CFD Investigation of Iced-Wing Performance Degradation Using DDES with the Spalart-Allmaras Extension to Consider Roughness Effects

by

Gitsuzo DE BRITO SIQUEIRA TAGAWA

THESIS PRESENTED TO ÉCOLE DE TECHNOLOGIE SUPÉRIEURE
IN PARTIAL FULFILLMENT FOR THE DEGREE OF
DOCTOR OF PHILOSOPHY
Ph.D.

MONTREAL, FEBRUARY 01, 2021

ECOLE DE TECHNOLOGIE SUPÉRIEURE
UNIVERSITÉ DU QUÉBEC

BOARD OF EXAMINERS

THIS THESIS HAS BEEN EVALUATED

BY THE FOLLOWING BOARD OF EXAMINERS

Prof. François Morency, Thesis Supervisor
Mechanical Engineering Department at École de technologie supérieure

Prof. Héloïse Beaugendre, Thesis Co-supervisor
Institut de Mathématiques de Bordeaux at Université de Bordeaux

Prof. Wahid Maref, President of the Board of Examiners
Construction Engineering Department at École de technologie supérieure

Prof. Louis Dufresne, Member of the jury
Mechanical Engineering Department at École de technologie supérieure

Prof. Lakhdar Remaki, External member
Mathematics & Computer Science Department at Alfaisal University

THIS THESIS WAS PRENSENTED AND DEFENDED

IN THE PRESENCE OF A BOARD OF EXAMINERS AND THE PUBLIC

ON JANUARY 20, 2021

AT ÉCOLE DE TECHNOLOGIE SUPÉRIEURE

ACKNOWLEDGMENT

I would like to express my deepest gratitude to my thesis supervisors, Professor François Morency from École de technologie supérieure (ÉTS), and Professor Héloïse Beaugendre from Inria Bordeaux Sud-Ouest. Their profound knowledge in aerodynamics and computational fluid dynamics has deeply enriched my understandings. Along these years, their continuous engagement and supervision have pushed me not only to achieve better results but also to evolve and strengthen my academic skills.

My family deserves a very special mention. I am grateful for the support they have given me along these years. Monia, Kenji, Katsuo and Hachi (my dog) left everything they had behind and embraced my dream of coming abroad to pursue my PhD. Only we know the innumerable challenges each one of us had to overcome in this long journey.

I am thankful to my friends from my country, and the new friends I have made in Canada. People from so many different parts of the world with contrasting differences in culture, traditions, habits, and beliefs. People from whom I have learned, and people I have taught. People that, after some time, made me realize how the preconceived ideas we have about other nations, in good and bad ways, might be misleading.

Finally, I am thankful to God who has always been wisely guiding me through all the moments of my life.

Investigation CFD sur la dégradation des performances des ailes glacées à l'aide de DDES avec l'extension Spalart-Allmaras implémentée pour prendre en compte les effets de rugosité

Gitsuzo DE BRITO SIQUEIRA TAGAWA

RÉSUMÉ

L'accrétion de glace peut réduire l'efficacité des surfaces portantes des aéronefs, ce qui augmente le coût du vol et le risque d'accidents. Des études expérimentales ont prouvé que le givrage, qui s'accompagne d'une augmentation de la rugosité, pouvait entraîner une réduction de 25% de la portance maximale et une augmentation de 90% de la traînée d'une aile d'allongement 6. Afin de mieux représenter les surfaces rugueuses et d'améliorer la fidélité des simulations CFD, différentes implémentations de rugosité ont été proposées, en particulier pour le modèle de turbulence Spalart-Allmaras (SA) bien établi et validé. De plus, la formation de glace en forme de corne entraîne une séparation massive des flux, générant des tourbillons énergiques dont la physique dans la couche externe ne peut pas être modélisée avec précision par l'approche RANS. Par conséquent, afin d'étudier les effets de la rugosité pour des écoulements séparés, nous proposons d'estimer numériquement la dégradation des performances aérodynamiques d'une aile tridimensionnelle givrée après l'angle de décrochage à l'aide d'un modèle hybride (RANS / LES) appelé DDES incluant le modèle RANS avec rugosité implémentée. Pour accélérer le déclenchement de l'instabilité de Kelvin-Helmholtz, l'échelle de longueur de sous-grille (SGS) adaptée à la couche de cisaillement (SLA) est utilisée en combinaison avec le schéma à faible dissipation HR-SLAU2. Dans un premier temps, la mise en œuvre de l'extension à la rugosité du modèle SA est vérifiée et validée à l'aide de cas d'étude de surface lisses et rugueuses. Ensuite, des cas d'étude à surface lisse avec détachement d'écoulement massif sont évalués. La nouvelle méthode est ensuite utilisée pour les estimations DDES des écoulements massivement séparés sur des cas d'étude à surface rugueuse. Dans le premier cas d'étude, l'écoulement sur une marche orientée aval (abrégé en BFS pour backwards facing step) est évalué. Les résultats montrent que la résistance causée par la rugosité produit trois effets principaux. Premièrement, il réduit la région de flux inverse maximal après la marche. Deuxièmement, la région d'écoulement inverse est formée 42% plus loin en aval. Troisièmement, le rattachement du flux se produit 12% plus loin en aval par rapport aux résultats générés avec le même modèle sur une surface lisse. Dans le deuxième cas d'étude, l'écoulement sur un modèle de profil 5-6 aérodynamique givré rugueux à un angle d'attaque de 8 degrés est étudié. Bien que la DDES ait présenté des estimations améliorées par rapport au modèle RANS, aucun effet de rugosité significatif n'a été observé sur l'écoulement autour d'un profil 5-6 avec une accumulation de glace de type corne. La différence dans les résultats du profil aérodynamique givré, par rapport à la configuration BFS, a été causée par deux raisons. Premièrement, la faible longueur de la distribution de rugosité (uniquement sur la glace), et deuxièmement, la plus grande perturbation créée par la corne de glace sur le bord d'attaque du profil aérodynamique, qui "occultait" les effets de rugosité.

Mots-clés : Simulation de tourbillons détachée retardée, DDES, rugosité, turbulence, adaptation de couche de cisaillement, profil aérodynamique glacé, dégradation des performances

CFD investigation of iced-wing performance degradation using DDES with the Spalart-Allmaras extension implemented to consider roughness effects

Gitsuzo DE BRITO SIQUEIRA TAGAWA

ABSTRACT

Ice accretion can reduce the efficiency of aircraft lifting surfaces, which increases the cost of flight and risk of accidents. Experiments proved that even the onset of icing (increased roughness) could cause a reduction of 25% in the maximum lift, and an increase of 90% in drag of an aspect ratio 6 wing. In order to better represent rough surfaces and improve the fidelity of CFD simulations, different roughness implementations have been proposed, especially for the well-established and validated Spalart-Allmaras (SA) turbulence model. In addition, horn-like ice formation results in massive flow separation, from which, the physics of the energetic eddies in the outer layer cannot be accurately modeled by RANS. Therefore, in order to investigate roughness effects for separated flows, we propose to numerically estimate the aerodynamic performance degradation of a three-dimensional post-stall-angle rough iced wing using a hybrid model (RANS/LES) called DDES including RANS with roughness implemented. To accelerate the unlocking of the Kelvin-Helmholtz instability, the Shear-Layer Adapted (SLA) Sub-Grid length Scale (SGS) is used in combination with the low-dissipation scheme HR-SLAU2. In the first step, the implementation of the SA roughness extension is verified and validated using smooth and rough-surface study-cases. Then, smooth-surface study cases with massive flow detachment are evaluated. The new method is then used for DDES estimations of massive-separated flows over rough-surface study cases are presented. In the first study case, the flow over a rough backward facing step is evaluated. Results show that, the resistance caused by roughness produces three main effects. First, it reduces the region of maximum reverse flow after the step. Second, the reverse flow region is formed 42% farther downstream. Third, the reattachment of the flow occurs 12% farther downstream as compared to results generated with the same model over a smooth surface. In the second study case, the flow over a rough iced model 5-6 airfoil at an angle of attack of 8 degrees is studied. Although the DDES presented improved estimations as compared to RANS, no significant roughness effects were noticed on the flow over a model 5-6 airfoils with a horn-type ice accretion. The difference seen between the iced airfoil and the BFS results, was caused by two reasons. First, the small length of the roughness distribution, which is only along the ice surface. Second, roughness effects were weaker than the great adverse pressure gradient created just after the tip of the horn ice, which "overshadowed" any roughness effects.

Keywords: Delayed Detached Eddy Simulation, DDES, roughness, turbulence, Shear-Layer Adapted, iced airfoil, performance degradation

TABLE OF CONTENTS

XII

LIST OF TABLES

LIST OF FIGURES AND ILLUSTRATIONS

Page

XVIII

LIST OF ABREVIATIONS AND ACRONYMS

AoA	Angle of Attack
AR	Aspect Ratio
AUSM	Advection Upstream Splitting Method
BFS	Backward Facing Step
CFD	Computational Fluid Dynamics
CFL	Courant–Friedrichs–Lewy
CPU	Central Processing Unit
CTU	Convective Time Unit
DDES	Delayed Detached Eddy Simulation
DES	Detached Eddy Simulation
DNS	Direct Numerical Simulation
FR	Focus Region
GARTEUR	Group for Aeronautical Research and Technology in Europe

HR-SLAU2	High-Resolution Simple Low Dissipation Advection Upstream
IDDES	Improved DDES
LES	Large Eddy Simulation
MDCD	Minimized Dissipation and Controllable Dissipation
MSD	Modeled Stress Depletion
NASA	The National Aeronautics and Space Administration
NSE	Navier Stokes Equations
NTSB	National Transportation Safety Board
PBC	Periodic Boundary Conditions
PDE	Partial Differential Equation
RANS	Reynolds-Averaged Navier-Stokes
SA	Spalart-Allmaras
SBC	Symmetric Boundary Conditions
SGS	Sub-Grid length Scale

SLA	Shear-Layer Adapted
SLAU	Simple Low Dissipation Advection Upstream
SST	Shear Stress Transport
URANS	Unsteady Reynolds Averaged Navier Stokes
VTM	Vortex Tilting Measure
WMB	Wind Multi Block
ZDES	Zonal DES

LIST OF SYMBOLS AND UNITS OF MEASUREMENTS
(INTERNATIONAL SYSTEM)

Roman Letters:

A_p *Projected area in the direction of the freestream velocity vector (m^2)*

A_s *Windward surface area of the element seen by the flow (m^2)*

c *Airfoil chord (m)*

C_d *Drag coefficient*

C_l *Lift coefficient*

$C_{l(\max)}$ *Maximum lift coefficient*

C_p *Pressure coefficient*

C_P *Specific heat of air at constant pressure*

C_f *Skin friction coefficient*

d *Distance to nearest wall (m)*

$\bar{d}$ *Modified length scale (DES) (m)*

$\tilde{d}$ *Modified length scale (DDES) (m)*

d_{new} *New distance from the nearest wall defined on the rough SA (m)*

E Total energy per unit mass (J kg^{-1})

$\vec{F}^c$ Convective fluxes

$\vec{F}^v$ Viscous fluxes

h Step height (m)

H Fluid enthalpy (J kg^{-1})

k Roughness height (m)

k_s Equivalent sand-grain roughness height (m)

$\tilde{K}$ Favre-averaged turbulent kinetic energy (J kg^{-1})

L Characteristic linear dimension (m)

Ma Mach number

P Static pressure (Pa)

$\Pr_d$ Dynamic Prandtl number

$\Pr_t$ Turbulent Prandtl number

r_0 Mean distance between roughness elements (m)

R Gas constant for air (287.06 J kg^{-1} K^{-1})

Re   *Reynolds number*

Re_k *Roughness Reynolds number*

s   *Distance on the upper camber (m)*

S   *Rate of strain (s^{-1})*

Su   *Sutherland temperature (273K)*

$\tilde{S}_{ij}$ *Favre-averaged strain rate (s^{-1})*

T   *Temperature (K)*

T_{ref} *Reference temperature (K)*

$\vec{U}$ *Vector of conservative variables*

y+   *Nondimensional wall distance*

Greek Letters:

γ *Ratio of specific heats* $\gamma = C_P / C_V$

δ_{ij} *Kroneckerd delta function*

Δ Local maximum grid spacing based on the three directions ($\Delta = \max(\Delta_x, \Delta_y, \Delta_z)$)

Δt *Time step (s)*

Δt^* *Non-dimensional time step*

κ *von Kármán constant (0.41)*

λ *Roughness shape parameter*

μ_{dyn} *Dynamic or laminar viscosity (N s m^{-2})*

μ_{ref} *Reference dynamic viscosity (N s m^{-2})*

μ_{tot} *Total viscosity (N s m^{-2})*

μ_{tot}^* *Effective total thermal conductivity (W m^{-1} K^{-1})*

μ_{tur} *Turbulent dynamic viscosity or eddy viscosity (N s m^{-2})*

ν *Laminar kinematic viscosity ($m^2 s^{-1}$)*

ν_{tur} *Turbulent kinematic viscosity ($m^2 s^{-1}$)*

$\hat{\nu}$ *Eddy-viscosity variable*

ρ *Air density (kg m^{-3})*

σ *Adaptative dissipation function*

τ_{ij} *Viscous stress (Nm^{-2})*

τ_w *Wall shear stress (Nm^{-2})*

υ *Velocity (m/s)*

υ_τ *Friction velocity (m/s)*

υ_∞ *Freestream velocity (m/s)*

$\vec{\omega}$ *Vorticity vector (Hz)*

Ω *Vorticity tensor (Hz)*

INTRODUCTION

This chapter covers an introduction to aircraft icing, and the risks of accidents due to this phenomenon. Additionally, we briefly present the common methods used to evaluate the effects caused by icing, some simplifications commonly seen in the literature of CFD simulations of iced airfoils, and how we propose to investigate roughness effects for separated flows caused by icing. Finally, the research objectives and thesis outline are presented.

In-flight icing

Airplanes have changed human history shortening distances and facilitating interaction among people all over the world. Several challenges have been surpassed along the years; however, others are still to be completely overcome such as the problem of icing. This kind of problem generally occurs when airplanes fly through clouds that contain super-cooled liquid droplets, which impinge on the airplane surfaces, and freeze (Zhang et al., 2015), initially forming thin layers of ice and, then, as time progresses, becoming thicker with different shapes. When on wings and tails, icing results in increased drag and reduced lift due to the change in shape and surface roughness, which can cause the airplane to stall and/or behave uncontrollably resulting in fatal accidents.

According to Ratvasky et al. (2010), there has been a great effort to reduce risks imposed by icing for over 80 years, and valuable achievements have been made such as the development of ice protection systems, strict certification procedures, and improved pilot training, which have cooperated to reduce the number of accidents. However, icing is still the cause of several accidents as can be seen by statistics of accidents and incidents that occurred only within the United States of America. (Green, 2006) mapped almost 1000 accidents and incidents due to icing from 1978 to 2002. Between 2006 and 2010, another 228 accidents and 30 inflight incidents were catalogued by (Appiah-Kubi, 2011). Additionally, (Eick, 2015) identified another 52 accidents on the NTSB (National Transportation Safety Board) database from 2010

to 2014. Therefore, it is of paramount importance to study and understand the effects caused by icing on the surface of airplanes so that this problem can be efficiently tackled.

Currently, there are three main approaches to evaluate the effects of ice accretion on the surface of airplanes, flight test, wind-tunnel testing, and numerical simulations. According to Cao et al. (2015), flight test yields the most reliable iced-aircraft aerodynamic data, though at a relatively high cost. Wind-tunnel experiments offer lower cost, but due to the difficulties to establish an icing wind-tunnel, simulated ice shapes are often used, which reduces the reliability of results. In the last decades, (Computational Fluid Dynamics, CFD) gained popularity, and it has been increasingly applied in multi-disciplinary design and analysis of aerospace products (Spalart & Venkatakrishnan, 2016). In their work, (Spalart & Venkatakrishnan, 2016) clearly state the extensive use of CFD on the design of the new Boeing 787. The areas presented by the authors are summarized in Table 1, in which the areas in green have present strong CFD penetration; the blue areas have some penetration; and the orange areas present future opportunities.

Table 1 Impact of CFD at Boeing. Green areas have strong CFD penetration; blue areas have some penetration; orange areas present future opportunities

Strong CFD penetration	Some CFD penetration	Future opportunities
Wing tip design	Cabin noise	Wing controls
Vertical tail and aft body design	Interior air quality	Design for FOD prevention
Horizontal tail design	Connexion Antenna	Inlet certification
Wing-body fairing design	High-lift wing design	Design for stability & control
Engine/airframe integration	Icing	
Planform design	Control failure analysis	
Exhaust system design	Buffet boundary	
Engine bay thermal analysis	APU inlet and ducting	
Air data system location	Avionics cooling	
Cab design	Design for loads	
Wind tunnel corrections	Vortex generator placement	
High-speed wing design	Wake vortex alleviation	
ECS inlet design	APU and propulsion fire suppression	
Inlet design	Aeroelastics	
	Flutter	
	Community noise	
	Thrust reverser design	
	Reynolds number corrections for loads and S&C	
	Nacelle design	

Along the years, the set of Partial Differential Equations (PDE) that describe the motion of viscous fluids, Navier-Stokes Equations (NSE), have been numerically solved using the time-averaged method, introduced by Osborne Reynolds in 1895, called Reynolds-Averaged Navier-Stokes (RANS) model, which is combined with turbulence models that solve the Reynolds stress such as the Spalart-Allmaras or Menter's SST $k-\omega$, among others (Blazek, 2015). This method has also been used in industry and academia to estimate the performance degradation of iced airfoils (GARTEUR, 2003). However, the estimation of aerodynamic parameters of flows with massive separation such as iced airfoils becomes challenging to RANS (Larsson et al, 2016). Therefore, an intermediate approach, called Large Eddie Simulation (LES), has been used to achieve more accurate results than RANS, while with a reduced computational cost as compared to the Direct Numerical Simulation (DNS) of the flow. In LES, a filtering process is used in the NSE to model the smallest length scales, and directly compute only the large eddies (Zhiyin, 2015).

When considering simulations of aircraft with flaps, landing gear, slat brackets, vortex generators, etc., LES models are much more powerful to capture the physics of the detached flows. On the other hand, RANS models present higher performance in the large areas of thin boundary layer (Spalart et al., 1997). Moreover, according to Larsson et al. (2016), even though LES approaches have displaced RANS in academia, they are seldom used in the actual engineering design process due to computational cost. Therefore, in order to profit from both LES and RANS advantages, hybrid models (RANS/LES) have been proposed, and the first model (Detached Eddy Simulation, DES), created by Spalart et al. (1997), successfully improved estimations when applied to different study cases.

On the other hand, the current hybrid models used for the estimation of the performance degradation of iced airfoils do not consider the ice rugosity. Additionally, Stebbins (2018) points out two simplifications commonly seen in the literature of CFD simulations of iced airfoils. First, icing is evaluated as a two-dimensional phenomenon, in which the three-dimensional ice effects are neglected. Second, even when the effects of ice are considered in a three-dimensional domain, simple extrusions of two-dimensional representational cuts of ice

shapes are performed, which, according to the author, smooths out a large portion of the roughness of the geometry.

Thesis Outline

This document is organized as follows: **Chapter 1** presents a literature review, in which we describe the types of ice catalogued and the ones used in this work, how these types of ice are characterized, and the aerodynamic effects produced by them. Additionally, we provide an overall picture of numerical simulations of aircraft icing, the commonly used RANS for the evaluation of icing effects, the proposed hybrid models, and their evolution. Finally, we look into the surface roughness study as well as the proposed approaches to treat it numerically. **Chapter 2** defines the problem under study, then, the models used herein are presented. First, the widely used RANS model is presented followed by the turbulence model applied in our simulations, Spalart-Allmaras (SA). Next, the extension of SA model that considers roughness is presented. Then, the Large Eddy Simulation (LES) is introduced. Following, the hybrid models Detached Eddy Simulation (DES) and Delayed Detached Eddy Simulation (DDES) are described along with a method to improve the transition between RANS and LES called Shear-layer Adapted model. Then, the computational method utilized is depicted along with the boundary conditions. Finally, we present an overview on the statistics process performed in this thesis, as well as how discrepancies and errors were calculated. **Chapter 3** presents the verification and validation process of the proposed method. First, the RANS model with the roughness implementation is evaluated using three study cases, a flat plate, a backward facing step, and a NACA 0012 airfoil. Each one of them is studied in two distinct configurations, with and without roughness. Moreover, two additional investigations were performed. One to evaluate the Reynolds number sensitivity, and the other to evaluate the influence of equivalent sand-grain roughness heights on the aircraft performance degradation. After that, we began the verification and validation of the DDES model with roughness implemented. First, a study to evaluate the appropriate width of a channel with a backward facing step for our simulations was performed. Then, once the width was chosen, a study of flows over two study cases with massive flow separation was carried out. Here, a backward facing step, and a NACA 0012

airfoil in deep stall were chosen as study cases. Finally, in **Chapter 4**, we study massive-separated flows over rough surfaces using the DDES model with roughness implemented. The first study case is a rough backward facing step, and the second is a rough-iced model 5-6 airfoil at an angle of attack of 8 degrees.

CHAPTER 1

LITERATURE REVIEW AND FURTHER INFORMATION

1.1 Performance Degradation due to icing

Although accreted ice has not a specific shape, Bragg et al. (2005) catalogued four representative types of ice shapes based on their contour characteristics: roughness, horn ice, streamwise ice, and spanwise-ridge ice. Roughness is formed during the initial stages of ice accretion, whereas prolonged stages may lead to the second type of ice, which is characterized by a horn-like shape on the leading edge of the airfoil. In the streamwise type, ice grows conforming the airfoil; and finally, the last type of ice is commonly formed downstream of heated leading edges as water freezes again when reaching a colder surface.

Along this work, the first two representative types of ice shapes, roughness and horn ice, as well as the superimposition of the first over the latter, which results in a rough horn ice, will be used. Bragg et al. (2005) gathered and highlighted key flow field features of these types of iced airfoils based on their study and several references. They characterized the onset of ice formation (roughness) by its height, density (how clustered they are), and surface location. In general, as height and/or density increases, the maximum lift coefficient is reduced, which was also shown by (Brumby, 1979; Jackson, 1999). However, when the density is increased above 30%, roughness effects diminish due to a reduction in the interaction between elements as a downstream element is in the wake of the upstream element (Bragg et al., 2005). As for the location, although Brumby (1979) showed that the sensitiveness increases as roughness is placed closer to the leading-edge of the airfoil, (Bragg & Gregorek, 1989) concluded that this behaviour is roughness size and airfoil dependent.

Even in its very earlier stages (increased roughness on the surfaces), icing frequently degrades aerodynamic performance by reducing lift and increasing drag, which results in lower stall angles, and higher risks of accidents. In experiments performed by Beierle (1999), it was shown that standard leading-edge roughness could increase the minimum drag coefficient of

63% for a NACA 0015 airfoil when compared to the clean one. The authors also showed that as the roughness region increases in length on the same airfoil, greater reduction of lift-to-drag is produced, especially for angles superior to 3 degrees up to the stall angle. Similarly, Gulick (1938) obtained from his experiments a reduction of 25% in the maximum lift, and an increase of 90% in drag due to roughness added to an aspect ratio 6 wing to simulate icing.

As for the horn ice, Bragg et al. (2005) characterized this type of icing by its height, the angle it makes with respect to the chord line, and its location on the surface. According to the authors, the separation bubble formed downstream of the horn is the dominant flow feature that determines the aerodynamics of this type of iced airfoil. They verified that the detailed shape of the horn played no significant role in the aerodynamics based on the studies of (Kim & Bragg, 1999; Papadakis et al., 1999; Papadakis, Alansatan, & Wong, 2000; Papadakis, Alansatan, & Yeong, 2000; Papadakis & Gile Laflin, 2001; Papadakis, Gile Laflin, et al., 2001; Papadakis, Yeong, et al., 2001). Kim and Bragg (1999) evaluated the effects of a horn height placed perpendicular to the surface of an NFL 0414 airfoil at a nondimensional distance on the upper camber (s/c) of 3.4%. When a 0.022 nondimensional height (k/c) horn ice was added to the airfoil, the maximum lift coefficient ($C_{l\text{(max)}}$) reduced 47% as compared to the clean airfoil. For a $k/c = 0.044$ height, the reduction was 58.5%, and for a $k/c = 0.067$ height, the reduction was 67%. The same authors also noted an incremental reduction of $C_{l\text{(max)}}$ when the horn was moved towards the trailing edge (up to $s/c = 4\%$). Steeper curves were found for higher horn ices.

1.2 Numerical Simulation of aircraft icing

A very rich and vast literature review on aerodynamics in icing since its very beginning (late 1920s) up to the 2000s can be found in Bragg et al. (2005). The authors touched interesting historical points such as the fact that up to 1978 icing research was almost exclusively experimental, and the beginning of the use of numerical methods to study icing began in 1979, mainly influenced by the NASA aircraft-icing program. They also pointed out that most icing research was focused on large leading-edge ice shapes, which changed after the ATR-72

accident in late 1994. From that moment on, several joint research programs were conducted to improve and validate numerical methods results.

The accumulated experimental data produced in the first years of icing research inspired some authors to create empirical correlations to evaluate icing effects on the aerodynamic of aircrafts. In 1958, Gray (1958) developed a correlation to evaluate the change in drag due to icing formation using the NACA 65A004, and in 1964, he extended his correlation to various airfoils (Gray, 1964). Another rich study was done by Brumby (1979), in which he presented empirical curves of maximum lift loss caused by roughness. His results clearly show the effects caused by position and height of roughness on the maximum lift coefficient. In 1982, Bragg (1982) developed a methodology to predict the growth of rime ice as well as its aerodynamic effects. According to the author, it was the pioneering approach to include time effects on the icing analysis. In 1987, Cebeci (1987) used a complex technique to evaluated the effects of icing using an Interactive Boundary-Layer technique (IBL).

With the evolution of computers, CFD became very attractive due to its reduced cost and satisfactory results (Cao et al., 2015). Another huge advantage of this method is that only numerical methods are able to explore, safely, all icing conditions required for certification (Beaugendre et al., 2003). Thus, researchers and engineers began to solve numerically the set of Navier-Stokes Equations (NSE). However, as almost all macroscopic flows in engineering practice are turbulent at higher Reynolds numbers (Kundu et al., 2012), an enormous range of length scales must be resolved. In order to achieve sufficient spatial resolutions in turbulent flow simulations, the number of grid points required is $\mathrm{Re}^{9/4}$, and the CPU-time is Re^3 (Blazek, 2015). Therefore, even nowadays, the direct numerical simulation of the NSE is only possible for simple turbulent flow cases at low Reynolds numbers (Blazek, 2015).

In this way, for engineering purpose, the approximation of the solution of the NSE has usually been done by making use of Reynolds-Averaged Navier-Stokes (RANS) equations. In this approach, the flow variables are decomposed into mean and fluctuating parts, followed by time or ensemble averaging (Blazek, 2015). However, as the development of RANS equations

yields six extra unknowns named Reynolds stresses, additional turbulent models are required to solve these variables. The most known models are mixing length, Reynolds stress, algebraic stress, $k-\varepsilon$, $k-\omega$, and Spalart-Allmaras (SA). Currently, the leading models used for aerospace applications are the Spalart-Allmaras (Versteeg & Malalasekera, 2007) and the Menter's SST $k-\omega$ turbulence models (Bates et al., 2005).

In 2003, a large study aimed to assess existing CFD codes was made by the Group for Aeronautical Research and Technology in Europe (GARTEUR), from which a report titled "Prediction of Performance Degradation Due to Icing for 2D Configurations" was published (GARTEUR, 2003). Several CFD codes, from Aerospatiale (now Airbus France), CIRA, DERA (now QinetiQ), DLR, Eurocopter France, INTA, NLR, ONERA, SAAB and DLR were used to estimate the performance degradation due to ice accretion in 2D airfoils, and results were assessed with experiments from the open literature. The leading models used were based on RANS equations.

Although RANS equations have been widely used in industry and academia for several years to evaluate attached boundary layer flows, it cannot robustly capture the physics of the energetic eddies in the outer layer (Larsson et al., 2016) during near-stall conditions, especially in iced-airfoils due to ice-shape vortex shedding (Pan and Loth, 2005). Therefore, in the last decade, hybrid RANS/LES models have gained popularity in aeronautical industry due to the high performance and low computational cost of RANS in the areas of thin boundary layers, and the high accuracy of LES for detached flows.

The first proposed hybrid model, called Detached Eddy Simulation (DES), was introduced by Spalart et al. (1997), and it was defined as "a three-dimensional unsteady numerical solution using a single turbulence model, which functions as a subgrid-scale model in regions where the grid density is fine enough for a large-eddy simulation, and as a Reynolds-averaged model in regions where it is not" (Travin et al., 2000). The model was rapidly well accepted among researchers and engineers. Spalart (2009) presented a vast reference of works in which DES was applied using cavities, ground vehicles, a simplified landing-gear truck, active flow control

by suction/blowing, space launchers, vibrating cylinders with strakes, cavitation in jets, buildings, air inlets, aircraft in a spin, high-lift devices, jet fighter tail buffet, and wing-wall junctions.

The DES formulation relied on the usual RANS-grids with highly stretched cells near the wall, in which the grid spacing along the flow direction is much larger than the boundary layer thickness. However, if the grid is gradually refined, the LES mode is activated inside the attached boundary layer. This problem was named Modeled Stress Depletion (MSD) due to the reduction of the RANS Reynolds Stresses (Mockett, 2009), and it was first encountered in studies of (Caruelle, 2000; Deck, 2002; Menter & Kuntz, 2004). To prevent this situation, Spalart et al. (2005) proposed a new formulation called Delayed Detached Eddy Simulation (DDES), in which a new length scale definition is also solution depended, rather than grid dependent only.

Thus, several studies began to emerge in the literature comparing DES and DDES estimations. (Squires et al., 2008) used both models to estimate aerodynamic parameter of the flow around a circular cylinder at high Reynolds number. No significant differences were obtained with DES and DDES. (Lorenzo et al., 2011) assessed the flow over an iced model 5-6 airfoil, in which mesh refinement is usually required near the wall due to the steep variation in geometry. The authors showed that, for 2D simulations, a good mesh refinement makes DES and DDES estimations equivalent. On the other hand, 3D DDES estimations of C_l, C_d and C_p were slightly improved over DES. (Im & Zha, 2014a) estimated C_l and C_d over a NACA0012 airfoil in deep stall using URANS, DES and DDES with high order schemes. Although DES and DDES results were improved over URANS, no significant difference was noticed between them.

In recent years, aircraft icing research efforts have focused, not only on DES and DDES, but also on different versions such as the Improved DDES (IDDES) and the Zonal DES (ZDES). According to Butler et al. (2016), the IDDES model, proposed by Shur et al. (2008), is suitable for the analysis of flow topologies with medium degrees of flow separation. The authors used

IDDES to evaluate the flow over an iced NACA0012 airfoil, which presented significant improvement over the DDES model. Moreover, the simple switch from DDES to IDDES proved as effective as a 50% improvement in grid resolution on the results accuracy. In the ZDES approach, RANS and LES regions are explicitly defined by the user, which makes it difficult to be used as a general tool. Deck (2005) first proposed a generalized zonal approach, which was later improved (Deck, 2012). This approach is combined with the features of the DDES model, and was later used by Zhang et al. (2015) to study the effect of span width domain size and grid density on detached flow behavior around two airfoils, the iced GLC-305 and the NACA23012. The authors concluded that a spanwise length larger than 0.3c is necessary to properly represent the physics of the turbulence in the wake flow. They also found out that insufficient grid density results in augmented eddy viscosity, which retards the development of Kelvin-Helmholtz instability, and consequently the transition from RANS to LES.

According to Mockett et al. (2018), the transition from RANS to LES (the so-called 'grey area') in DDES is commonly trigged by an instability. In flows dominated by separating shear layers, DDES has a fairly slow transition due to relatively high LES eddy-viscosity. In an effort to speed up the Kelvin-Helmholtz instability of the free shear layer formed over iced airfoils, Xiao et al. (2017a) used the DDES combined with the low dissipation schemes SLAU/MDCD, which improved estimations of the lift coefficient on an iced GLC-305 airfoil compared to the ZDES models. Another approach to unlock the Kelvin-Helmholtz instability, and accelerate transition to 2D, and, then, 3D flow structures in shear layers was proposed by Shur et al. (2015). Their model is called Shear-Layer Adapted (SLA) Sub-Grid length Scale (SGS), and it proposes a new length scale definition that tries to correct the anisotropic grid cell effects on the RANS/LES transition taking into account the direction of the vorticity vector. The SLA-SGS is also referred to Enhanced DDES in the literature (Jefferson-Loveday, 2020; Younes et al., 2020).

Molina et al. (2017) confirmed the improved performance of this approach using a backward-facing step, tandem cylinders, and a wing at transonic buffet conditions study cases. Similarly,

Guseva et al. (2017) made a comparative study of the original versions of DDES and IDDES, and their equivalent versions with SLA-SGS implemented. The authors studied different flows: a flow with non-fixed pressure-induced separation and reattachment (wall-mounted hump), a massively separated flow (NACA 0021 airfoil beyond stall), and a supersonic separated flow (wake behind a cylindrical body). Their results confirmed the accelerated RANS/LES transition produced by the SLA-SGS.

More recently, the GLC-305 airfoil with a leading-edge horn-shape glaze ice was used in a study carried out by Molina et al. (2020), in which the standard Sub-Grid length Scale (SGS) is compared to the Shear-Layer Adapted Sub-Grid length Scale (SLA-SGS) model. The authors also combined the SLA-SGS model with a low-dissipation scheme, HR-SLAU2. The rapid transition from RANS to LES was shown, and consequently, a significant reduction of the 'grey area', when the SLA-SGS model was used. As, according to Molina et al. (2020), this is "the latest Shear-Layer Adapted Sub-Grid length Scale" to date, and improved estimations was shown in the literature, it will be the model selected to the roughness implementation as well as the numerical simulations within this thesis.

1.3   Modification of RANS model to account for roughness

Roughness is one of the main characteristics of ice accretion, and although only the onset of ice formation is commonly treated as a rough surface, the other types of ice catalogued by Bragg et al. (2005) are also rough. According to Stebbins et al. (2019), in three-dimensional simulations, it is a common practice to extrude two-dimensional representational cuts of ice shapes, which smooths out a large portion of the roughness of the geometry. The authors highlight that this loss of fidelity is an open research question, and it can depend on several parameters. Nevertheless, most studies in the literature do not take roughness effects into account when performing numerical simulations with hybrid models on iced airfoils such as the horn-type shape. This is not surprising due to the challenges involved in the roughness study. According to Flack and Schultz (2010), "the most important unresolved issue regarding

surface roughness in fluid engineering practice is how frictional drag (for external flows) or pressure drop (for internal flows) relates to the particular roughness topography".

Different experimental studies on roughness were performed in the past and, some of them, became reference such as the well-known works of (Moody, 1944; Nikuradse, 1933; Schlichting, 1937). Nikuradse (1933) made an extensive study on rough pipes, which resulted in a vast amount of data and important observations such as the division of the three different regions of the flow based on the roughness Reynolds number (Re_k), "hydraulically smooth", "transition", and "completely rough". Based on Nikuradse's data, Schlichting (1937) proposed the equivalent sand-grain roughness (k_s), which is an idealized roughness deduced from the real roughness height using empirical correlations. He showed that k_s is affected by the height, shape, and density of roughness. Also based on the data built by Nikuradse, Moody (1944) created a diagram that relates the friction factor, Reynolds number, and surface roughness. Due to its simplicity, the Moody diagram is still widely used to calculate the loss of energy caused by viscous friction in pipes (LaViolette, 2017).

For numerical simulations, there are three commonly used approaches to predict flow over rough surfaces, "highest fidelity", "discrete element approach", and "equivalent sand grain" (deVelder, 2020). As reported in (Aupoix, 2015b), the first approach consists of computing the flow around the roughness elements, which is presently done only at a research level due to its high computational cost. In the second approach, roughness effects are averaged at a higher level from the reference surface, which requires the modification of the mean flow equations to account for blockage effects caused by the roughness elements. However, Aupoix emphasizes that this modification precludes the use of this technique in general RANS solvers. The last approach is the most popular and, according to Aupoix, it is the only affordable one for industrial applications. In this technique, the equivalent sand-grain roughness (k_s), proposed by Schlichting (1937), is used to represent the height of a sand grain from Nikuradse's experiments, and reproduce the drag increase in the fully rough regime. With the purpose of reducing the uncertainty in the determination of the equivalent sand-grain

roughness, Dirling (1973) proposed a correlation in which topological features are translated into the k_s. This correlation became very popular, and it is frequently cited in the literature (Liu, 2014).

Different roughness implementations based on the equivalent sand grain have been proposed, especially for the well-established and validated $k - \omega$ Shear-Stress Transport (SST) and Spalart-Allmaras (SA) turbulence models. The history of $k - \omega$ models that take roughness into account is somewhat extensive, and different formulations have been proposed. In 1988, Wilcox (1988) proposed a roughness correction for the $k - \omega$ model, which presented satisfactory results. However, Hellsten and Laine (1998) observed the shortcoming in Wilcox's technique of not working well with the $k - \omega$ SST model. Therefore, they proposed an extension for the $k - \omega$ SST model to account for roughness by adjusting the surface value of ω. Similarly, Knopp et al. (2009) improved not only model compatibility with the $k - \omega$ SST but also another shortcoming in Wilcox's model, the requirement of a much finer near-wall grid resolution for rough walls than smooth ones. The authors proposed a new model inspired by the strategy developed by ONERA and Boeing (Aupoix & Spalart, 2003) for the SA turbulence model. However, the results obtained with this model were highly grid-dependent (Lee, 2018), and the model strongly underestimated the velocity shift caused by roughness in the transition regime (Aupoix, 2015b). Therefore, Aupoix (2015b) proposed a new SST model that performs better in the three roughness regimes.

For the Spalart-Allmaras turbulence model, two different extensions were independently developed by ONERA and Boeing (Aupoix & Spalart, 2003). Both models are based on the commonly used equivalent sand grain approach (k_s), which is utilized to reproduce the drag increase in the turbulent model. Aupoix (2015a) noticed that k_s produced overestimated values of heat flux. Therefore, the author proposed a correction of the Prandtl number based on a large database obtained with the discrete element approach to improve estimations.

As seen in the literature review, although RANS has been used for decades in industry and academia to estimate the performance degradation of iced airfoils, it fails to robustly capture

the physics of massive flow separation. Thus, the proposed hybrid models (RANS/LES) such as DES and DDES, and their improved versions, have been increasingly used in the study of iced airfoils, which has been augmenting fidelity of estimations. On the other hand, it was also shown that, to the date and to the best of our knowledge, roughness has never been considered in the study of iced airfoils using DES or DDES. Therefore, we propose to numerically estimate the aerodynamic performance degradation of a three-dimensional post-stall-angle rough iced wing using a hybrid model (RANS/LES) called DDES including RANS with roughness implemented. The roughness model is implemented into an open-source code called Stanford University Unstructured, SU2, which is a collection of tools written in C++ and Python aimed at performing multi-physics simulations (Palacios et al., 2013).

1.4 Research Objectives

The main objective of this research is to numerically estimate the aerodynamic performance degradation of a three-dimensional post-stall-angle rough iced wing using a hybrid model (RANS/LES) called DDES including RANS with roughness implemented.

In order to achieve the main objective, the following sub-objectives are carried out:

1)   Propose a DDES model that includes RANS with roughness.

2)   Verify and validate the Spalart-Allmaras roughness implementation in SU2, which is performed separately. First, RANS with the roughness implementation is verified and validated using rough and smooth surfaces. Following, DDES is verified and validated using smooth surfaces with massive flow separation.

3)   Evaluate how roughness affects DDES estimations of aerodynamic parameters of massive-separated flows over rough surfaces. The evaluation is performed using two three-dimensional study cases, a rough backward facing step and a rough-iced model 5-6 airfoil.

1.5   Contributions

The purpose of numerical simulations is to represent and mimic the behaviour of real systems based on mathematical models. Along the years, mathematical models, approaches, and methods have been evolving in an effort to improve fidelity of numerical simulations. Towards the same objective, this research contributes by:

-       Proposing a method, which is a combination of models and schemes that simulates the behaviour of flows over three-dimensional rough iced wings. The main advantage of this approach is twofold. First, it robustly represents the physics of turbulent massive-detached flows. Second, it considers the effects produced by the surface (ice) roughness.

-       Verifying and validating the models with the roughness implementation to prove that they behave as expected. We performed RANS (smooth and rough surfaces) and DDES (smooth surfaces with massive flow separation) simulations. For RANS, we used the classical study case originally utilized for the validation of the rough SA model. In addition, another two study cases were used, a NACA 0012 airfoil, and an iced model 5-6 airfoil. Each study case is duplicated so that we can evaluate flows over smooth and rough surfaces. For DDES, two study cases with massive flow separation are used, a smooth-surface channel with a Backward Facing Step, and a smooth-surface NACA 0012 airfoil in deep stall. In addition, we perform two investigations with the roughness implementation in RANS, a study on the Reynolds number sensitivity, and the influence of equivalent sand-grain roughness heights on the aircraft performance degradation based on the deterioration of the $C_{l(\max)}$.

-       Proving that, although roughness causes significant effects on a backward facing step, no roughness effects are seen on a rough iced airfoil. Our results showed that the great adverse pressure gradient created after the tip of the horn ice prevailed against the roughness effects.

CHAPTER 2

MODEL AND METHODOLOGY

2.1 Problem definition

As mentioned before, cloud droplets can remain in their liquid form at temperatures well below water freezing point. When airplanes fly into clouds that contain these super-cooled water droplets, ice crystals are formed on the leading edge of the surfaces, as illustrated in Figure 2-1, which represents the scheme of the physical problem under study. The aircraft of weight, W, is flying at a velocity, V. The wings generate a lift force, L, equal to the weight. The engines thrust, T, must be equal or superior to the drag, D. As the aircraft enters clouds at below freezing point temperatures, ice begins to accrete on the leading edge of the wings, shown in blue.

The aerodynamic performance of various lifting components with small or large ice accretion should be known to enable proper aircraft design and certification as well as the development of efficient anti-icing and de-icing systems. According to Anderson (2001), although the aerodynamic forces generated on aircraft seem complex, they have two basic sources: pressure and shear stress distribution over the body. Based on them, one can obtain lift, drag and moments, which are important in the preliminary design and performance analysis of airplanes. The same author also affirms that almost all the lift, at cruising conditions, is produced by the wing. Thus, it is important to study the mentioned forces generated on airplane's wings. However, in aeronautical engineering, dimensionless force and moment coefficients are most used. Therefore, the aerodynamic effects produced on wings are commonly presented in the literature in terms of lift, drag and moment coefficients.
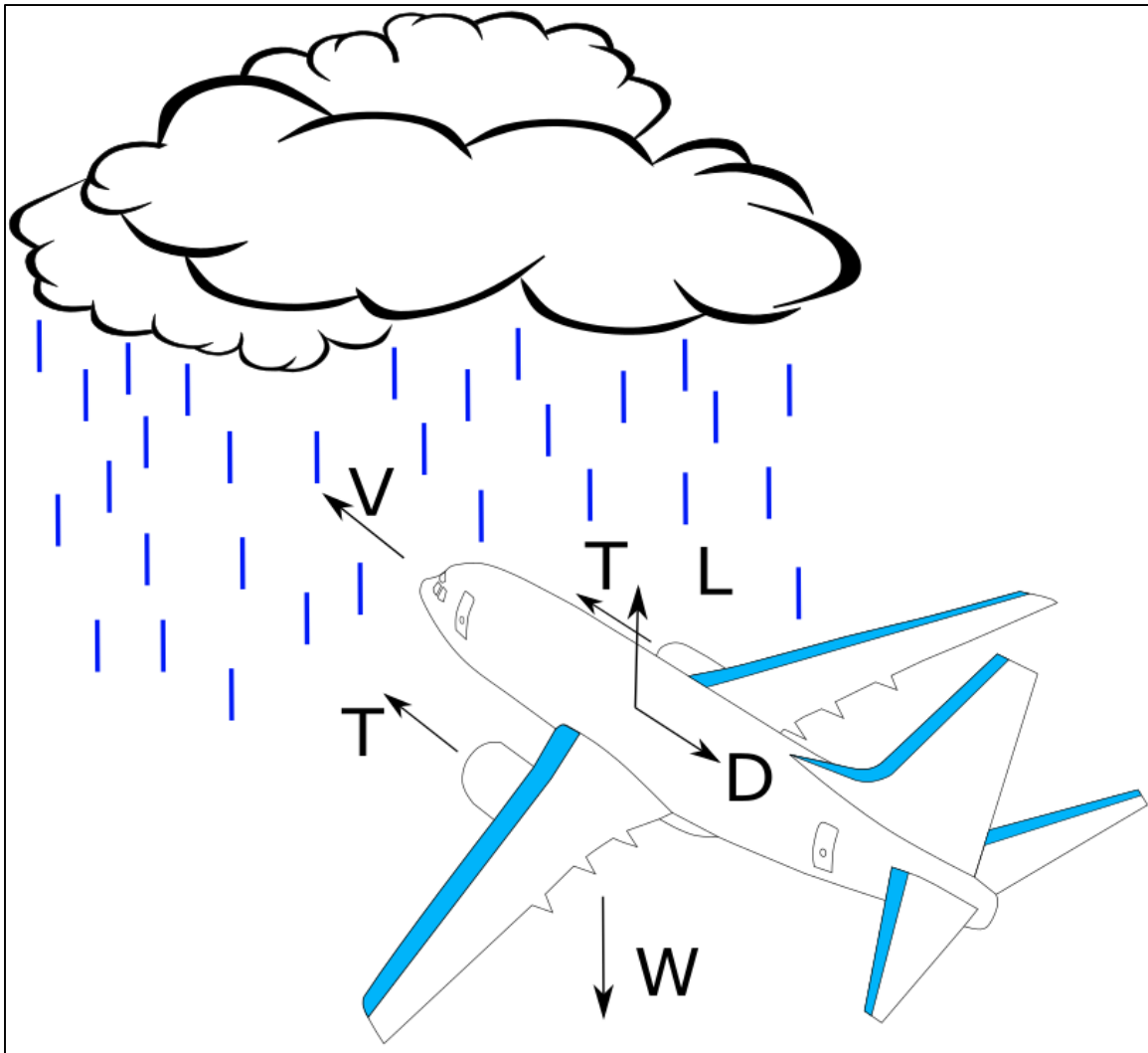
Figure 2-1 Scheme of the physical problem under study

In order to evaluate the performance degradation created by the accreted ice on the leading edge (shown in blue in Figure 2-1 and Figure 2-2), the wing is modeled as a straight infinite wing. Therefore, we assume that the wing performance degradation is equivalent to the one computed over a straight infinite wing with a uniform ice shape along the span. Nevertheless, the problem is still considered as 3D because we intend to model the large 3D turbulent structures. Figure 2-2 illustrates a perspective view of the problem under study.
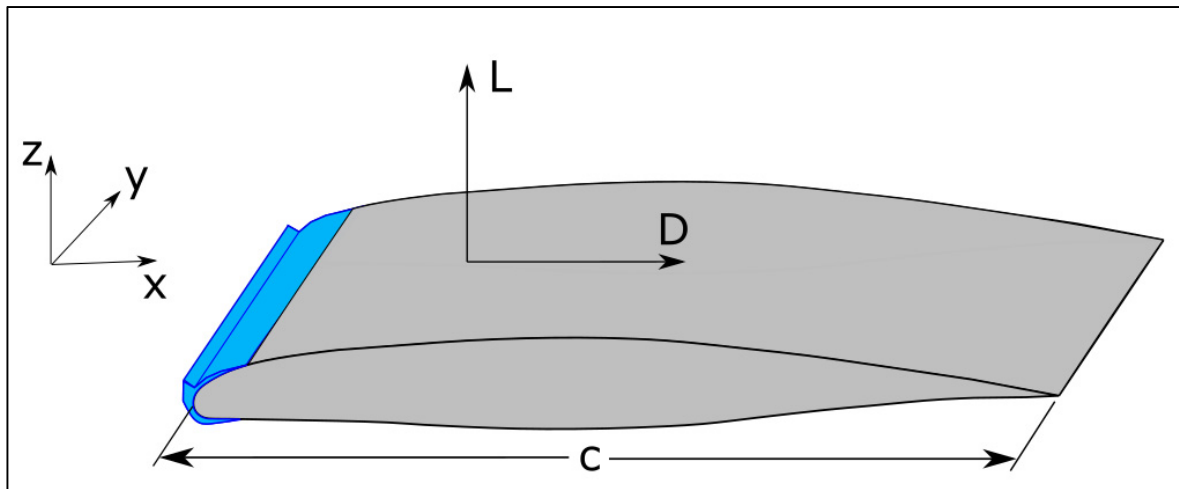
Figure 2-2 Perspective view of the model 5-6 airfoil

The airfoil of chord c has a horn iced shape on the leading edge that creates airflow separation at a lower Angle of Attack (AoA), as compared to the clean airfoil. The airflow separation is modeled as an unsteady compressible turbulent flow. Therefore, lift, drag and moment coefficients will fluctuate over time. From an aircraft aerodynamic point of view, the fluctuations are fast and can be neglected. The average coefficients are of interest however, especially when compared to the clean airfoil coefficients.

As already mentioned, in-flight ice accretion degrades aerodynamic performance reducing lift and increasing drag, which results in lower stall angles and higher risks of accidents. To evaluate the aerodynamic effects caused by in-flight icing, lift and drag coefficients are estimated using straight infinite wings with two types of ice, the onset of ice accretion represented by roughness, and a horn-shape type formation. For the first type of ice, only RANS is active in the model, whereas for the second type, RANS or LES might be active. The ice roughness is modeled based on the equivalent sand grain roughness approach, and it is estimated using the SA extension implemented into the DDES model. The horn-shape ice is chosen based on (GARTEUR, 2003), and it will be modeled as smooth and rough ice (the ice surface) so that the impact of roughness on the performance degradation can be evaluated. As large regions of flow detachment are expected in this case, both models will be active, RANS in attached regions, and LES in regions of massive detachment.

2.2 Mathematical model

2.2.1 Reynolds-Averaged Navier-Stokes (RANS)

According to Kundu et al. (2012), almost all macroscopic flows in engineering practice are turbulent. Although the NSE can be used to evaluate turbulence, the enormous range of length scales to be resolved is virtually impossible, and not necessary at high Reynolds numbers (Kundu et al., 2012). Therefore, Reynolds proposed to average the equations of motion by separating the quantities in mean and fluctuating parts. This process is known as Reynolds decomposition, and leads to the Reynolds-Averaged Navier-Stokes equations. According to Blazek (2015), for compressible flows, where the density is not constant, it is recommended to apply Reynolds averaging for density and pressure, whereas Favre averaging is used for the other variables, which results in:

$$\frac{\partial \bar{\rho}}{\partial t} + \frac{\partial}{\partial x_i}(\bar{\rho}\tilde{v}_i) = 0 \tag{2.1}$$

$$\frac{\partial}{\partial t}(\bar{\rho}\tilde{v}_i) + \frac{\partial}{\partial x_j}(\bar{\rho}\tilde{v}_j\tilde{v}_i) = -\frac{\partial \bar{p}}{\partial x_i} + \frac{\partial}{\partial x_j}(\tilde{\tau}_{ij} - \overline{\rho v_i'' v_j''}) \tag{2.2}$$

$$\frac{\partial}{\partial t}(\bar{\rho}\tilde{E}) + \frac{\partial}{\partial x_j}(\bar{\rho}\tilde{v}_j\tilde{H}) = \frac{\partial}{\partial x_j}\left(k\frac{\partial \tilde{T}}{\partial x_j} - \overline{\rho v_j'' h''} + \overline{\tau_{ij} v_i''} - \overline{\rho v_j'' K}\right) + \frac{\partial}{\partial x_j}\left[\tilde{v}_i\left((\tilde{\tau}_{ij} - \overline{\rho v_i'' v_j''})\right)\right] \tag{2.3}$$

where $\bar{\rho}$ represents the mean density, $\tilde{v}_i$ is the mean velocity, in which the indicial notation is used together with Einstein's implicit summation convention for repeated indices, $\bar{p}$ is the mean pressure, h is the enthalpy, k is the thermal conductivity coefficient, and K is the turbulent kinetic energy. Here, the bar denotes the Reynolds-averaged values, the tilte represents the Favre-averaged values, and the double prime is used for fluctuating parts. The transfer of momentum due to turbulent fluctuations based on the Boussinesq eddy-viscosity hypothesis, which assumes a linear relationship between the turbulent shear stress tensor and the mean strain rate (Blazek, 2015), is defined as:

$$\tau_{ij}^F = -\overline{\rho \check{v}_i'' v_j''} = 2\mu_{tur}\tilde{S}_{ij} - \left(\frac{2\mu_{tur}}{3}\right)\frac{\partial \tilde{v}_k}{\partial x_k}\delta_{ij} - \frac{2}{3}\overline{\rho}\tilde{K}\delta_{ij} \tag{2.4}$$

where τ_{ij}^F, μ_{tur}, $\tilde{S}_{ij}$ and $\tilde{K}$ represent the Favre-averaged Reynolds stress tensor, eddy viscosity, the Favre-averaged strain rate and the Favre-averaged turbulent kinetic energy, respectively.

2.2.2 Spalart-Allmaras (SA) turbulent model

The development of RANS equations yields six extra unknowns called Reynolds stresses. Therefore, additional turbulent models are required to solve these terms. In this work, the one-equation Spalart-Allmaras turbulence model is used without any transition model, mainly because transition tends to occur close to the leading edge on a rough airfoil. The SA model, as implemented into the open-source code SU2 (Palacios et al., 2013), is presented by (Philippe Spalart & Steven Allmaras, 1992) making use of the Boussinesq hypothesis as follows:

$$\frac{\partial \hat{v}}{\partial t} + v_j\frac{\partial \hat{v}}{\partial x_j} = c_{b1}(1-f_{v2})\hat{S}\hat{v} - \left[c_{\omega 1}f_\omega - \frac{c_{b1}}{\kappa^2}f_{v2}\right]\left(\frac{\hat{v}}{d}\right)^2 + \frac{1}{\sigma}\left[\frac{\partial}{\partial x_j}\left((v+\hat{v})\frac{\partial \hat{v}}{\partial x_j}\right) + c_{b2}\frac{\partial \hat{v}}{\partial x_i}\frac{\partial \hat{v}}{\partial x_i}\right] \tag{2.5}$$

where $\hat{v}$ is the eddy-viscosity variable (Blazek, 2015).

For the turbulent viscosity:

$$\mu_{tur} = \rho\hat{v}f_{v1}, \quad f_{v1} = \frac{\chi^3}{\chi^3+c_{v1}^3}, \quad \chi = \frac{\hat{v}}{v}, \quad v = \frac{\mu_{dyn}}{\rho} \tag{2.6}$$

where the production term is $\hat{S} = |\vec{\omega}| + \frac{\hat{v}}{\kappa^2 d^2}f_{v2}$, $\vec{\omega} = \nabla\times\vec{v}$ is the fluid vorticity, d is the distance to the nearest wall, and $f_{v2} = 1 - \frac{\chi}{1+\chi f_{v1}}$; $f_\omega = g\left[\frac{1+c_{\omega 3}^6}{g^6+c_{\omega 3}^6}\right]^{1/6}$, where $g = r + c_{\omega 2}\left(r^6 - r\right)$ and $r = \frac{\hat{v}}{\hat{S}\kappa^2 d^2}$. The closure constants are:

$$\sigma = \frac{2}{3}, \; c_{b1} = 0.135, \; c_{b2} = 0.622, \; \kappa = 0.41, \; c_{\omega1} = \frac{c_{b1}}{\kappa^2} + \frac{1+c_{b2}}{\sigma}, \; c_{\omega2} = 0.3, \; c_{\omega3} = 2, \; c_{v1} = 7.1 \quad (2.7)$$

The dynamic viscosity can be calculated based on the Sutherland law and reference values, $\mu_{ref} = 1.716 \times 10^{-5} \, kg/ms$, $T_{ref} = 273.15K$ and $Su = 110.4K$. Hence:

$$\mu_{dyn} = \mu_{ref} \left(\frac{T}{T_{ref}} \right)^{3/2} \frac{T_{ref} + Su}{T + Su} \qquad (2.8)$$

where the value of T is obtained from the energy equation and the enthalpy definition, $H = \rho C_p T$.

2.2.3 Extension of the Spalart-Allmaras model (Rough SA)

The technique used to evaluate roughness effects in this thesis are based on the equivalent sand-grain roughness (k_s), proposed by (Schlichting, 1937), which is an idealized roughness height that represent the height of a sand grain from (Nikuradse, 1933)'s experiments. The commonly used correlation proposed by (Dirling, 1973) to translate topological features into k_s is summarized below:

$$\begin{aligned} k_s / k &= 0.0164\lambda^{3.78}, \; \lambda < 4.93 \\ k_s / k &= 139\lambda^{-1.90}, \; \lambda > 4.93 \end{aligned} \qquad (2.9)$$

where: k_s is the equivalent sand-grain roughness height, k is the mean roughness height, and λ is the roughness shape parameter defined as:

$$\lambda = (r_0 / k)(A_p / A_s)^{-4/3} \qquad (2.10)$$

where: r_0 / k is the spacing parameter, with r_0 being the mean distance between roughness elements; A_p is the projected area in the direction of the freestream velocity vector; and A_s is the windward surface area of the element seen by the flow.

The extension of the Spalart-Allmaras model to consider roughness effects, herein called rough SA, is presented in (Aupoix & Spalart, 2003). In this model, the distance function is increased in relation to the SA standard version

$$d_{new} = d + 0.03k_s \tag{2.11}$$

where d is the (original) distance to the nearest wall, and k_s is the conventional equivalent sand-grain roughness height. For uniform k_s, the new distance replaces all d in the original model. The χ becomes

$$\chi = \frac{\hat{v}}{v} + c_{R1}\frac{k_s}{d_{new}} \tag{2.12}$$

with $c_{R1} = 0.5$. As $\hat{S}$ is not affected, f_{v2} becomes

$$f_{v2} = 1 - \frac{\hat{v}}{v + \hat{v}f_{v1}} \tag{2.13}$$

Then, the wall boundary condition $\hat{v}_{wall} = 0$ is replaced by

$$\left(\frac{\partial \hat{v}}{\partial \vec{n}}\right)_{wall} = \frac{\hat{v}_{wall}}{0.03k_s} \tag{2.14}$$

where $\vec{n}$ is the outside normal to the wall vector.

2.2.4   Large Eddy Simulation (LES)

According to Blazek (2015), the more universal aspect of small turbulent structures has led researchers to the idea of resolving the large, energy-carrying structures, and of modeling the effects of the small ones, which is computationally considerably less expensive than the DNS. In this way, a low-pass spatial filtering of the Navier-Stokes, named Large Eddy Simulation (LES), was proposed by Orszag and Patterson (1972). In this approach, the large-scale three-

dimensional unsteady turbulent motions are directly solved, whereas the smaller scales are modeled by a sub-grid scale model (Zhiyin, 2015). Figure 2-3 illustrates the mentioned filtering process, in which the eddies are represented in blue. As seen, the eddies that are larger than the grid cells are filtered and resolved (Grid Scale), while the smaller ones are modeled (Sub-Grid Scale).
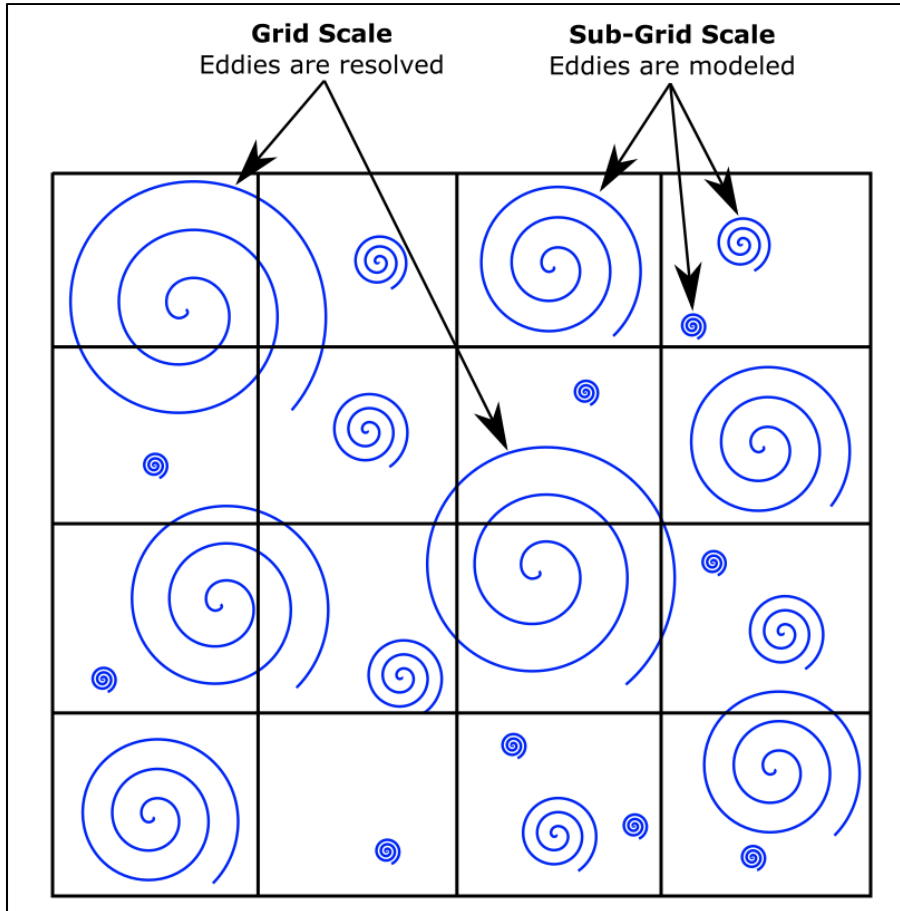
Figure 2-3 Grid Scale (GS) and Sub-Grid Scale (SGS)

In more refined meshes, a higher number of time-dependent eddies is directly solved, which results in an improved fidelity of predictions. On the other hand, as simulations approaches DNS for highly refined meshes, computational cost, and simulation time are massively increased. Therefore, the same study case that takes a couple of hours using RANS models could take several weeks when LES is used. For instance, the iced model 5-6 airfoil simulations of this work lasted around 19 hours using RANS, whereas it consumed around 478 hours (~20

days) when DDES (RANS/LES) was used. Both simulations used 288 CPU cores of the Cedar cluster of Compute Canada. Each node used of the cluster has 48 cores provided by 2 intel 8260 cascade lake at 2.4 GHz.

2.2.5 Delayed Detached Eddy Simulation and roughness

The DES proposed to switch from RANS to LES model is based on a modified length scale definition $\overline{d}$, used instead of the distance from the nearest wall, d, in the SA model (Spalart et al., 1997) . The length scale is based on the local maximum grid spacing Δ :

$$\overline{d} = \min(d, C_{DES}\Delta) \tag{2.15}$$

$$\Delta = \max(\Delta_x, \Delta_y, \Delta_z) \tag{2.16}$$

The value of $C_{DES} = 0.65$ is obtained after calibration on isotropic turbulence. Usually, the maximum grid spacing should be larger than the boundary layer because the elements near the wall are highly stretched in the streamwise direction for most aerodynamic flows. However, in some cases, the maximum grid spacing could be smaller than the boundary layer, and lead to activation of LES inside the attached boundary layer region . In order to prevent this situation, (Spalart et al., 2005) created the Delayed Detached Eddy Simulation (DDES) model, in which a new length scale definition is proposed:

$$\tilde{d} = d - f_d \max(0, d - C_{DES}\Delta) \tag{2.17}$$

$$f_d = 1 - \tanh((8r_d)^3), \ r_d = \frac{\nu + \hat{\nu}}{\sqrt{U_{i,j}U_{i,j}\kappa^2 d^2}} \tag{2.18}$$

where $U_{i,j}$ is the velocity gradient, κ is the Kármán constant. The function f_d is zero in RANS region.

As already mentioned, the Delayed Detached Eddy Simulation (DDES) model (Spalart et al., 2005) is based on a modified length scale definition, $\tilde{d} = d - f_d \max(0, d - C_{DES}\Delta)$, used instead of the distance from the nearest wall, d, in the SA model. The modified length scale is responsible for switching between RANS and LES. When in RANS, $f_d = 0$, and $\tilde{d} = d$, thus, in order to account for roughness, d is replaced by $d_{new} = d + 0.003k_s$ herein.

2.2.6   Shear-Layer Adapted DDES

In order to improve the slow transition between RANS/LES, which is commonly called "grey area", (Shur et al., 2015) presented the Shear-layer Adapted model, which proposes a new length scale definition that tries to correct the anisotropic grid cell effects on the RANS/LES transition. The length scale considers the direction of the vorticity vector. For a cell with the center vector $\vec{r}$ and vertices located at $\vec{r}_n$, and n being the number of element vertices (8 for hexahedral cell), the definition is

$$\tilde{\Delta}_\omega = \frac{1}{\sqrt{3}} \max_{n,m=1,8} \left| \vec{I}_n - \vec{I}_m \right|, \ \vec{I}_n = \vec{n}_\omega \times \vec{r}_n \tag{2.19}$$

where $\vec{n}_\omega$ is the unit vector aligned with the vorticity vector. The length scale is further corrected to facilitate the Kelvin–Helmholtz (KH) instability, which is the effect caused by the strongly inflectional profile of separated shear layers due to friction velocity:

$$\Delta = \Delta_{SLA} = \tilde{\Delta}_\omega F_{KH}\left(\langle VTM \rangle\right) \tag{2.20}$$

The F_{KH} function depends on the average values of VTM (Vortex Tilting Measure) over the current and closest neighboring cells. The piecewise linear function is defined as

$$F_{KH}\left(\langle VTM \rangle\right) = \max\left\{ F_{KH}^{\min}, \min\left\{ F_{KH}^{\max}, F_{KH}^{\min} + \frac{F_{KH}^{\max} - F_{KH}^{\min}}{a_2 - a_1}\left(\langle VTM \rangle - a_1\right) \right\} \right\} \tag{2.21}$$

Here, $F_{KH}^{max} = 1.0$, $F_{KH}^{min} = 0.1$, $a_1 = 0.15$, and $a_2 = 0.3$. Finally, the definition of VTM is

$$VTM = \frac{\sqrt{6}\left|\left(\hat{S}\cdot\vec{\omega}\right)\times\vec{\omega}\right|}{\omega^2\sqrt{3tr(\hat{S}^2)-\left[tr(\hat{S})\right]^2}}\max\left\{1,\left(\frac{v^*}{V_{tur}}\right)\right\}, v^* = 0.2v \qquad (2.22)$$

2.2.7   Boundary conditions

According to Blazek (2015), regardless of the method used to solve the Navier-Stokes equations, suitable initial and Boundary Conditions (BC) must be defined in order to avoid inaccurate simulation of the real system. The Initial Condition (IC) defines the state of the fluid at $t=0$ or at the first step of an iterative scheme, and it can be prescribed as values of free-stream pressure, density and velocity components. Still according to the author, the boundary conditions are used because only a certain part of the physical domain is used in numerical simulations. Therefore, values of the physical quantities must be specified on the artificial boundaries. The different initial conditions and boundary conditions used in this work are presented in each study case throughout the document. Nevertheless, we summarized them in this section.

In our study, farfield BCs are used to define the boundaries of the domain for the numerical simulations of external-flow study cases, in which freestream values are prescribed. For the spanwise plans (side walls), two different BCs were defined in the study cases, periodic BC and symmetric BC. In the periodic BC, one periodic side wall is transformed into the other side wall by pure coordinate translation (Blazek, 2015). In the symmetric BC, both side walls are symmetrical, and the following conditions must be met. First, the velocity normal to the symmetric boundary must be zero. Second, the following gradients must be zero, the gradient of a scalar quantity normal to the boundary, the gradient of the tangential velocity normal to the boundary, and the gradient of the normal velocity along the boundary (Blazek, 2015). For internal flows, inlet BC are defined, in which total pressure and total temperature are imposed;

and for the outlet BC, the static pressure is imposed. For the study cases with rough surfaces, roughness is imposed by defining the equivalent sand grain roughness height (k_s).

Static temperature (T), Mach number (Ma) and Reynolds number (Re) are directly defined on the configuration file of SU2. However, other parameters must be previously calculated. In this way, velocity can be calculated using:

$$v = Ma\sqrt{\gamma RT} \tag{2.23}$$

where γ is the heat capacity ratio, and R is the specific gas constant for air. Total pressure and total temperature are calculated using:

$$p_{total} = p\left(1 + \frac{\gamma - 1}{2}Ma^2\right)^{\frac{\gamma}{\gamma-1}} \tag{2.24}$$

and

$$T_{total} = T\left(1 + \frac{\gamma - 1}{2}Ma^2\right) \tag{2.25}$$

The ρ can be obtained using the Reynolds number equation:

$$\rho = \frac{\text{Re}\,\mu_{dyn}}{vL} \tag{2.26}$$

where L is a characteristic linear dimension.

2.3   Numerical method

The 3D flows are modeled by the compressible, turbulent Navier-Stokes equations, expressed in the conservative form (Molina et al., 2017). The vector of conservative variables is

$$\vec{U} = (\rho, \rho v_1, \rho v_2, \rho v_3, \rho E)^T \tag{2.27}$$

where ρ is the air density, E is the total energy per unit mass, and $\vec{v} = v_1, v_2, v_3 \in \square^3$ is the flow velocity in Cartesian coordinate system. Then, the NSE are expressed as a general convection diffusion equation

$$\partial_t \vec{U} + \nabla.\vec{F}^c - \nabla.\vec{F}^v = \vec{Q} \text{ on a domain } \Omega \in R^3, \ t > 0 \tag{2.28}$$

in which $\vec{U}$ represents the vector of state variables, $\vec{F}^c(\vec{U})$ are the convective fluxes, $\vec{F}^v(\vec{U})$ are the viscous fluxes and $\vec{Q}(\vec{U})$ is a generic source term. Thus, the convective and viscous fluxes are respectively:

$$\vec{F}_i^c = \begin{pmatrix} \rho v_i \\ \rho v_i v_1 + P\delta_{i1} \\ \rho v_i v_2 + P\delta_{i2} \\ \rho v_i v_3 + P\delta_{i3} \\ \rho v_i H \end{pmatrix} \tag{2.29}$$

$$\vec{F}_i^v = \begin{pmatrix} \cdot \\ \tau_{i1} \\ \tau_{i2} \\ \tau_{i3} \\ v_j \tau_{ij} + \mu_{tot}^* C_P \partial_i T \end{pmatrix}, \text{ for i=1,2,3} \tag{2.30}$$

where P is the static pressure, which under the assumption of a perfect gas can be determined from $P = (\gamma-1)\rho[E - 0.5(\vec{v}.\vec{v})]$, H is the fluid enthalpy, $C_P = \gamma R/(\gamma-1)$ is the specific heat of air at constant pressure, $T = \dfrac{P}{\rho R}$ is the temperature, δ_{ij} is the Kronecker delta function, the viscous stresses are written as:

$$\tau_{ij} = \mu_{tot}(\partial_j v_i + \partial_i v_j - \frac{2}{3}\delta_{ij}\nabla.\vec{v}), \text{ with } \mu_{tot} = \mu_{dyn} + \mu_{tur} \tag{2.31}$$

$$\mu_{tot}^* = \frac{\mu_{dyn}}{\mathrm{Pr}_d} + \frac{\mu_{tur}}{\mathrm{Pr}_t} \tag{2.32}$$

where Pr_d and Pr_t are dynamic and turbulent Prandtl numbers. The dynamic viscosity, μ_{dyn}, is assumed to satisfy Sutherland's law (White & Corfield, 2006). The turbulent viscosity, μ_{tur}, is obtained from the one equation SA turbulent model (P. Spalart & S. Allmaras, 1992). Moreover, in the framework of the general convection diffusion equation, the SA equation can be rewritten as:

$$\vec{F}^c = \vec{v}\hat{v},\ \vec{F}^v = \frac{v+\hat{v}}{\sigma}\Delta\hat{v},\ Q=c_{b1}(1-f_{v2})\hat{S}\hat{v}+c_{b2}\frac{\partial\hat{v}}{\partial x_i}\frac{\partial\hat{v}}{\partial x_i}-\left[c_{\omega1}f_\omega-\frac{c_{b1}}{\kappa^2}f_{v2}\right]\left(\frac{\hat{v}}{d}\right)^2 \quad (2.33)$$

The boundary conditions for smooth walls are

$$\hat{v}_{wall} = 0 \text{ and } \hat{v}_{farfield} = 3v \quad (2.34)$$

For the roughness version of the SA, the distance from the nearest wall d is replaced by $d_{new} = d + 0.03k_s$, and the boundary conditions become:

$$\left(\frac{\partial\hat{v}}{\partial\vec{n}}\right)_{wall} = \frac{\hat{v}_{wall}}{0.03k_s} \quad (2.35)$$

where $\vec{n}$ is the outside normal to the wall vector.

The Partial Differential Equations (PDE) are discretized on unstructured meshes using the finite volume method. The second order finite volume scheme is applied using a standard edge-based data structure on dual grid. The control volumes are constructed using a median-dual vertex-based scheme (Palacios et al., 2013). The general convection diffusion equations are, after integration over the dual control volume Ω_i, surrounding vertex i

$$\int_{\Omega_i}\frac{\partial U}{\partial t}d\Omega = -\sum_{j\in\square(i)}\left(\tilde{F}^c_{ij}+\tilde{F}^v_{ij}\right)\Delta S_{ij}-Q|\Omega_i| \quad (2.36)$$

The convective and viscous fluxes, $\tilde{F}_{ij}^{c}$ and $\tilde{F}_{ij}^{v}$ are the numerical approximations of the fluxes projected along an edge. ΔS_{ij} is the area of the face associated with the edge ij and Ω_{i} is the set of vertices neighbor to vertex i.

The viscous and convective fluxes are evaluated at the midpoint of an edge. The viscous fluxes are evaluated using flow quantities and their first derivatives at the faces of the dual control volume. The spatial gradient is evaluated using the weighted least-squares approach at vertices, and then, averaged to obtain the gradient at the dual control volume face. Source terms are approximated using piecewise constant reconstruction within each dual control volume. The convective fluxes for the Navier-Stokes equations are obtained using two schemes along this work, the Roe Scheme (for RANS simulations) and the High-Resolution Simple Low Dissipation Advection Upstream scheme (HR-SLAU2) (for DDES simulations) from the AUSM-family (Advection Upstream Splitting Method) (Kitamura, 2016; Kitamura & Hashimoto, 2016). According to Blazek (2015), the Roe scheme is the most widely used approach on unstructured grids because of its excellent resolution of boundary layers. This scheme is presented in (Palacios et al., 2013) as:

$$\tilde{F}_{ij}^{c} = \left(\frac{\vec{F}_{i}^{c} + \vec{F}_{j}^{c}}{2} \right) \cdot \vec{n}_{ij} - \frac{1}{2} P |\Lambda| P^{-1} \left(U_{i} - U_{j} \right) \tag{2.37}$$

where i and j represent the position of nodes. Thus, U_{i} and U_{j} are the conserved variables at nodes i and j, respectively. $\vec{F}^{c}$ is the convective flux, P is the matrix of eigenvectors of the convective flux Jacobian Matrix $\vec{A}^{c}$ constructed using the Roe-average variables and projected in the $\vec{n}_{ij}$ direction, which is outward vector associated with the face between nodes i and j. $|\Lambda|$ is the diagonal matrix with entries corresponding to the absolute values of the eigenvalues of the flux Jacobian matrix.

According to Winkler et al. (2012), low dissipation schemes are required in the LES portion of hybrid models. Inspired by the reduced dissipation approach presented by Winkler et al.

(2012) for the Roe scheme, (Kitamura & Hashimoto, 2016) proposed the HR-SLAU2, which the author presents as:

$$\tilde{F}_{ij}^c = \frac{\dot{m} + |\dot{m}|}{2}\vec{\Psi}^+ - \frac{\dot{m} - |\dot{m}|}{2}\vec{\Psi}^- + \tilde{p}\vec{N} \tag{2.38}$$

$$\vec{\Psi} = (1, \upsilon_1, \upsilon_2, \upsilon_3, H)^T, \qquad \vec{N} = (0, n_1, n_2, n_3, 0)^T \tag{2.39}$$

where, $\vec{n} = (n_1, n_2, n_3)$ are Cartesian components of a normal vector from the left to the right, $\vec{\upsilon} = (\upsilon_1, \upsilon_2, \upsilon_3)$ is the velocity vector, and $\dot{m}$ is the mass flux, defined as:

$$\dot{m} = \frac{1}{2}\left\{ \rho_L\left(V_{nL} + \left|\overline{V}_n\right|^+\right) + \rho_R\left(V_{nR} + \left|\overline{V}_n\right|^-\right) - \frac{\chi}{\overline{c}}\Delta p \right\} \tag{2.40}$$

$$V = \vec{\upsilon} \cdot \vec{n} = n_1\upsilon_1 + n_2\upsilon_2 + n_3\upsilon_3 \tag{2.41}$$

$$\left|\overline{V}_n\right|^+ = (1 - g)\left|\overline{V}_n\right| + g\left|V_{nL}\right| \tag{2.42}$$

$$\left|\overline{V}_n\right|^- = (1 - g)\left|\overline{V}_n\right| + g\left|V_{nR}\right| \tag{2.43}$$

$$\left|\overline{V}_n\right| = \frac{\rho_L\left|V_{nL}\right| + \rho_R\left|V_{nR}\right|}{\rho_L + \rho_R} \tag{2.44}$$

$$g = -\max\left[\min(M_L, 0), -1\right] \cdot \min\left[\max(M_R, 0), 1\right] \tag{2.45}$$

$$\chi = (1 - \overline{M})^2 \tag{2.46}$$

$$M = \frac{\upsilon}{\overline{c}} \tag{2.47}$$

$$\overline{c} = \frac{c_L + c_R}{2} \tag{2.48}$$

and, the pressure flux is:

$$\tilde{p} = \frac{P_L + P_R}{2} + \frac{P^+\big|_{\alpha=0} - P^-\big|_{\alpha=0}}{2}(P_L - P_R) + \sigma\left(\sqrt{\frac{\bar{v}_L^2 + \bar{v}_R^2}{2}}(P^+\big|_{\alpha=0} + P^-\big|_{\alpha=0} - 1)\right)\overline{\rho c} \quad (2.49)$$

with

$$P^\pm\big|_{\alpha=0} = \begin{cases} \frac{1}{2}(1 \pm sign(M)) & if \quad |M| \geq +1 \\ \frac{1}{4}(M \pm 1)^2(2 \mp M) \pm \alpha M(M^2 - 1)^2 & if \quad \text{otherwise} \\ 0 & if \quad M_L \leq -1 \end{cases} \quad (2.50)$$

$$\sigma = \sigma_{FD} = \max(\sigma_{\min}, 1 - f_d) \quad (2.51)$$

The f_d parameter is equal to zero in the RANS region, and to one in the LES region, thus, the σ parameter smoothly evolves from RANS to LES regions.

As already mentioned, the DDES model is based on a modified length scale definition, $\tilde{d} = d - f_d \max(0, d - C_{DES}\Delta)$, used instead of the distance from the nearest wall, d in the SA model. The modified length scale is responsible for switching between RANS and LES. When in RANS, $f_d = 0$, and consequently $\tilde{d} = d$, then, due to the roughness implementation, d is replaced by the increased $d_{new} = d + 0.03k_s$, which considers the role of the equivalent sand-grain roughness height, k_s.

This formulation has been implemented into an open-source code called Stanford University Unstructured, SU2 (Palacios et al., 2013). The model will be called SU2$_{rough}$ herein, and it is expected to improve the fidelity of estimations in which roughness is considered.

2.4   Post-processing approaches

2.4.1   Statistics

As already mentioned, one of the main challenges faced in CFD simulations is how to 'solve' turbulent flows in which a wide range of length and time scales is present. The time-averaged process offered by RANS models has been widely used for several years. In this process, the instantaneous results are not considered, and only the time-averaged values are generated. One of the main advantages of this model is the reduced computational cost and amount of data produced. However, as stated earlier, RANS is not suitable for simulations of massive-separated flows.

The presented hybrid RANS/LES models offer improved results in simulations of massive-separated flows, in which LES is active. However, this improvement translates into exponentially higher computational cost as well as an enormous amount of data to be assessed. For instance, in our NACA 0012 in deep stall study case, a total of 16000 iterations with a physical time step of $\Delta t = 0.15$ milliseconds, and 20 inner iterations were used. Statistics were calculated from the last 10000 iterations. Each flow file solution generated, at each iteration, had around 3 Gigabytes. Therefore, the total storage space required for the solutions (disregarding other files also generated) would be around 30 Terabytes. Although the storage issue could be solved by using high-capacity hard disk drives, working with these numerous large files becomes extremely challenging and time-consuming. Therefore, to reduce the amount of data, instantaneous solution files were generated at every interval of 30 iterations, which resulted in around 330 files, and a total of around 1 Terabyte of occupied space. Averaging capabilities have been added to SU2, which reduces further the number of files for post-processing.

For the statistics calculation as well as data analysis and visualization (post-processing) performed in this work, we used three distinct software packages, MatLab from MathWorks, Excel from Microsoft, and Paraview from Kitware. The time-averaged global aerodynamic coefficients, such as C_l, C_d, C_p and C_f, were performed as follow. First, we evaluated our results to make sure we get values after the initial oscillating regions. In this way, the iterations were accompanied until the greater oscillations were reduced, as illustrated in the backward facing step example shown in Figure 2-4. As shown, the instantaneous drag coefficient (C_d) is presented along the total simulation time, 44.2 seconds or 96000 iterations. An oscillating region is clearly seen in the first 40000 iterations. After this point, the oscillation is reduced, and values fluctuate around 1.018, which is the mean value represented in green in the zoomed-in graph of Figure 2-5. The dispersion of values is represented by the standard deviation, which is 0.021, and is shown in pink. This analysis was performed for all unsteady study cases, and then, the time-averaged values were calculated.

Additionally, since turbulence is a three-dimensional phenomenon (Tabatabaian, 2015), the time-averaged values obtained in the previous steps presented variations in the spanwise direction. Therefore, in our unsteady three-dimensional study cases, values in the spanwise direction were space averaged. Thus, the final aerodynamic coefficients presented throughout this document is obtained after two averaging processes, time (temporal) and space (spatial) averaging, unless stated otherwise.
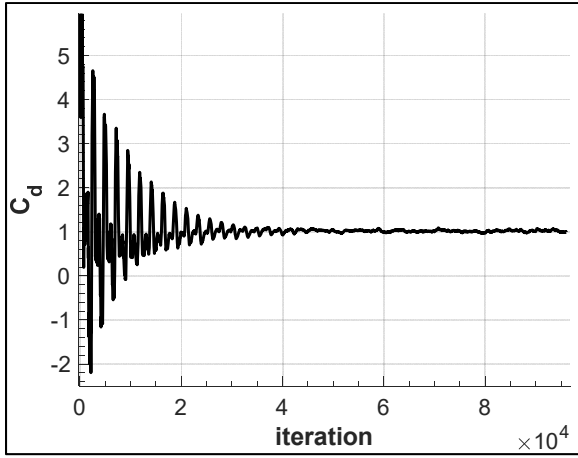
Figure 2-4 Evolution of Drag coefficient along total number of iterations
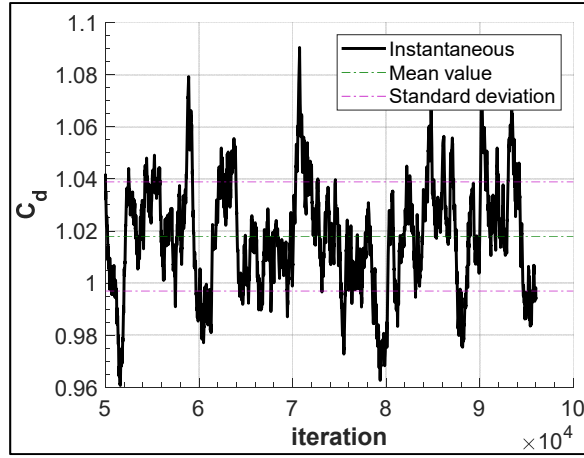
Figure 2-5 Zoomed-in evolution of Drag coefficient along statistical iterations

2.4.2 Discrepancies and errors

In order to evaluate the quality of our estimations, a verification and validation process is performed in CHAPTER 3. In this way, our results are confronted with numerical and experimental data from the literature so that discrepancies and errors could calculated. One of the approaches used to present errors in the literature is the percent error (herein also called percent discrepancy when performing verification against numerical results), which is obtained from the multiplication of the relative error by 100. The relative error is the ratio:

$$\text{Relative error} = \frac{|\text{Exact Value} - \text{Approximation}|}{\text{Exact Value}} \qquad (2.52)$$

in which, $|\text{Exact Value} - \text{Approximation}|$ is called absolute error. Thus, the percent error is:

$$\delta = \left(\frac{|\text{Exact Value} - \text{Approximation}|}{\text{Exact Value}} \right) \cdot 100 \qquad (2.53)$$

Herein, the "Exact Value" represents the references used in this work, and the "Approximation" represents our estimations.

In order to calculate discrepancies and errors that better represent what it is being shown in our graphs, some sections will present a percent error in which the absolute error is scaled by the difference of the maximum and minimum values of a curve. Hence, the percent error becomes:

$$\delta = \left(\frac{|\text{Exact Value - Approximation}|}{\text{Maximum - Minimum}} \right) \cdot 100 \qquad (2.54)$$

For instance, the discrepancy or error of the pressure coefficient obtained using the backward facing step (Figure 3-31) is calculated using:

$$\delta C_f = \left(\frac{C_{f\_(estimated)} - C_{f\_(reference)}}{C_{f\max} - C_{f\min}} \right) \cdot 100 \qquad (2.55)$$

where $\Delta C_f = C_{f\max} - C_{f\min} = 0.0701$.

Whenever equation 2.53 is used throughout this document, the "Maximum - Minimum" is explicitly presented when introducing the graphs.

2.5   Summary

In this chapter, the problem of aircraft ice accretion was defined, and the governing equations of the models used in this thesis were presented. In this way, the commonly used RANS model was presented along with the extension of the SA turbulence model to consider roughness. Next, we illustrated the basic principles of LES, followed by an introduction of the hybrid DES and DDES model, which make use of RAN and LES. Then, a model intended to improve the transition between RANS/LES, called Shear-layer Adapted model, was introduced. Next, the numerical model used along with boundary conditions were presented. Finally, we discussed the statistics approach used herein as well as how errors were calculated. In the next chapter, we present the verification and validation process of the DDES model with roughness implemented.

CHAPTER 3

VERIFICATION AND VALIDATION OF NUMERICAL APPROACH

In this chapter, the roughness model implementation performed into SU2 code is verified and validated using RANS and DDES simulations to estimate aerodynamic parameters of flows over multiple study cases. The extension of the Spalart-Allmaras turbulence model (presented in 2.2.3) to consider roughness effects is used in our simulations. In sub-section 3.1, smooth and rough RANS simulations are verified and validated using a flat plate, a NACA 0012 airfoil, and a model 5-6 airfoil. Next, verification and validation of massive-separated-flow DDES simulations with the SLA-SGS model proposed by (Shur et al., 2015) combined with the low-dissipation scheme HR-SLAU2 is presented in subsection 3.2.

In order to facilitate the identification of the model active during the simulations throughout this document, the following nomenclature is used: *SU2-RANS$_{smooth}$* is used when RANS simulations are performed with roughness deactivated, while *SU2-RANS$_{rough}$* is used when roughness is activated. *SU2-RANS* is used for the general case in which both cases are treated. Similarly, *SU2-DDES$_{smooth}$* is used when roughness is deactivated, whereas *SU2-DDES$_{rough}$* is used when roughness is activated. *SU2-DDES* is used when both cases are treated. Finally, SU2$_{rough}$ is used for the code in general without considering the active model.

3.1   Smooth/Rough RANS

3.1.1   Smooth/Rough Flat plate

The schemes of the flat plate study cases are illustrated in Figure 3-1 and Figure 3-2. In Figure 3-1, a smooth flat plate is shown, whereas in Figure 3-2, a rough flat plate is illustrated. The flow enters the inlet with total pressure and temperature imposed, and it exits the outlet with static pressure imposed. For the verification of *SU2-RANS$_{smooth}$* estimations, results obtained from (Rumsey et al., 2018) are used as reference. In this way, flow parameters are defined as

$Ma = 0.2$, $Re = 5 \times 10^6$ based on a length of 1 m, $T = 300K$, and the heat flux is set to zero at the wall. Similarly, for the verification and validation of *SU2-RANSrough* estimations, numerical results are taken from (Knopp et al., 2009), and experimental results from (Blanchard, 1977). Hence, flow parameters are defined as $Ma = 0.131$ ($\vec{\upsilon} = 45$ m/s), $Re = 3 \times 10^6$ based on length of 1 m, free stream temperature is 293 K, total temperature is 294 K, total pressure is 102971 Pa, static pressure is 101744 Pa, and the heat flux is set to zero at the wall. For the roughness, (Blanchard, 1977) proposed an equivalent sand-grain roughness (k_s) of 0.85 mm, which was obtained based on the average height of the sand-grain paper employed, 0.425mm.

The grid used is the finest grid (545 x 385) among the ones provided by (Rumsey et al., 2018), in which a minimum spacing at the wall of $y = 5 \times 10^{-7}$ m is achieved. An average nondimensional wall distance ($y+$) of 0.1 and 0.045 are reached for the smooth and rough flat plate, respectively.
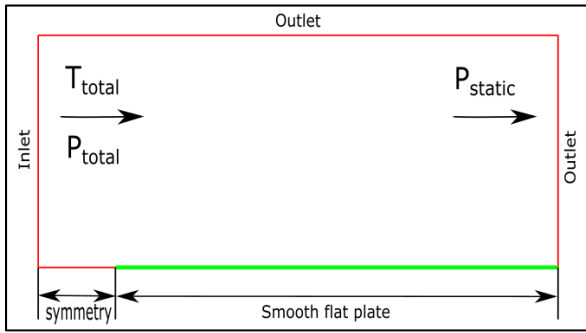
Figure 3-1 Scheme of the smooth flat plate   Figure 3-2 Scheme of the rough flat plate
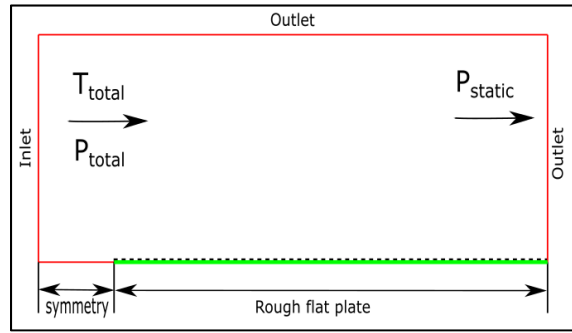
Figure 3-3 and Figure 3-4 present *SU2-RANS* estimations of the friction coefficient distribution (C_f) along smooth and rough flat plates, respectively. In Figure 3-3, *SU2-RANSsmooth* estimations are compared to results from (Rumsey et al., 2018), in which CFL3D and FUN3D RANS codes are used with the SA turbulence model. As seen, the three codes estimated very similar results. In Figure 3-4, *SU2-RANSrough* estimations are compared to Blanchard's experimental data (Blanchard, 1977) for validation, and to Knopp's numerical results (Knopp et al., 2009) for verification. For validation, percent errors are obtained using the general

equation 2.53. Thus, the percent error of the friction coefficient becomes

$$\delta C_f = \left(\frac{\left| C_{f\_(reference)} - C_{f\_(estimated)} \right|}{C_{f\,max} - C_{f\,min}} \right) \cdot 100, \text{ where } \Delta C_f = C_{f\,max} - C_{f\,min} = 0.0701.$$

As shown in Figure 3-4, *SU2-RANS*$_{rough}$ estimations slightly underestimates the friction coefficient, as compared to estimations presented by (Knopp et al., 2009). Nevertheless, when comparing numerical estimations with experimental results, (Knopp et al., 2009) estimations reach the largest error of 1.23% against 1.13% of *SU2-RANS*$_{rough}$. As our results were obtained neither using the same grid nor with the Edward modification version of SA (Edwards & Chandra, 1996), a small difference was expected.

Figure 3-3 Flat plate friction coefficient curve (smooth surface)
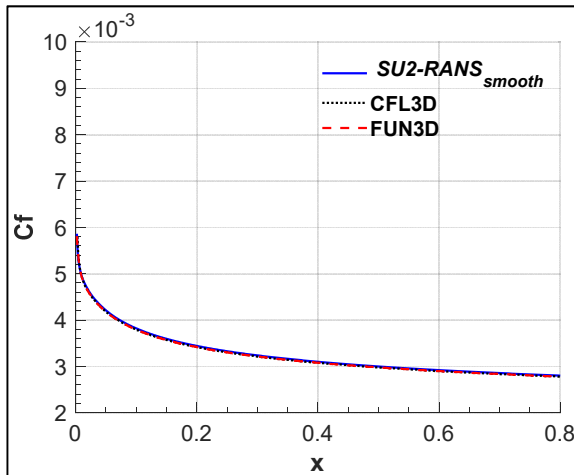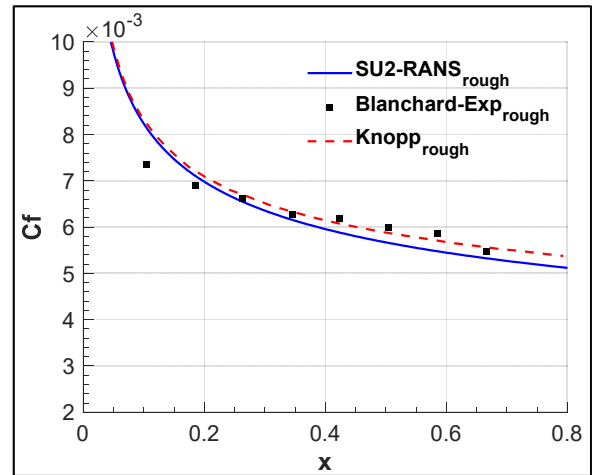

Figure 3-4 Flat plate friction coefficient curve (rough surface)

3.1.2 Smooth/Rough NACA 0012

In this study case, *SU2-RANS* estimations of lift coefficient and velocity profiles inside the boundary layer are evaluated and compared to numerical (Jespersen et al., 2016; Langel et al.,

2017; Mendez et al., 2015) and experimental (Gregory & O'Reilly, 1970; Kerho & Bragg, 1997; Ladson, 1988) results.

For the smooth NACA 0012 airfoil, the lift coefficient is estimated using *SU2-RANS$_{smooth}$*, and results are compared to estimations of two different codes, CFL3D and OVERFLOW, obtained from (Jespersen et al., 2016). The validation is performed using experimental results from (Gregory & O'Reilly, 1970; Ladson, 1988). In this way, the parameters are kept as they were used in (Jespersen et al., 2016), $Ma = 0.15$, $\text{Re} = 6 \times 10^6$ and $T = 300K$.

Five grids ("C-grid" type) ranging from the coarsest (113×33) to the finest (1793×513) were evaluated for these simulations. The finest grid counts 1025 points on the airfoil surface while the coarsest grid counts 65. As the two finest grids (1793×513 and 897×257) presented similar results, the 897×257 grid was chosen as a matter of faster processing time. The farfield boundary condition is located 500c away from the airfoil in order to minimize the issues associated with the boundaries. The minimum space from the wall to the grid is $y = 8.14 \times 10^{-7}$ m, and the average y^+ around the airfoil is 0.2.

For the rough NACA 0012 airfoil, two separated evaluations are performed, as done by (Mendez et al., 2015). First, *SU2-RANS$_{rough}$* estimations of lift coefficient are compared to numerical results produced by the WMB code used by (Mendez et al., 2015), and to experimental data from (Abbott et al., 1945). Mendez uses RANS simulations with two different models to take roughness into account, the extension of the k-ω-SST turbulence model (Hellsten & Laine, 1998) and the k-ω turbulence model (Knopp et al., 2009). For the experimental data, (Abbott et al., 1945) use a 24-inch-chord airfoil with 0.011-inch carborundum grains applied on the first 0.08c of the leading edge of the airfoil (Abbott et al., 1945). In our simulations, we use $\text{Re} = 6 \times 10^6$, $Ma = 0.15$, and $k_s / c = 6 \times 10^{-4}$ as in (Mendez et al., 2015). Next, for the evaluation of the velocity profiles inside the boundary layer, the experimental results obtained from (Kerho & Bragg, 1997), and the numerical estimations produced by (Langel et al., 2017) are used for comparisons. In the experiments, the

measurements were performed using a NACA 0012 airfoil with a chord of 0.5334 m, and a span of 0.8573 m. Strips tapes of *12.7×101.6 mm* (*0.5×4 in)* were used to simulate roughness. The tapes were 0.35 mm high and the roughness element's center-to-center distance was *1.3 mm*. The roughness was spread between $x/c = 0.00612 \; or \; x/s = 0.0150$ and $x/c = 0.0258 \; or \; x/s = 0.388$, which results in a length of *12.7 mm (1/2 in)*, as illustrated in the scheme of Figure 3-5. For the numerical estimations of (Langel et al., 2017), a modified version of the Langtry-Menter $\gamma - \tilde{Re}_{\theta t}$ transition model to account for roughness was used. The model was implemented into OVERFLOW-2.2k, and a $k_s / c = 6.56 \times 10^{-4}$ was chosen for their simulations.

Figure 3-5 Scheme of the study case used by (Kerho & Bragg, 1997)

Our numerical simulations are conducted at a Reynolds number of *1.25×10⁶*, as used by (Mendez et al., 2015) and (Langel et al., 2017). As shown in Figure 3-6, the computational domain is the same as the one presented for the smooth NACA 0012. The heat flux is set to zero at the wall, and the farfield boundary is located 500c away from the airfoil. Roughness is considered along the whole airfoil.

The grid used has 897×257 grid points, the closest point to the wall is $y = 8.14 \times 10^{-7}$ *m*, and the maximum $y+$ is *0.105*. The equivalent sand-grain roughness height was calculated making use of Dirling's correlations (equations 2.9 and 2.10), in which the parameter (A_p / A_s) was assumed to be 0.5, which resulted in a $k_s / c = 6.94 \times 10^{-4}$.
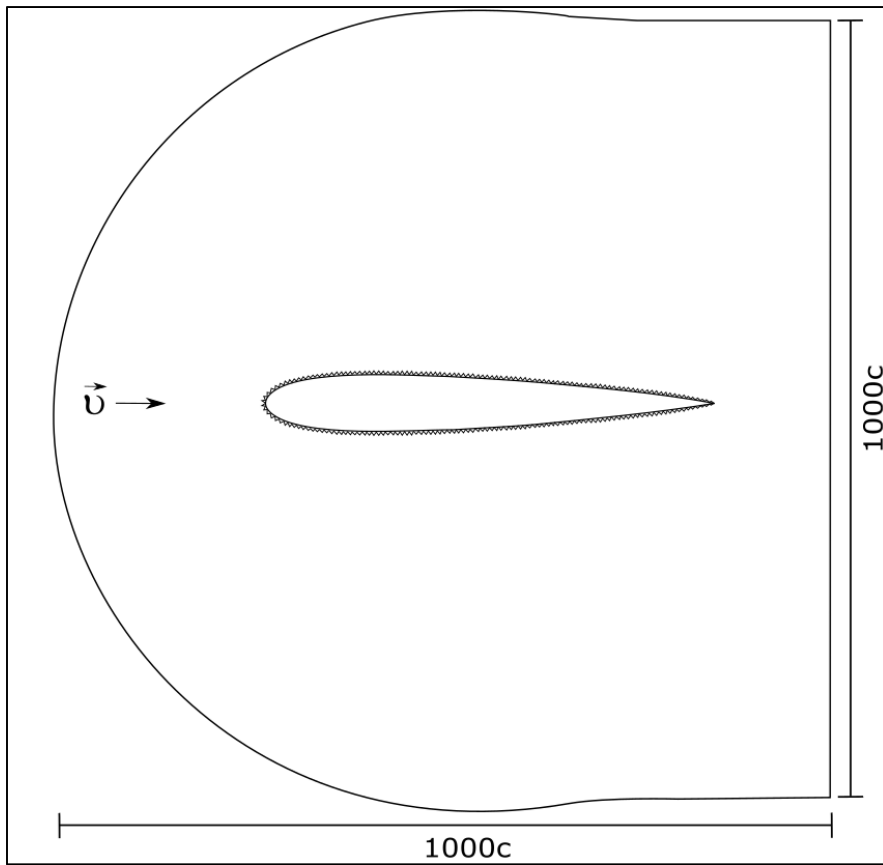
Figure 3-6 Scheme of the rough NACA 0012

Figure 3-7 and Figure 3-8 present the velocity streamlines of flows over smooth and rough NACA0012 airfoils at an angle of attack of 12 degrees. Both figures present the streamlines colored by the streamwise velocity, and the range of the legends are based on the maximum and minimum values of the smooth case. The smooth airfoil reaches a maximum streamwise velocity of 112.3 m/s, and a minimum value of -43.7 m/s. Whereas, the rough case presents reduced velocities of 100.8 and -35.7 m/s due to roughness effects. Maximum and minimum velocities are reached at leading edge of the airfoils. The minimum velocities are reached near the stagnation point, where the flow must contour the lower part of the airfoil to reach the upper region. When the upper region of the airfoil is finally reached, the maximum velocities are achieved.

When comparing both figures, the first noticeable difference caused by roughness effects is the thickening of the boundary layer, which results in trailing-edge separation and flow recirculation, as seen in Figure 3-8. These effects caused by roughness were also pointed out by (Bragg et al., 2005; Lynch & Khodadoust, 2001). In addition, (Bragg et al., 2005) highlights that these effects are manifested through modified skin friction and pressure distribution into performance degradation.
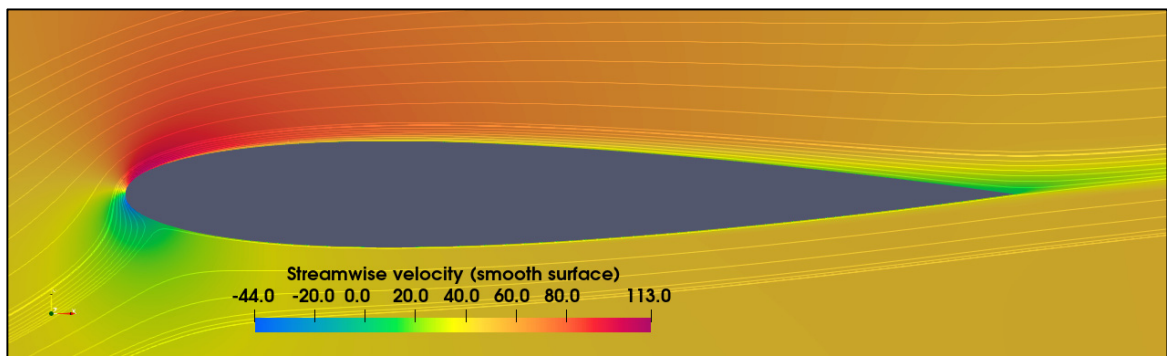
Figure 3-7 Velocity streamlines of flow over smooth NACA0012 airfoil at AoA=12º
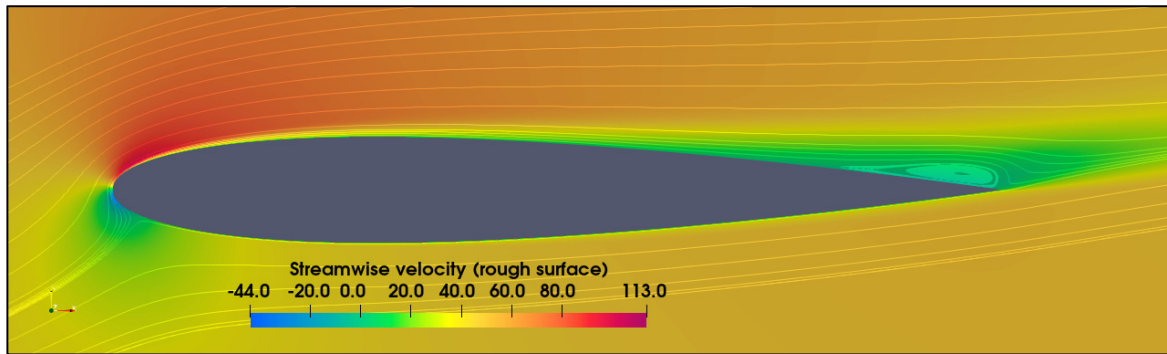
Figure 3-8 Velocity streamlines of flow over rough NACA0012 airfoil at AoA=12º

Figure 3-9 and Figure 3-10 present the variation of the lift coefficient as the AoA of the airfoil is increased. Numerical and experimental results of lift coefficient over the smooth NACA 0012 are presented in Figure 3-9. As shown, *SU2-RANS_{smooth}*, CFL3D and OVERFLOW almost perfectly match, and the maximum discrepancies between the results are inferior to 1%. When compared to experimental results, the maximum error is 2%, obtained with OVERFLOW at an angle of attack of 15 degrees, and the minimum error is 1.18%, achieved

by CFL3D. *SU2-RANSsmooth* presents a good estimation of the maximum lift coefficient, $C_{l(max)} = 1.66$, at 17 degrees, against $C_{l(max)} = 1.64$ in the experimental data, which results in an error of 1.2% . Figure 3-10 presents *SU2-RANSrough* estimations of lift coefficient over the rough NACA 0012. As seen, *SU2-RANSrough* estimations are globally closer to experimental data than Mendez's estimations using the WMB code. When estimating the $C_{l\max}$, *SU2-RANSrough* and WMB reach the same error of 7%, as compared to experiments.
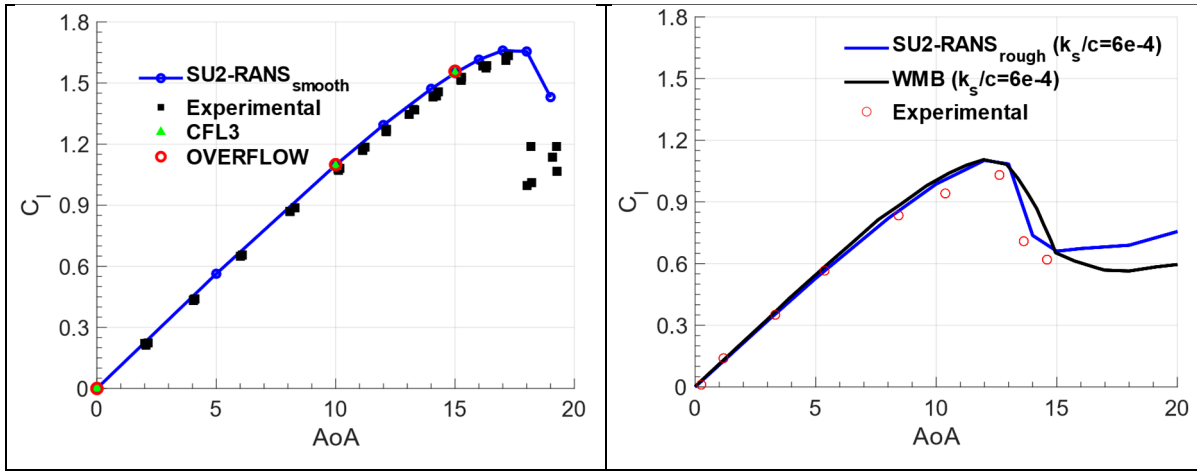
Figure 3-9 C_l for smooth-surface NACA0012 with $Ma = 0.15$, $\mathrm{Re} = 6 \times 10^6$, and $T = 300K$

Figure 3-10 C_l for rough-surface NACA0012 with $Ma = 0.15$, $\mathrm{Re} = 6 \times 10^6$, $T = 288.15K$, and $k_s / c = 6 \times 10^{-4}$

Figure 3-11-a to Figure 3-11-e depict the profiles of the nondimensional velocities ($\upsilon / \upsilon_\infty$) over the rough NACA 0012 at an AoA of zero degrees. Each figure represents a cut in the normal direction on the upper surface of the airfoil. Thus, the velocity profiles, which is perpendicular to the wall, is measured from point 0 (at the wall) up to 7×10^{-3} m in the normal direction. In the first region of the airfoil (Figure 3-11a), *SU2-RANSrough* estimations achieved better agreement with experimental results than the numerical reference. At $x/c = 0.05$, *SU2-RANSrough*, and the numerical reference agrees on estimations for values obtained at a distance superior to $y/c = 1.3 \times 10^{-3}$ from the airfoil. In the region below this distance, *SU2-RANSrough* performed better with a maximum error of 10.6% for velocity estimations, against an error of

15.7% of the numerical reference, when considering the same distance y/c of 9.2×10^{-4}. At $x/c=0.075$, *SU2-RANSrough* and the numerical reference achieved reduced errors globally, as shown in Figure 3-11b. *SU2-RANSrough* results of nondimensional velocities are slightly underestimated with a maximum error of 5.5% at $y/c=1.4\times10^{-3}$, whereas the numerical reference's results are overestimated with a maximum error of 6.6% at the same y/c. For the next cuts, the numerical reference estimations are slightly better than *SU2-RANSrough*'s, as shown in Figure 3-11c to Figure 3-11e. Nevertheless, the maximum difference between SU2 and the numerical reference along these cuts is inferior to 11%. This underestimation is probably caused by the fast thickening of the boundary layer due to the roughness effects.
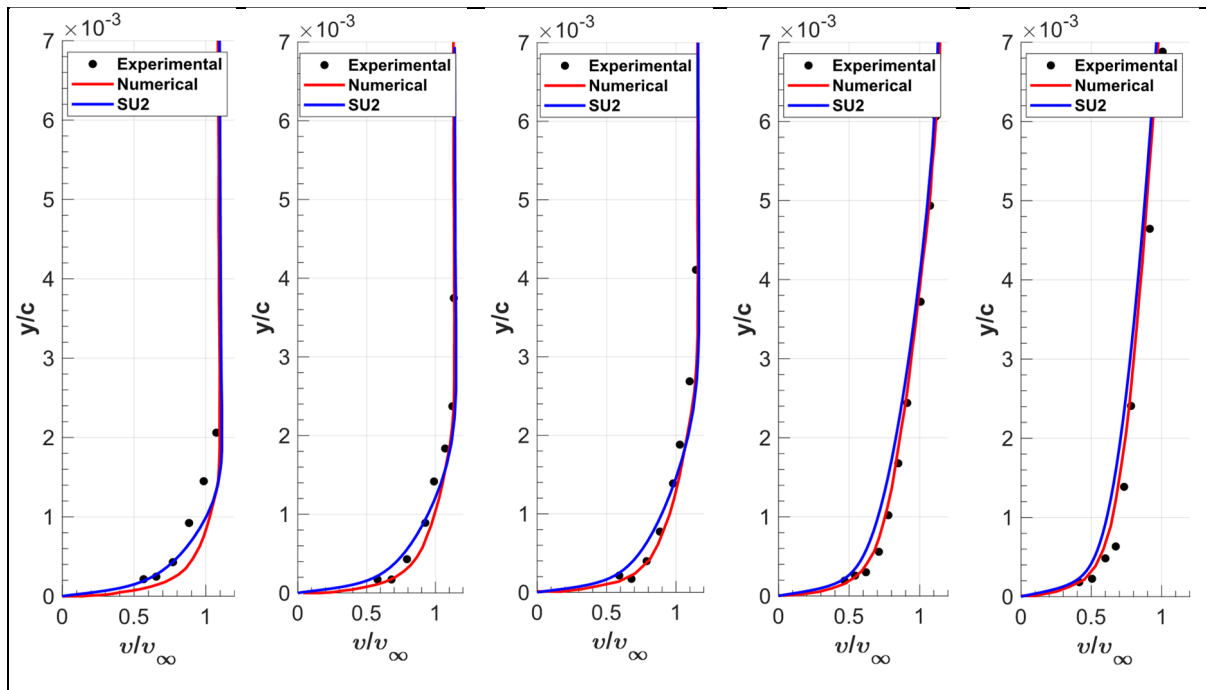
a) Velocity with cut at $x/c=0.05$ b) Velocity cut at $x/c=0.075$ c) Velocity with cut at $x/c=0.10$ d) Velocity with cut at $x/c=0.30$ e) Velocity with cut at $x/c=0.50$

Figure 3-11 Nondimensional velocity profiles (NACA 0012 Rough surface)

Considering the uncertainties involved in a transitional roughness regime, and the fact that the model implemented is not a transition model, *SU2-RANSrough* predictions are satisfactory when compared to Kerho's experimental data (Kerho & Bragg, 1997) and with numerical results

from (Langel et al., 2017). Therefore, these results show that SU2 roughness implementation behaves as expected, and that the code is applicable for the estimation of lift coefficient and velocity profiles over airfoils with rough surfaces.

3.1.3 Smooth iced model 5-6 (validation)/Rough iced model 5-6 (verification only)

In this study case, the flows over smooth and rough iced model 5-6 airfoils are evaluated with *SU2-RANS*. Experimental and numerical results are obtained from the final report (GARTEUR, 2003) of the GARTEUR Action Group. The airfoil studied represents an outer wing section of a transport aircraft. Figure 3-12 illustrates a typical glaze ice formation, in which the smooth ice is zoomed in on the left side, and the rough ice is zoomed in on the right side. The main airfoil model characteristics are chord of $c = 1$ m, thickness of $t/c = 10.6\%$, and span width of 0.4 m. The farfield boundary surface is a circle of diameter 44.39c defined in an unstructured grid with 2,329,960 cells and 1,781,409 points, as illustrated in Figure 3-13. The aerodynamic parameters are $Ma = 0.2$ and $\mathrm{Re} = 3 \times 10^6$. The flow is periodic along the spanwise direction (y-axis).
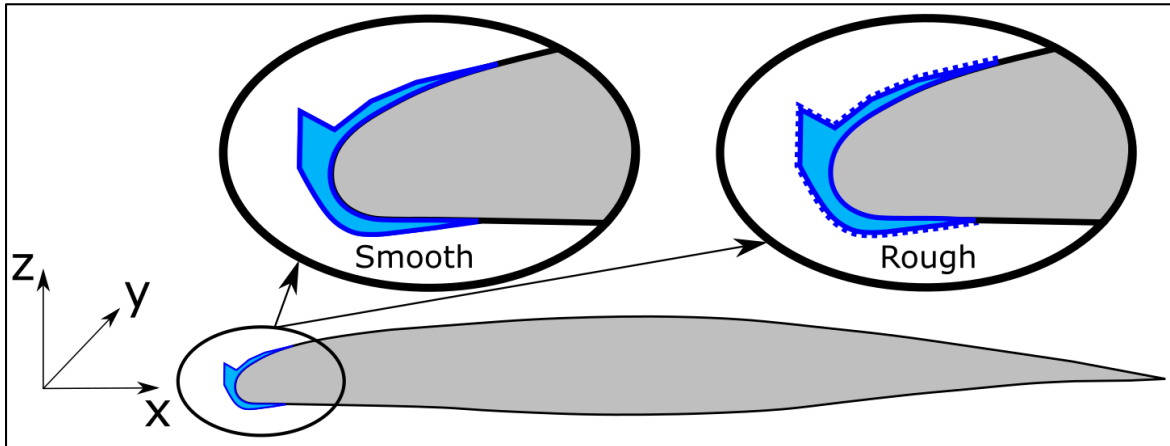
Figure 3-12 Outer wing section of a transport aircraft model 5-6 depicted in black (C case in the AG 32 report) with ice accretion highlighted in blue (C1 case in the AG32 Final report (GARTEUR, 2003)).
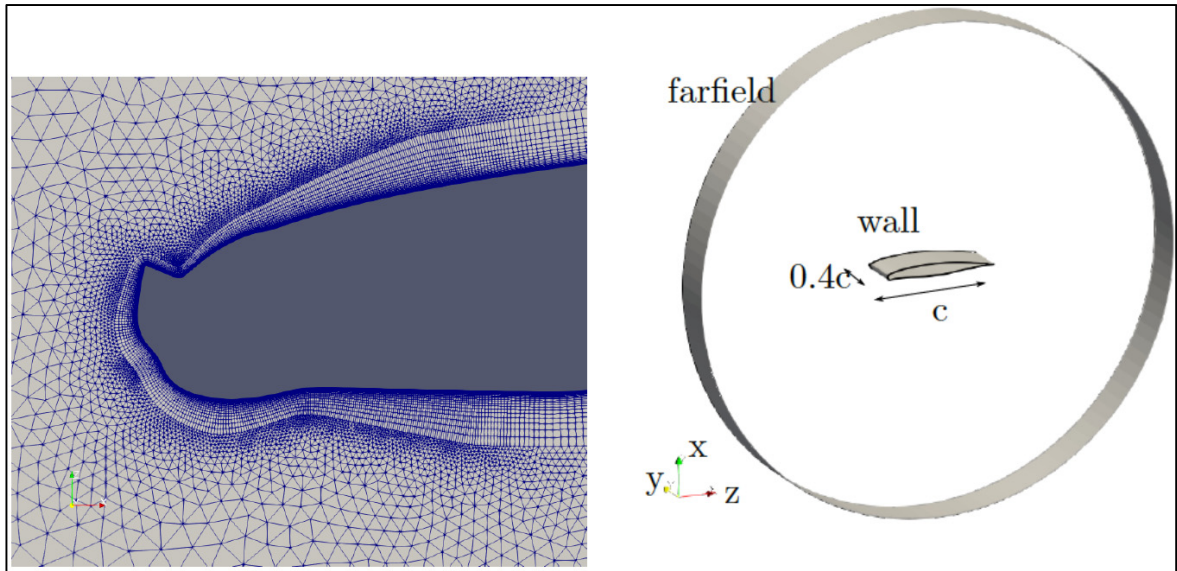
Figure 3-13 Mesh around iced model 5-6 airfoil and farfiel BC illustration

The numerical results taken from GARTEUR's final report are computed by the DLR-TAU code. The computations were obtained using RANS with the SA turbulence model fully turbulent. The main characteristics of the DLR-TAU computations performed within this project is a finite volume scheme with temporal gradients discretized using a multistep Runge-Kutta scheme, a calculation of the inviscid fluxes performed using an AUSM or a Roe type 2nd-order upwind scheme, and gradients of the flow variables determined by employing a Green- Gauss formula (Dezitter et al., 2009; GARTEUR, 2003).

In our study, two different simulations are performed; one with roughness deactivated (*SU2-RANS$_{smooth}$*), and the other with roughness activated (*SU2-RANS$_{rough}$*), in which an equivalent sand-grain roughness height of 0.6 mm is considered in the SA turbulence model (2.2.3). Figure 3-15 and Figure 3-15 present the velocity streamlines of the flow over smooth and rough iced model 5-6 airfoils at an angle of attack of 8 degrees. The velocity streamlines are colored by the streamwise velocity (velocity in x). The color legend is the same in both airfoils, with a maximum streamwise velocity of 102.5 m/s and maximum reverse velocity of 47.5 m/s. As shown, no significant difference is visually noticed between the estimations. A maximum streamwise velocity of 112.5 m/s is reached in both cases, and a reverse flow of -47.5 m/s is

seen in the separation region. The similarity in results might be caused either by the inefficiency of RANS to capture physics of massive-detached flows or by stronger effects of the horn ice as compared to roughness. Further investigations will be performed using *SU2-DDES* in section 4.1.2. As shown, trailing-edge flow separation occurs on the iced model 5-6 airfoil, which, differently of the NACA0012 study case, is mainly attributed to the horn ice effects in this case.
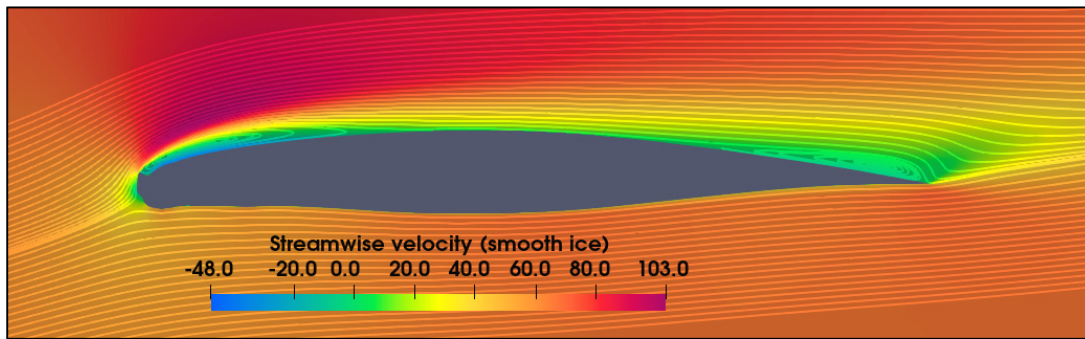
Figure 3-14 *SU2-RANS*$_{smooth}$ estimations of the streamwise velocity represented by streamlines of the flow over the smooth-iced airfoil at AoA=8 degrees

Figure 3-15 *SU2-RANS*$_{rough}$ estimations of the streamwise velocity represented by streamlines of the flow over the smooth-iced airfoil at AoA=8 degrees

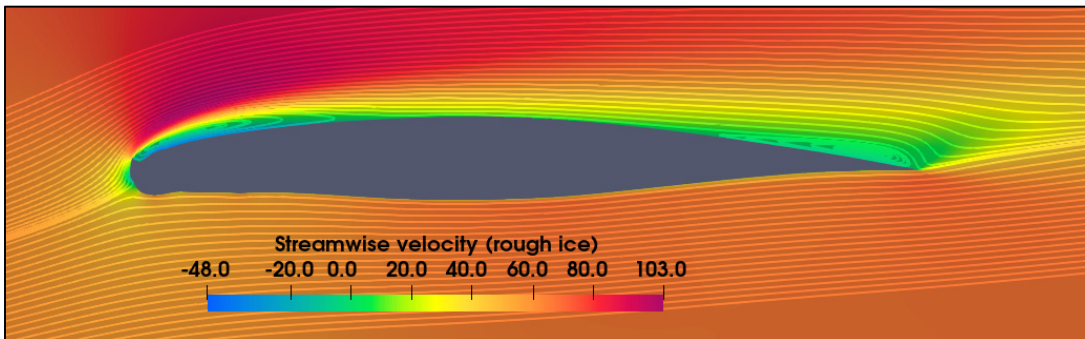Figure 3-16 presents lift, drag and moment curves. As shown in the first graph, the $C_{l\max}$ is under predicted by *SU2-RANS* and DLR-TAU in comparison to the measurements. DLR-TAU code presents a $C_{l\max}$ 17% inferior as compared to experiments, whereas *SU2-RANS* estimation

presents and error of 8%. At an AoA of 8 degrees, DLR-TAU achieves an error of 18.7% in comparison to measurements, whereas *SU2-RANS* reaches 6.82%.

For C_d, at AoA lower than or equal to 0°, DLR-TAU and *SU2-RANSsmooth* underestimate values up to 60%. This error is reduced to 6.7% with *SU2-RANSrough*. With increasing AoA (greater than zero, up to 7.5 degrees), *SU2-RANS* presents better results than DLR-TAU. At 5 degrees, DLR-TAU achieves an error of 14%; *SU2-RANSsmooth* reaches 8.3%; and *SU2-RANSrough* reduces the error to 0.2%, as compared to experiments. However, for the last two AoA assessed (8 and 9 degrees), DLR-TAU estimations are slightly better than *SU2-RANS*'s. At 8 degrees, DLR-TAU estimation achieves an error of 4.1%, while *SU2-RANSsmooth* achieves 7.6%. When roughness is activated, this value drops to 4.9%.

The recirculation region created behind the ice horn alters the flowfield structure causing a drop in the suction peak, pressure rises at the rear part of the airfoil, and accordingly, a more nose-heavy pitching moment is generated. The pitching moment curve shows a great discrepancy between measurement and calculations at a negative AoA of 6°, as seen in Figure 3-16. DLR-TAU and *SU2-RANSsmooth* present an error of around 82%, while *SU2-RANSrough* reduces this error to 35%. At the next two AoA, the estimations agree well with measurements. However, as the AoA increases, the gradient of the calculated pitching curve becomes higher than the measured one. Like the experiments, all calculations estimate a maximum pitching moment at an AoA of 7 degrees. At 8 degrees, DLR-TAU and *SU2-RANS* estimations agree presenting an error of around 23% as compared to experiments.
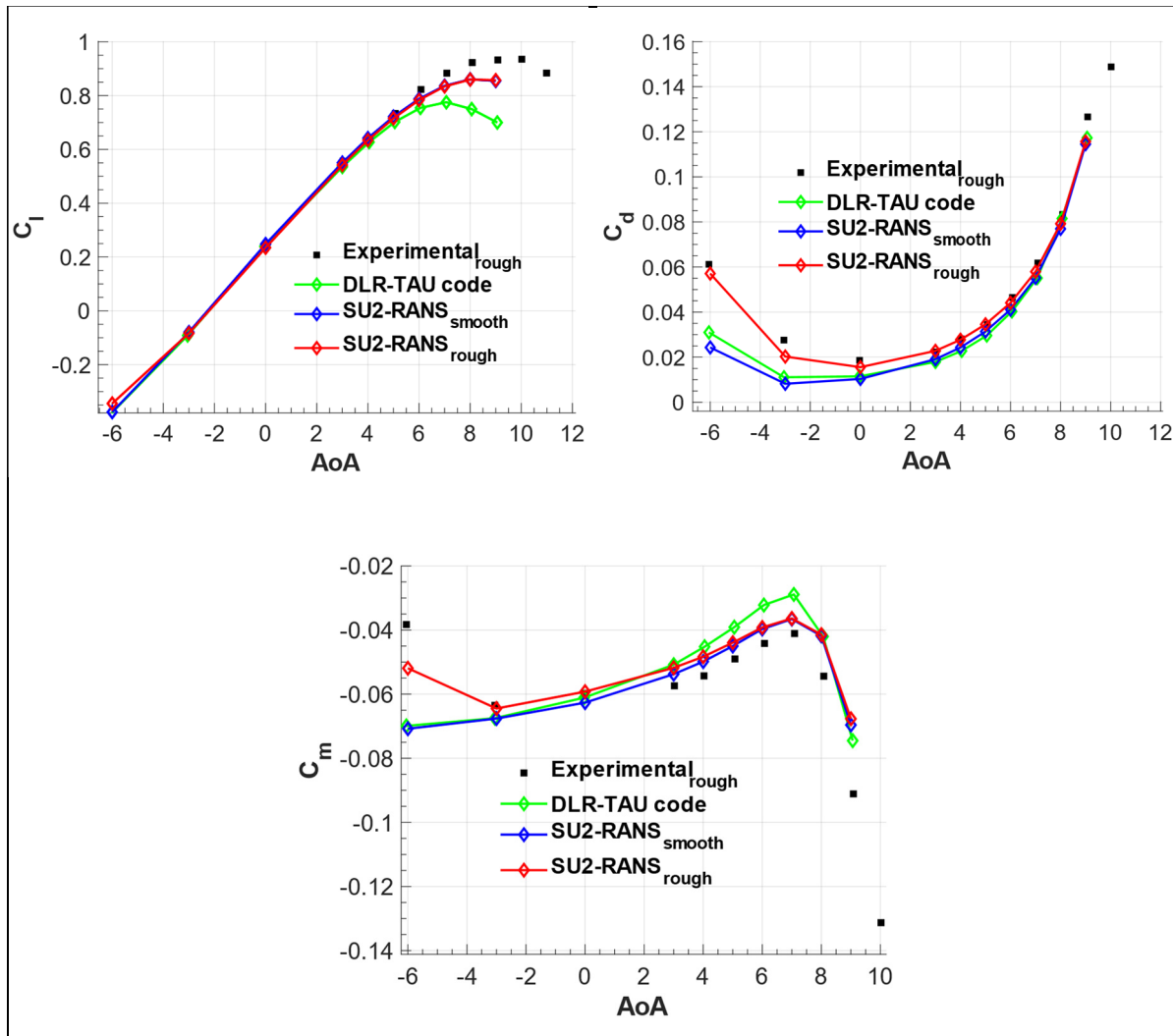
Figure 3-16 Drag, lift and Moment curves. Comparisons between SU2 results, DLR-TAU, elsA and experiments

3.1.4 Reynolds number and k_s sensitivity study

Wind-tunnel tests to evaluate ice formation are usually performed using scaled-down airfoils, which poses a concern on whether the results produced would apply to full scale flight conditions. Another concern is the computational cost of CFD simulations, which is increased at higher Reynolds numbers due to wider range of eddy sizes to be solved as well as finer grids requirements (Patel, 1998). Therefore, lower Re simulations are desired for industrial

applications. In this way, a Reynolds number sensitivity analysis would be helpful to shed light on these concerns.

Moreover, the process of in-flight ice formation might result in different roughness heights. As seen in the literature, the maximum lift coefficient, $C_{l(\max)}$, is usually reduced as the roughness height and density are increased (Brumby, 1979; Jackson, 1999). Thus, an evaluation of the effects of different roughness heights would help to quantify the aircraft performance degradation based on the deterioration of the $C_{l(\max)}$.

Therefore, this section has a two-fold objective. First, a study on the sensitivity of Reynolds numbers of flows over rough surfaces is performed. Second, the decrease of maximum lift coefficient of rough airfoils, $C_{l(\max)}$, caused by different equivalent roughness heights, k_s, is investigated. For the NACA 0012 airfoil, Reynolds number sensitivity analysis is performed keeping the equivalent sand-grain height fixed at $k_s / c = 6 \times 10^{-4}$, while for the model 5-6 this value is $k_s / c = 10 \times 10^{-4}$. Results for the NACA 0012 airfoil are first presented, followed by results for the 5-6 model.

3.1.4.1 NACA 0012

Figure 3-17 presents estimations of the lift coefficient, C_l, in function of the AoA for different Reynolds numbers using the NACA 0012 airfoil. The AoA is varied from 11 to 15 degrees, and the Reynolds number is varied from 1×10^6 to 18×10^6 with increments of 3×10^6. Table 2 gathers information obtained from Figure 3-17 as well as the $C_{l(\max)}$ reduction calculation for each Reynolds number selected. The reductions are calculated based on the first Re chosen, $\text{Re} = 1 \times 10^6$, herein called baseline Re. Hence, $\dfrac{(C_{l(\max)\_\text{Re}} - C_{l(\max)\_\text{Re}=1\times10^6})}{C_{l(\max)\_\text{Re}=1\times10^6}}$, where $C_{l(\max)\_\text{Re}}$ is the maximum lift coefficient estimated using a $k_s / c = 6 \times 10^{-4}$ at a selected Reynolds number,

and $C_{l(\text{max})\_\text{Re}=1\times10^6}$ is maximum lift coefficient with the baseline Re, $\text{Re}=1\times10^6$. As a matter of

space, $\dfrac{(C_{l(\text{max})\_\text{Re}} - C_{l(\text{max})\_\text{Re}=1\times10^6})}{C_{l(\text{max})\_\text{Re}=1\times10^6}}$ will be represented as $\Delta C_{l(\text{max})\text{Re}} / C_{l(\text{max})\_\text{Re}=1\times10^6}$ in the graphs.

As shown, $C_{l(\text{max})}$ suffers a decrease of 0.082 units (reduction of 6.7%) as the Reynolds number is increased from $\text{Re}=1\times10^6$ to $\text{Re}=3\times10^6$. In the next increments, the reduction achieves 9.5 % at $\text{Re}=6\times10^6$, then, 10% at $\text{Re}=9\times10^6$. From this point on, a plateau is achieved and no significant reduction in $C_{l(\text{max})}$ is achieved, as shown in Figure 3-18. This diminished evolution on the $C_{l(\text{max})}$ degradation as Reynolds is increased can also be seen in the experimental results of (Valarezo et al., 1993).
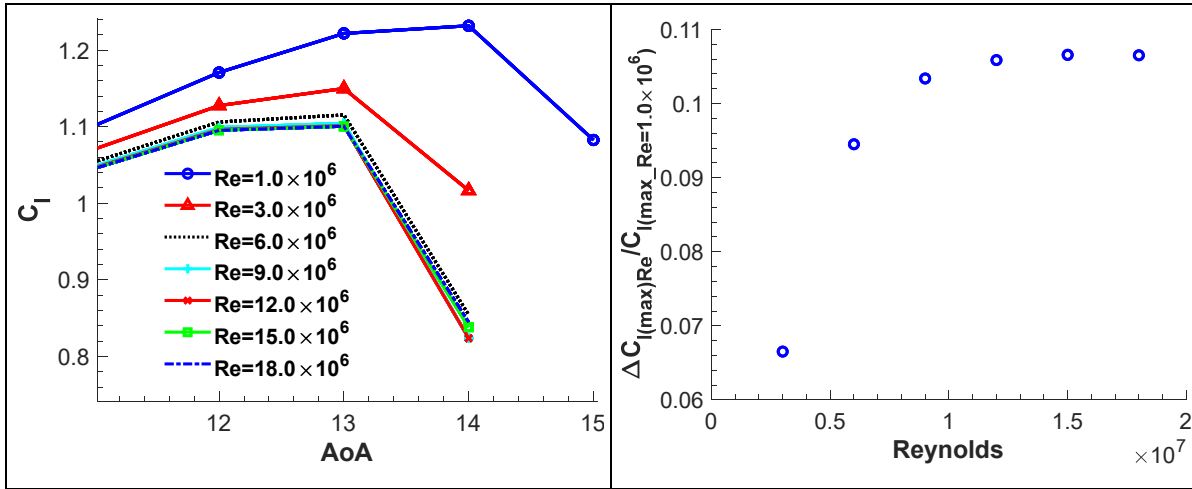

Figure 3-17 Influence of Re on C_l using the NACA 0012 airfoil

Figure 3-18 $C_{l(\text{max})}$ reduction due to variation in the Re using the NACA 0012 airfoil

Table 2 Maximum lift reduction caused by Reynolds number variation for the NACA 0012 airfoil

$C_{l(\max)}$	Re	$\dfrac{(C_{l(\max)\_Re} - C_{l(\max)\_Re=1\times10^6})}{C_{l(\max)\_Re=1\times10^6}}$	Reduction (%)
1.232	1.0E+06		
1.150	3.0E+06	-0.067	-6.7
1.115	6.0E+06	-0.095	-9.5
1.104	9.0E+06	-0.103	-10.3
1.101	1.2E+07	-0.106	-10.6
1.101	1.5E+07	-0.107	-10.7
1.101	1.8E+07	-0.107	-10.7

In order to analyze the decrease in $C_{l(\max)}$ caused by roughness, a range of equivalent sand-grain roughness heights, k_s, was evaluated and gathered in Figure 3-19, Figure 3-20 and Table 3. Hence, in Figure 3-19 the x-axis represents the variation of the angle of attack of the airfoil, while the y-axis represents the lift coefficient. Each curve is a representation of the behavior of C_l for a specific equivalent sand-grain roughness height. The reductions are calculated based on the maximum lift coefficient of the smooth airfoil. Hence, $\dfrac{(C_{l(\max)\_smooth} - C_{l(\max)})}{C_{l(\max)\_smooth}}$,

which will be represented as $\Delta C_{l(\max)k_s} / C_{l(\max)\_smooth}$ in the graphs.

As shown, for the first equivalent sand-grain roughness heights chosen, $k_s / c = 1\times10^{-7}$, $k_s / c = 1\times10^{-6}$ and $k_s / c = 1\times10^{-5}$, no significant decrease of $C_{l(\max)}$ is noted, as compared to the smooth case. The roughness Reynolds number for these k_s are within the aerodynamically smooth regime, $\mathrm{Re}_k < 5$. On the other hand, among the points chosen for the simulations over the NACA 0012, the effects produced by roughness become significant from $k_s / c = 1\times10^{-4}$, which marks the beginning of the in the transitional roughness Re regime ($5.0 < \mathrm{Re}_k < 70.0$), in which, according to Kays and Crawford (1993), the effects of roughness become to be noticeable on the flow. Thus, from $k_s / c = 1\times10^{-4}$, $C_{l(\max)}$ decreases rapidly, as illustrated in Figure 3-19 and Figure 3-20. However, as $k_s / c = 9\times10^{-4}$ is achieved, the changes in the

reduction of $C_{l(\max)}$ begins to decrease, as illustrated by the gentler slope of the curve shown in Figure 3-20. Therefore, even for the increased k_s used ($k_s / c = 16 \times 10^{-4}$, $k_s / c = 20 \times 10^{-4}$ and $k_s / c = 25 \times 10^{-4}$), the changes in reduction were mild.

It is also worth discussing at which AoA the maximum lift coefficient occurs. As presented in Table 3, the AoA of the $C_{l(\max)}$ is the same as that of the smooth case for $k_s / c = 1 \times 10^{-7}$, $k_s / c = 1 \times 10^{-6}$ and $k_s / c = 1 \times 10^{-5}$. Then, from $k_s / c = 1 \times 10^{-4}$ even mild increments suffice to drop the AoA of the $C_{l(\max)}$. Hence, at $k_s / c = 1 \times 10^{-4}$, the AoA of the $C_{l(\max)}$ is 16 degrees; at $k_s / c = 3 \times 10^{-4}$, the AoA drops to 14 degrees; and at $k_s / c = 7 \times 10^{-4}$ it becomes 12 degrees. When further increased, the maximum reduction on the AoA achieved is 11 degrees.
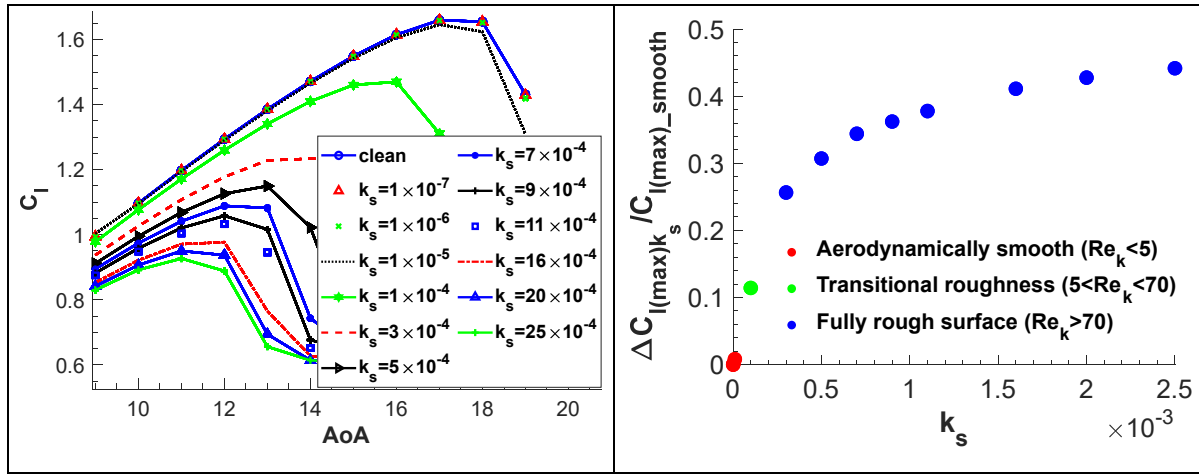

Figure 3-19 Influence of k_s on C_l using the NACA 0012 airfoil

Figure 3-20 $C_{l(\max)}$ reduction due to variation in the k_s using the NACA 0012 airfoil

Table 3 Maximum lift reduction caused by the equivalent sand-grain roughness heights variation for the NACA 0012 airfoil

	$C_{l(max)}$	AoA	k_s	$\dfrac{(C_{l(max)\_smooth} - C_{l(max)})}{C_{l(max)\_smooth}}$	Reduction (%)
smooth	1.66	17			
rough	1.66	17	1.0E-07	0.000	0.0
	1.66	17	1.0E-06	0.001	0.1
	1.65	17	1.0E-05	0.008	0.8
	1.47	16	1.0E-04	0.114	11.4
	1.23	14	3.0E-04	0.256	25.6
	1.15	13	5.0E-04	0.307	30.7
	1.09	12	7.0E-04	0.344	34.4
	1.06	12	9.0E-04	0.362	36.2
	1.03	12	1.1E-03	0.378	37.8
	0.98	12	1.6E-03	0.411	41.1
	0.95	11	2.0E-03	0.428	42.8
	0.93	11	2.5E-03	0.442	44.2

3.1.4.2 Model 5-6 airfoil

Similar to the previous study case, estimations of the lift coefficient, C_l, in function of the AoA for different Reynolds numbers are presented in Figure 3-21. The AoA of the model 5-6 is varied from 10 to 17 degrees, and the Reynolds number from 1×10^6 to 18×10^6 with increments of 3×10^6. Calculations were done as the ones in the previous study case, and results are presented in Table 4 and Figure 3-22.

As shown in Figure 3-21, a reduction in $C_{l(max)}$ of 5% is reached when the Reynolds number is increased from 1×10^6 to 3×10^6. Then, at 6×10^6, a reduction of 6.2% is obtained as compared to the baseline $Re = 1\times10^6$. The difference between the $Re = 3\times10^6$ and $Re = 6\times10^6$ is 1.2%, and from $Re = 6\times10^6$ to $Re = 18\times10^6$, no significant reduction is noticed, as shown in Table 4. The same behaviour is seen in the plateau region of Figure 3-22 .

Figure 3-21 Influence of Re on C_l using the model 5-6 airfoil

Figure 3-22 $C_{l(max)}$ reduction due to variation in the Re using the model 5-6 airfoil

Table 4 Maximum lift reduction caused by Reynolds number variation for the model 5-6 airfoil

$C_{l(max)}$	Re	$\dfrac{(C_{l(max)\_Re} - C_{l(max)\_Re=1\times10^6})}{C_{l(max)\_Re=1\times10^6}}$	Reduction (%)
1.463	1.0E+06		
1.390	3.0E+06	-0.050	-5.0
1.372	6.0E+06	-0.062	-6.2
1.367	9.0E+06	-0.065	-6.5
1.366	1.2E+07	-0.066	-6.6
1.366	1.5E+07	-0.066	-6.6
1.367	1.8E+07	-0.066	-6.6

The decrease caused by roughness on the maximum lift coefficient, $C_{l(max)}$, of the airfoil was studied over a range of different k_s. Results are compiled in Figure 3-23, Figure 3-24 and Table 5. In Figure 3-23, the x-axis represents the variation of the AoA of the airfoil, and the y-axis represents the lift coefficient for each AoA. Figure 3-24 illustrated the reduction of the maximum lift coefficient as well as the roughness Reynolds number for each k_s used. The same information is presented in more details in Table 5.

As shown in Figure 3-23 and Figure 3-24, the behavior of the rough 5-6 is very similar to that of the rough NACA 0012. Thus, $C_{l(\max)}$ suffers no significant influence for small k_s, and, for sufficiently large k_s, mild changes in the reduction of $C_{l(\max)}$ is noticed. On the other hand, for intermediate heights of k_s (from $k_s/c = 2\times10^{-4}$ to $k_s/c = 16\times10^{-4}$), the effect of roughness is elevated, and a significant loss in $C_{l(\max)}$ is seen. This behaviour is also illustrated in Figure 3-24, in which the steeper slope of the curve represents the highest influence of roughness.

As seen in Table 5, the AoA of the maximum lift coefficient for $k_s/c = 2\times10^{-6}$ and $k_s/c = 2\times10^{-5}$ is the same as that of the smooth airfoil, 17 degrees. Then, for $k_s/c = 2\times10^{-4}$, $k_s/c = 6\times10^{-4}$ and $k_s/c = 8\times10^{-4}$, a unitary reduction is achieved in each change, 16, 15 and 14 degrees, respectively. From this point on, mild variations in the AoA are seen, and the smallest value reached is 12 degrees for $k_s/c = 40\times10^{-4}$.
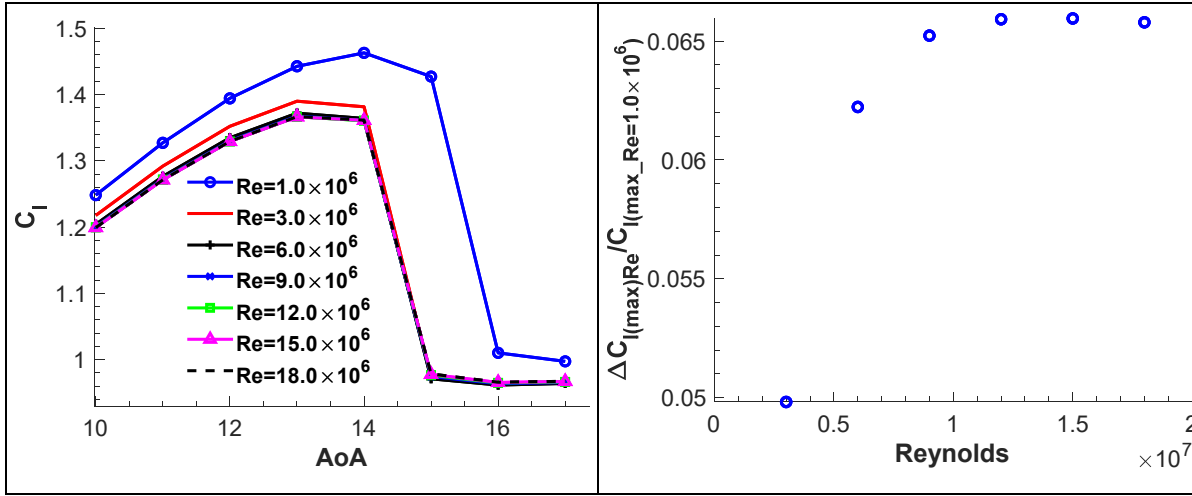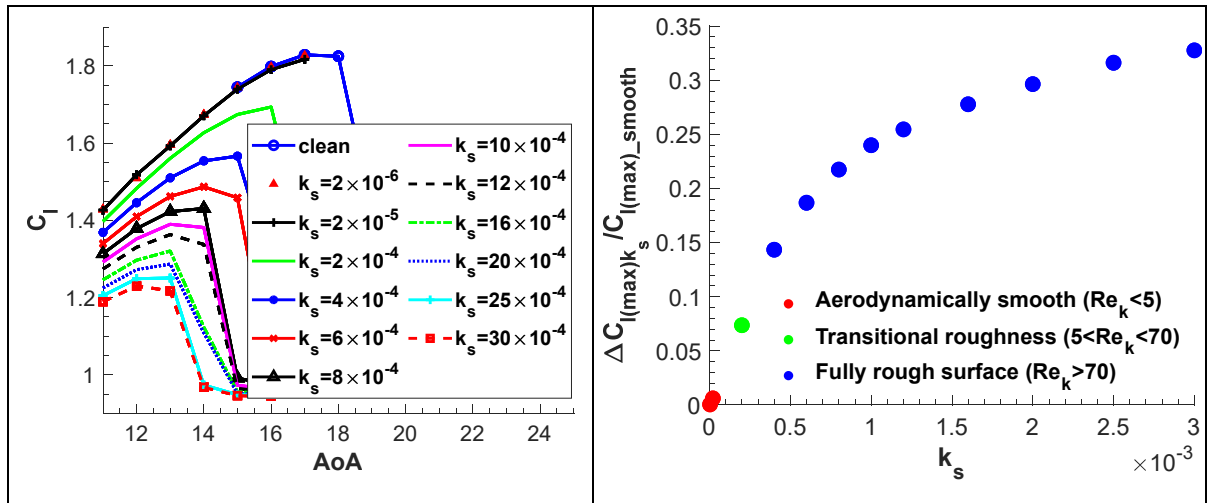

Figure 3-23 Influence of k_s on C_l using the model 5-6 airfoil

Figure 3-24 $C_{l(\max)}$ reduction due to variation in the k_s using the model 5-6 airfoil

Table 5 Maximum lift reduction caused by the equivalent sand-grain roughness heights variation for the model 5-6 airfoil

	$C_{l(\max)}$	AoA	k_s	$\dfrac{(C_{l(\max)\_smooth} - C_{l(\max)})}{C_{l(\max)\_smooth}}$	Reduction (%)
smooth	1.83	17			
rough	1.83	17	2.0E-06	0.001	0.1
	1.82	17	2.0E-05	0.006	0.6
	1.69	16	2.0E-04	0.074	7.4
	1.57	15	4.0E-04	0.143	14.3
	1.49	14	6.0E-04	0.187	18.7
	1.43	14	8.0E-04	0.218	21.8
	1.39	13	1.0E-03	0.240	24.0
	1.36	13	1.2E-03	0.255	25.5
	1.32	13	1.6E-03	0.278	27.8
	1.29	13	2.0E-03	0.296	29.6
	1.25	13	2.5E-03	0.316	31.6
	1.23	12	3.0E-03	0.328	32.8
	1.20	12	4.0E-03	0.344	34.4

Results show that, for the two airfoils considered, moderate reduction of maximum lift coefficient is noticed at Reynolds numbers greater than 6×10^6. This value is in accordance with the observations of (Lynch & Khodadoust, 2001), in which it is shown that Re values much below $5\Box\, 6\times10^6$ are most likely not meaningful or useful for higher Re applications. Therefore, higher-Reynolds-number simulations could be performed at reduced Reynolds numbers ($\text{Re} \geq 6\times10^6$) when estimating lift coefficient curves.

As for the equivalent sand-grain roughness heights investigated, results suggest that variation of sufficiently small heights has no significant influence on the maximum lift coefficient degradation. Moreover, when roughness is continuously increased, a saturation point seems to be approached, in which the variation of the maximum lift coefficient degradation is reduced. On the other hand, in-between values of k_s produce the maximum variation of the $C_{l(\max)}$ during the increments.

3.2 Smooth DDES

The flow over a backward facing step was studied experimentally by (Driver & Seegmiller, 1985), and their results have become reference for turbulence models verification and validation. In the experiment, the reference Mach number was set to 0.128, a freestream velocity of 44.2 m/s, and the Reynolds number was set to 36000 based on the length of the step of $h=1.27$ cm. Some numerical results such as RANS (Jespersen et al., 2016), DES (Dietiker & Hoffmann, 2009), DDES (Molina et al., 2017), which were done based on Driver & Seegmiller's experiment, have also been chosen for this study. Figure 3-25 shows the geometry of the problem. The flow enters at the inlet face with total pressure and temperature set at ($P_{total}=1293.26\ Pa$) and ($T_{total}=299.31\ K$), respectively, and it exits from the outlet face with static pressure $P=1278.53\ Pa$. Low values of pressure were achieved so that the fixed parameters, $Re=36000$ and $Ma=0.128$ could be kept for $h=1$ m. On top and bottom, adiabatic viscous walls confine the flow, and periodic boundary conditions are imposed on spanwise plans. The length of 130h is used upstream of the step, and a boundary layer thickness of 1.5h is achieved at $x/h=-4$. At $x/h=0$, the flow detaches from the wall, and a recirculation region is formed. A shear layer exists between the recirculation region and the main flow. Contrary to the original experiment (Driver & Seegmiller, 1985), in which an Aspect Ration (AR) of 12 is used, a study is performed in our work to assess the spanwise length effect on results. Thus, three AR (z/h) are evaluated, 2, 4 and 6. Symmetric boundary conditions are used for the spanwise plans in this evaluation.
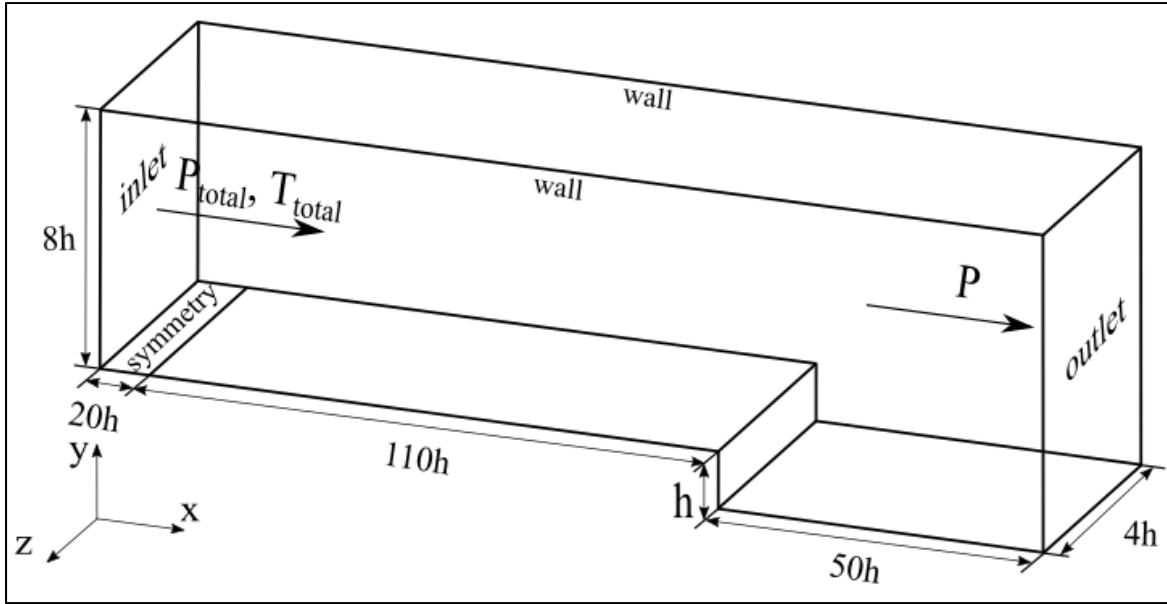
Figure 3-25 Backward facing step geometry (out of scale to show the main dimensions)

3.2.1   Spanwise length effect on results

DDES is a three-dimensional computational methodology, in which a minimum length in the spanwise direction is required to capture the biggest 3D structure in the flow (Lorenzo et al., 2011). According to Pan and Loth (2005), in order to capture the separation characteristics, this length should be related to the physical separation bubble size. The authors proposed a relation for an iced airfoil in which the spanwise length was twice the height of the separation bubble. In our study, the step size is one, therefore, we assume that the height of the separation bubble is also around 1, which would result in a minimum spanwise length of $z/h=2$. Thus, we started the investigation using the spanwise length of $z/h=2$. Then, we increased it to $z/h=4$, and, finally to $z/h=6$.

The computation grid used is based on one of the 2D grid available on NASA's turbulence modeling resource webpage (Rumsey et al., 2018). The original mesh, a four-zone mesh of 20,540 nodes, was extruded 20, 40, and 60 nodes in the z direction for $z/h=2$, $z/h=4$, and

$z/h=6$, respectively, which resulted in 3D cases with 410,800, 821,600, and 1,238,117 points with a fixed spanwise mesh spacing of $\Delta z/h=0.1$. For the calculation, a second order dual time stepping approach is used, with 10 inner iterations. The same time step, $\Delta t = 0.0204h/v_\infty$ with $v_\infty = Ma\sqrt{\gamma RT} = 44.3\text{m/s}$, was used for the three meshes. Simulations are run for 1958 CTU (Convective Time Unit), with $CTU = h/v_\infty$, and the time-averaging is performed using the last 938 CTU.

According to Holmén (2012), research in the area of vortex identification has been of interest since the discovery of vortical structures in turbulence. Among the available methods, a commonly used approach based on the second invariant of the velocity gradient tensor is the Q-criterion, which is used in all DDES results of this thesis. This method identifies as vortices those regions where vorticity magnitude is larger than the strain-rate magnitude with the following expression:

$$Q = \frac{1}{2}\left(\|\mathbf{\Omega}\|^2 - \|\mathbf{S}\|^2\right)$$
(2.56)

where $\mathbf{\Omega}$ is the antisymmetric part known as the vorticity tensor, and $\mathbf{S}$ is symmetric part known as the rate of strain. Values of $Q>0$ represent the existence of a vortex.

Figure 3-26 presents the instantaneous iso-surfaces of Q-criterion ($Q=500$ s^{-2}) colored by the velocity for channels with span width of $z/h=2$, $z/h=4$ and $z/h=6$. Once the step is reached, the flow is seen to begin rolling up forming two-dimensional structures, which are broken down by Kelvin-Helmholtz instabilities into random three-dimensional structures. No significant change is seeing among the structures of the different channels.
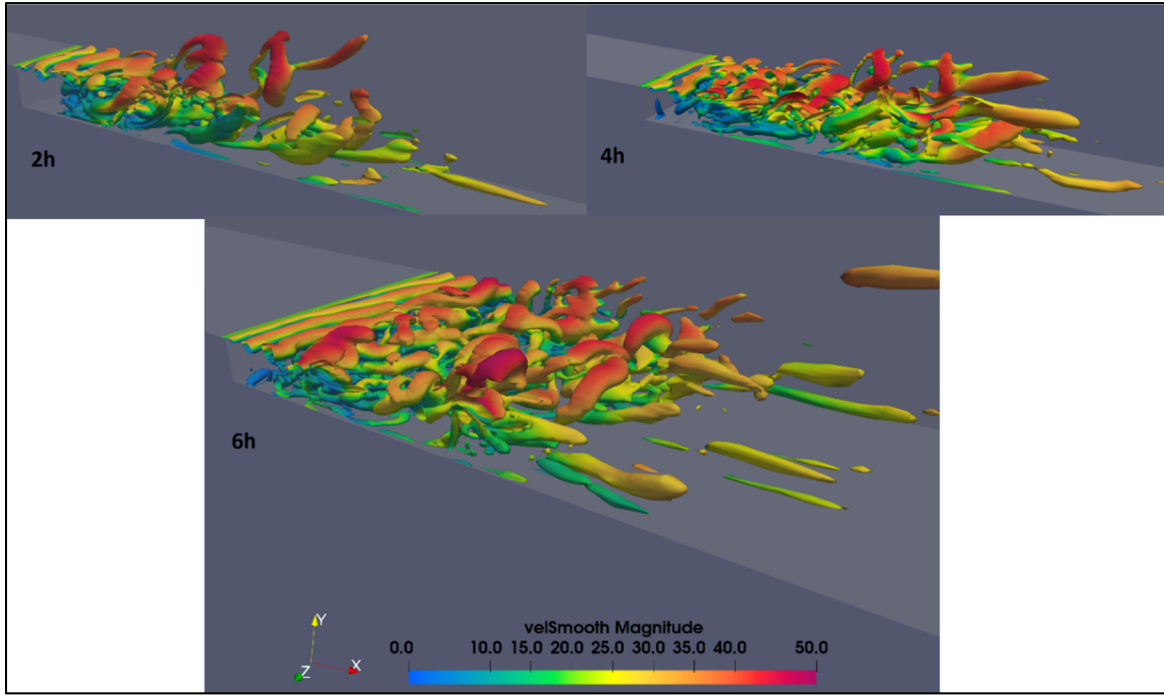
Figure 3-26 Instantaneous iso-surfaces of Q-criterion ($Q = 500\,\text{s}^{-2}$) colored by the velocity for channels with span width of $z/h=2$, $z/h=4$ and $z/h=6$

Figure 3-27 and Figure 3-28 present the mean wall pressure coefficient and friction coefficient distribution along the lower wall of the channels with span width of $z/h=2$, $z/h=4$ and $z/h=6$. Temporal statistics are calculated using the last 938 CTU, and space averaging is performed using all points along the spanwise direction. For the evaluation of the discrepancies among the different channels, the channel with the widest span width ($z/h=6$) is taken as reference. Thus, the difference among estimations of C_p is $C_{p\_(reference)} - C_{p\_(compared)}$, where $C_{p\_(reference)}$ is the C_p of the channel with width $z/h=6$, and $C_{p\_(compared)}$ is either the C_p of the channel with span width of $z/h=2$ or $z/h=4$. Then, the general equation (2.53) for percent discrepancy is used, in which $\Delta C_p = 0.190$, is calculated from the difference between $C_{p(max)}$ and $C_{p(min)}$, at $x/h=7.83$ and $x/h=2.33$, respectively. The same approach is used to evaluate discrepancies of friction coefficient distribution C_f, in which $\Delta C_f = 0.00466$, $C_{f(max)} = 0.00340$ and $C_{f(min)} = -0.00126$.

As shown in Figure 3-27, the difference in the span width caused mild effects on pressure coefficient; some discrepancies near the maximum and minimum values are visible. In the recirculation region of the channel with span of $z/h = 2$, the maximum discrepancy in C_p is 6% at $x/h = 1.5$, and for the channel with span of $z/h = 4$, this value drops to 2.3% at $x/h = 3.7$, as compared to the widest channel ($z/h = 6$). Near the reattachment point, at $x/h = 6$, discrepancies are 3.8% and 0.5% for spans of $z/h = 2$ and $z/h = 4$, respectively. From this point on discrepancies present inferior values. For the friction coefficient, the maximum discrepancies in the recirculation region are 5.8% at $x/h = 2.2$ and 4.2% at $x/h = 3.2$, for spans of $z/h = 2$ and $z/h = 4$, respectively. At $x/h = 6.5$, discrepancies reach 3.8% for the span of $z/h = 2$, whereas this value drops to 0.8% for the wider span ($z/h = 4$). After $x/h \square 15$, a plateau is reached, and discrepancies fluctuate between 1.3% and 2.4% for both widths, as shown in Figure 3-28. The estimation of reattachment point reaches a 2.2% discrepancy for $z/h = 4$, when compared to $z/h = 6$; for $z/h = 2$, the difference is 3%.

As already mentioned, the span width of the domain should be two times the height of the separation bubble (Pan & Loth, 2005; Zhang et al., 2015). In our case, the step height is 1, which requires a spanwise size of $z/h = 2$. However, as shown in Figure 3-27 and Figure 3-28, the discrepancies obtained with a span of $z/h = 4$ are in general lower as compared to the narrower channel. Therefore, in order to reduce the overall discrepancies while keeping acceptable computational cost, the grid with an aspect ratio of 4 was chosen for our simulations.
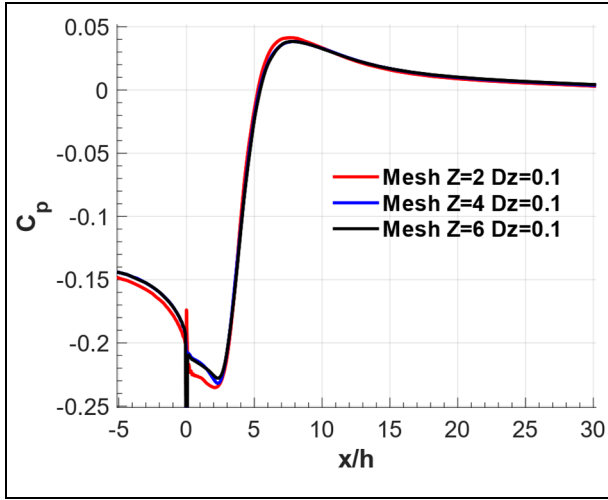
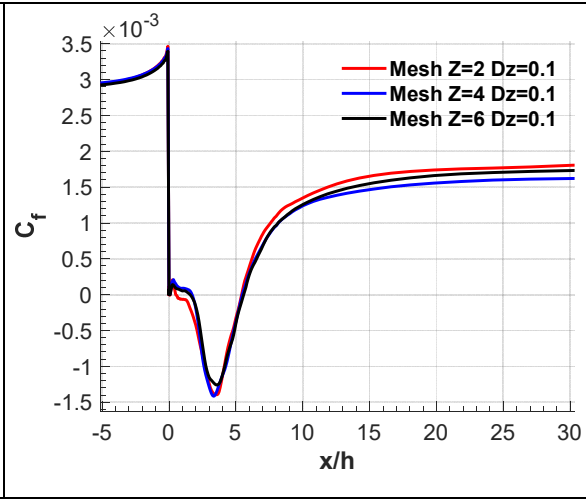Figure 3-27 Effect of spanwise length on the pressure coefficient

Figure 3-28 Effect of spanwise length on the friction coefficient

3.2.2 Smooth surface backward facing step (validation)

Figure 3-29 and Figure 3-30 present the time-averaged streamwise nondimensional velocity (v/v_∞), taken in the middle of the channel ($z/h = 2$), on different stations. In Figure 3-29, our estimations are compared to Molina's numerical results (Molina et al., 2017). As it can be seen, curves tend to slightly deviate as they get farther from the bottom wall. The maximum difference is seen on station $x/h = -4$, in which our nondimensional velocity is 8.5% higher than Molina's. In Figure 3-30, a comparison is made with numerical (DES model) and experimental data obtained from Dietiker (Dietiker & Hoffmann, 2009). When comparing *SU2_DDES*_{smooth} estimations of v/v_∞ to experiments, the largest difference is found on station 4 at $y/h = 0.193$, in which our nondimensional velocity is 25.6% higher than experiments. Numerical results of Dietiker achieved a maximum difference of 49.7% on station 6 at $y/h = 0.188$.
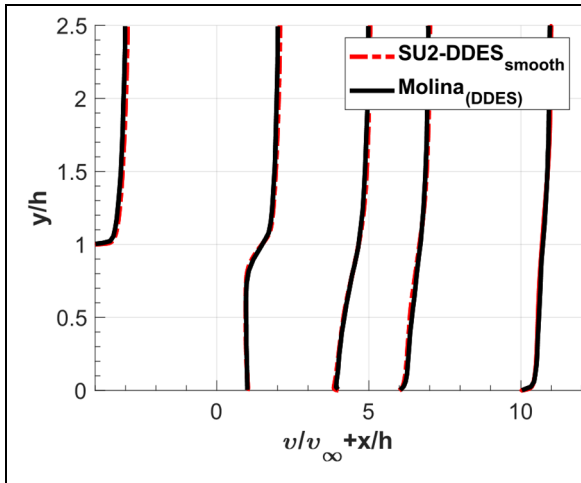
Figure 3-29 Mean nondimensional streamwise velocity profiles compared to numerical results
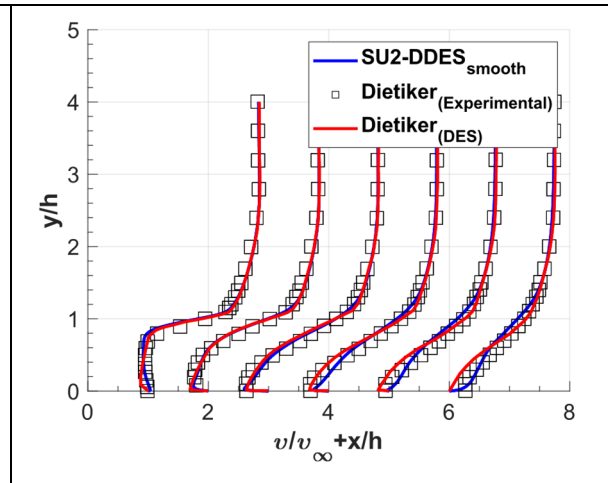
Figure 3-30 Mean nondimensional streamwise velocity profiles compared to numerical and experimental results

The mean wall pressure coefficient and friction coefficient distribution along the lower wall are presented in Figure 3-31 and Figure 3-32, respectively. Comparisons are made using RANS (Jespersen et al., 2016), DES (Dietiker & Hoffmann, 2009), DDES (Molina et al., 2017) as well as experimental results (Driver & Seegmiller, 1985). RANS results were obtained using CFL3D code with Spalart-Allmaras turbulence model; DES estimations were made using Cobalt code with Menter's shear stress transport turbulence model; and DDES results were obtained using the standard SU2 (version 5.0) with the SA turbulence model. As recommended on NASA Langley Research Center Turbulence Modeling Resource website (Rumsey et al., 2018), C_p and C_f were calculated based on references values such as velocity, density and pressure near the position $x / h = -4$. Moreover, the pressure coefficient data was uniformly shift so that C_p is zero near $x / h = 40$. For the errors and discrepancies, the general equation 2.53 is used with $\Delta C_p = 0.2297$ and $\Delta C_f = 0.0014$, obtained from maximum and minimum values of the experimental results.

For the mean wall pressure coefficient, all models underestimated C_p before the step. As shown in Figure 3-31, at $x / h = -2.5$, CFL3D estimation presented the maximum error, which is 10.8% inferior as compared to experimental results, whereas *SU2-DDESsmooth* estimations

achieved the most reduced error of 8.2%. The lowest C_p of the flow was estimated, by all codes, in the detached-flow region, from $x/h = 0$ to $x/h = 6.26$, where the latter is the reattachment point obtained from (Rumsey et al., 2018). Among the codes estimations for that region, *SU2-DDES$_{smooth}$*'s results presented the minimum error of 18.1%, against 24.8% and 25.1% from Dietiker's and CFL3D's estimations, respectively.

For the friction coefficient distribution before the step, all codes but Dietiker's presented very similar estimations. The difference in his results may be caused by the choice of a shorter extension of the channel before the step. In the recirculation region, the estimation of the minimum C_f, by CFL3D, is 16% inferior to experimental results. This error was expected due to the inefficiency of RANS for detached flows. As the other codes use unsteady models, the error was reduced to values between 9.5% and 10.6%. Although Molina's DDES estimations were also obtained using SU2, our samples utilized for statistics seem to be larger, which resulted in somewhat different curves. Moreover, (Molina et al., 2017) chose symmetric boundary conditions for their simulations, while we used periodic boundary conditions.
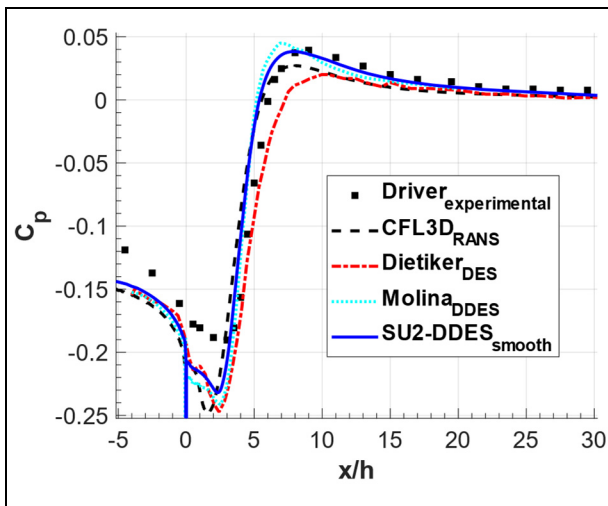

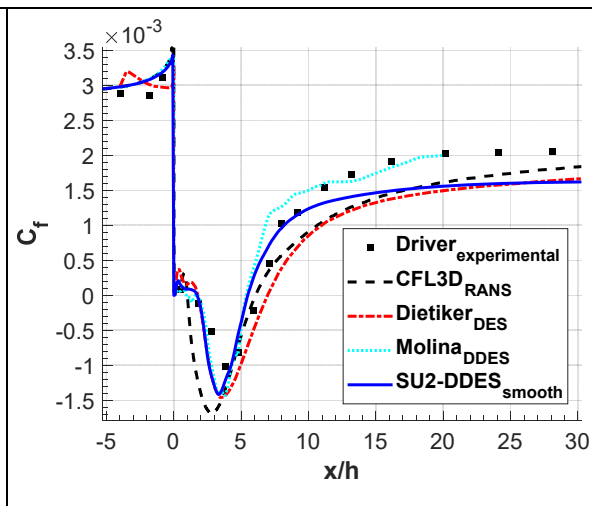Figure 3-31 Mean pressure coefficient along the lower wall

Figure 3-32 Mean skin friction coefficient along the lower wall

3.2.3   Smooth-surface NACA0012 (validation)

The flow around a NACA 0012 airfoil at high Reynolds number has been extensively studied both experimentally (Critzos et al., 1955; Hoerner, 1965; Sheldahl & Klimas, 1981) and numerically, using RANS, URANS, LES, DES and DDES models. For the NACA 0012 airfoil with an AoA of 45 degrees, some results, especially average lift and drag coefficients, are available in the literature at $Re = 1.3 \times 10^6$ for URANS, DES, and DDES (Im & Zha, 2014a), and at $Re = 1 \times 10^5$ for experimental, DES and URANS (Shur et al., 1999). According to (Im & Zha, 2014a; Shur et al., 1999), Reynolds number dependence is weak in post-stall conditions for high Reynolds numbers ($Re > 10^5$). Thus, the Reynolds number chosen for this paper is $Re = 1.3 \times 10^6$, $Ma = 0.15$, and the freestream temperature is 300 K.

In this study, the 2D computational domain used in (Tagawa et al., 2018) was extruded along the span to a distance of 1.0c, as shown on Figure 3-33. The mesh has 429 elements in the streamwise direction (x axis), 129 elements in the direction normal to the airfoil (y axis), and 100 elements in the span wise direction (z axis). The mesh spacing in z is 0.01c, similar to the typical magnitude of the values found in the literature, for instance the 0.03c value of (Im & Zha, 2014b). The heat flux is set to zero at the wall. The farfield boundary condition is located 500c away from the airfoil in order to minimize the issues associated with the boundaries. Periodic boundary conditions are defined in the spanwise direction, and adiabatic solid wall on the airfoil.
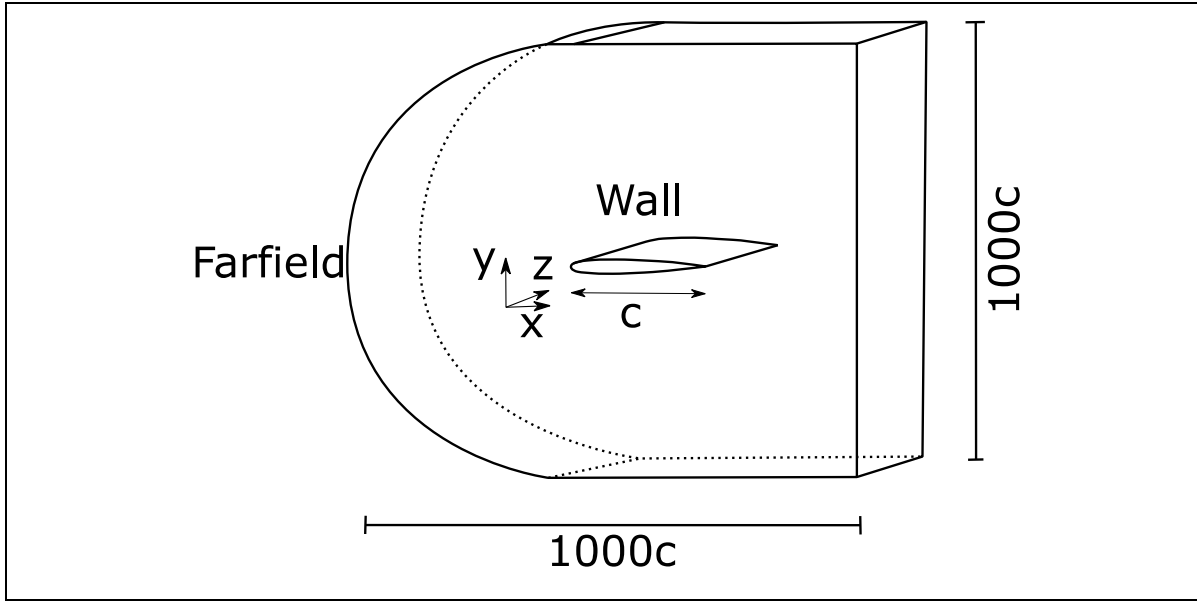
Figure 3-33 Three-dimensional computation domain around the NACA 0012 airfoil

The aerodynamic parameters, C_l, C_d and C_p, are obtained using *SU2-DDESsmooth* simulations for a stalled AoA of 45 degrees. At such AoA, the flow detaches from the airfoil resulting in a zone of high turbulence and recirculation, which cannot be well predicted using RANS models due to the unsteady nature of the flow.

The time step estimation for DES-type simulations is known to be challenging. We followed the recommendation of (Spalart & Allmaras, 1994) of keeping a unitary CFL in the Focus Region (FR), which is the region close to the body where the turbulence must be well resolved (Philippe, 2001). The CFL number is calculated based on the local flow velocity, the local mesh spacing, and the time step size. The maximum velocity in the FR is 30% higher than the freestream velocity, and it was obtained from previous RANS simulations results. For the local mesh spacing, the distance between nodes considered is $\Delta x = 0.01c$. Therefore, a physical time step of $\Delta t = 0.15$ milliseconds (non-dimensional time $\Delta t^* = \Delta t \dfrac{v_\infty}{c} = 0.0078$) is obtained. Between each physical time step (outer iteration), 20 pseudo time steps (inner iterations) were used, which caused a reduction of the residuals of around 2.5 orders of magnitude.

Figure 3-34 represents a zoomed-in view of residuals reduction (y-axis) for five outer iterations (x-axis), from 6725 to 6730. Between each outer iteration, 20 inner iterations are performed. As shown, on the first curve of the left side, at an inner iteration of 17, the maximum reduction was achieved. On the other hand, the last curve on the right required the 20 inner iterations to achieve the maximum reduction of residuals.
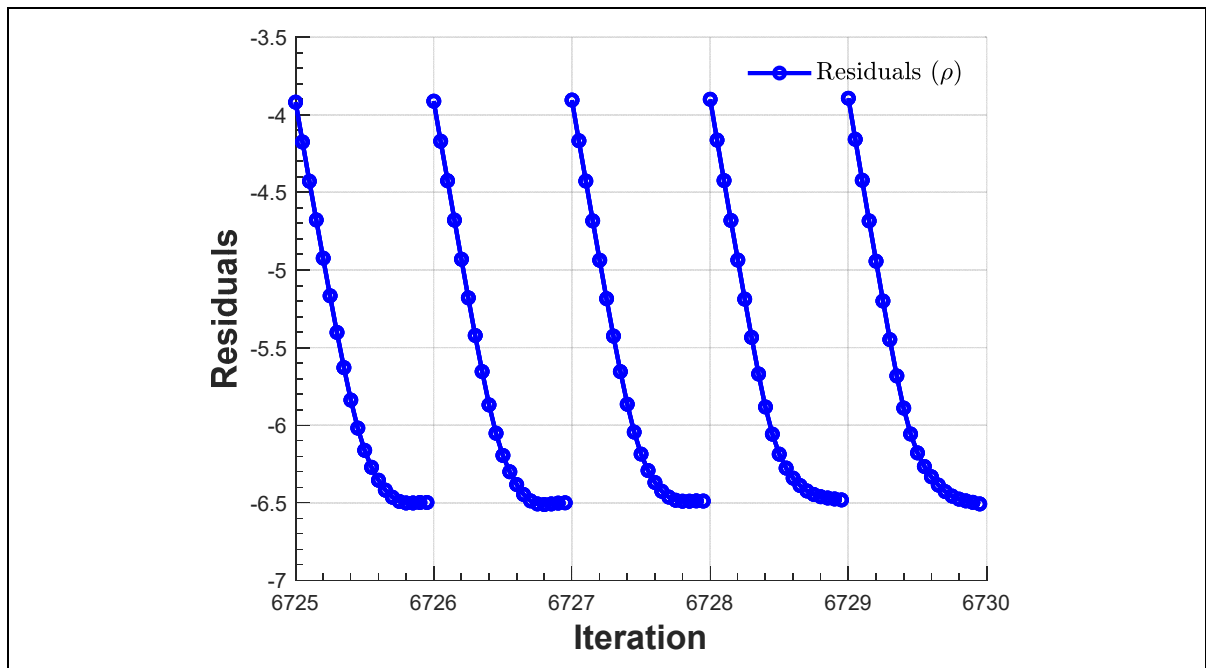
Figure 3-34 Residuals between physical time steps (20 pseudo time steps)

Figure 3-35 presents the isosurfaces of the Q-criterion, $Q=15000\,\text{s}^{-2}$, colored by the velocity magnitude at 68.7 CTU. As can be seen, the flow separation occurs at the leading edge, and a chaotic turbulent region is formed along the whole upper surface of the airfoil. In this region, the flow recirculates, and the velocity is drastically reduced, which cooperates for a high increase in the drag force. It can also be noted that close to the airfoil there are smaller turbulent eddies, whereas a bit farther, larger eddies are formed.
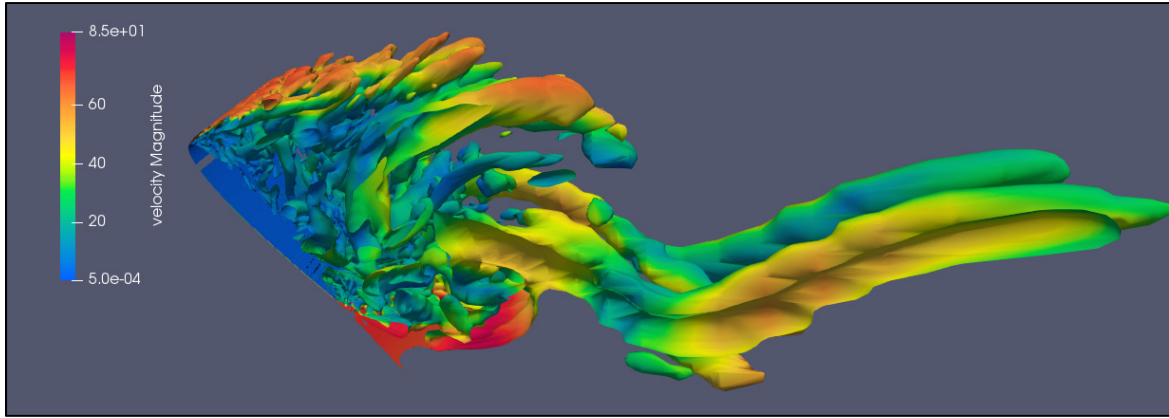
Figure 3-35 Isosurfaces (Q=15000 s^{-2}) of the Q-criterion colored by the velocity at iteration number 8790

Figure 3-36 presents the mean pressure coefficient around the airfoil. The time-averaging process was performed from 46.9 CTU to 125 CTU. Results are compared to numerical and experimental results taken from (Shur et al., 1999). When comparing *SU2-DDES*smooth results to experimental results, the estimation of the pressure coefficient presents an error of 4.5% at $x/c = 0.1$ (leading edge region). A larger error, 12.3%, is obtained for the trailing edge at $x/c = 0.9$, as shown in Table 6. The pressure predicted by *SU2-DDES*smooth is flat on the top of the airfoil like Shur's experimental results, but lower. However, as the experimental results are between the two numerical predictions, the discrepancies are similar.
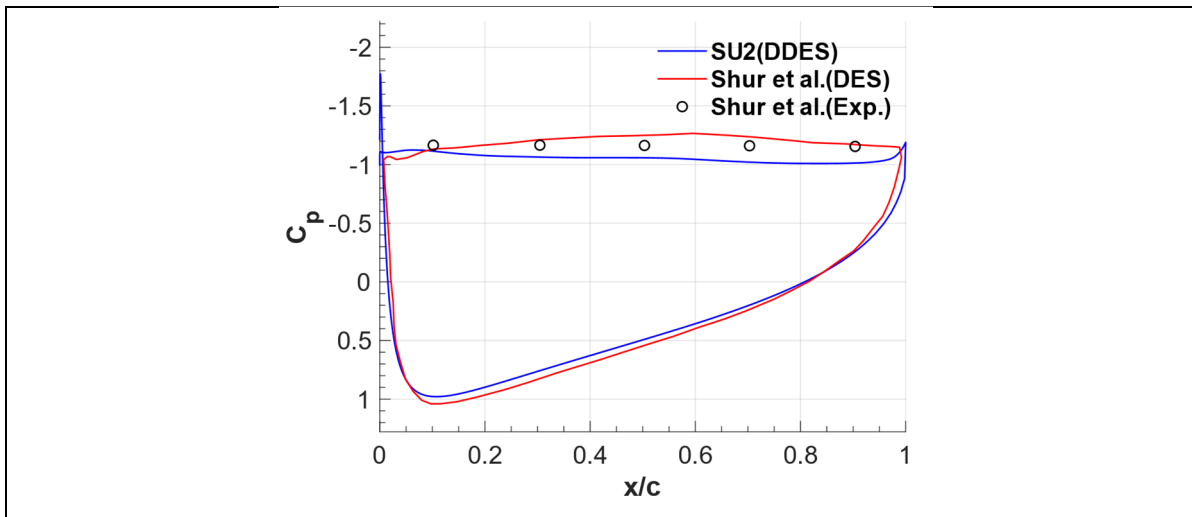
Figure 3-36 Mean pressure coefficient

Table 6 Pressure coefficient error when compared to experimental results

x/c	0.106	0.306	0.492	0.699	0.900
C_p error (%)	-4.12	-8.67	-9.02	-11.9	-12.3

SU2-DDES$_{smooth}$'s estimations of instantaneous and mean lift coefficients are presented in Figure 3-37. Similarly, instantaneous and mean drag coefficients are shown in Figure 3-38. In both figures, the mean values are represented by the green lines, while the standard deviations are presented in pink. Statistics were obtained using the last 1.5 seconds (78 CTU). Estimations are gathered in Table 7 along with results taken from (Im & Zha, 2014a). The maximum discrepancy encountered when comparing with DDES numerical results is 2% for C_l, and 0.05% for C_d. When comparing with the experimental results, an error of 8.9% is found for C_l, and 2.9% for C_d.
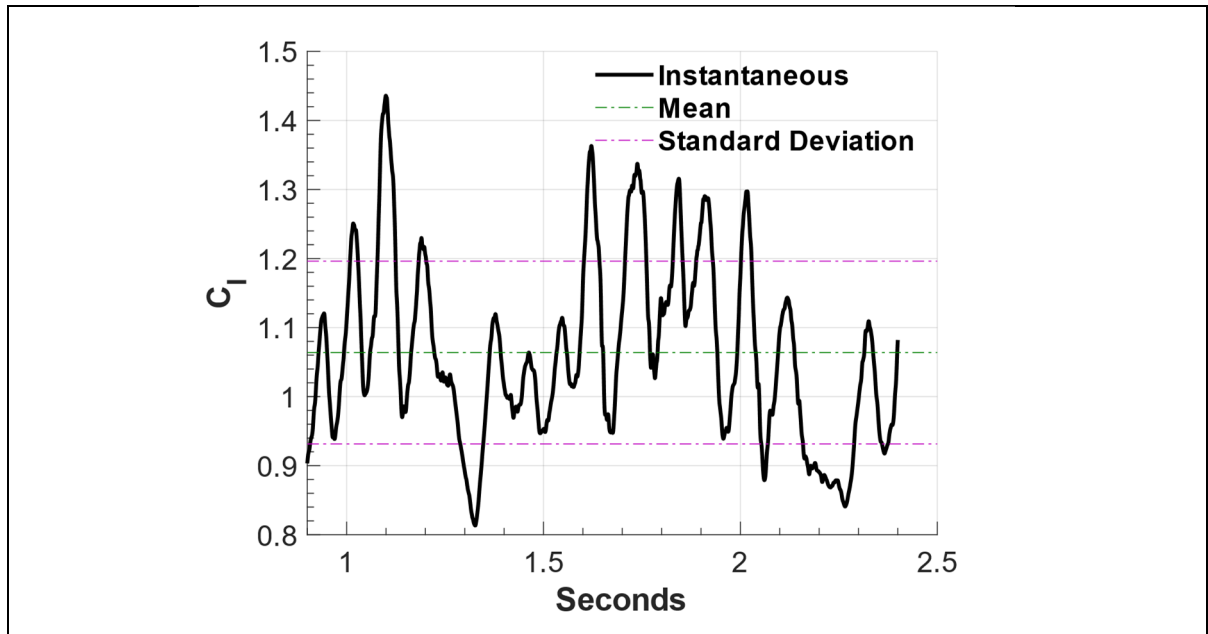
Figure 3-37 C_l Instantaneous and Mean values over a NACA 0012 in deep stall
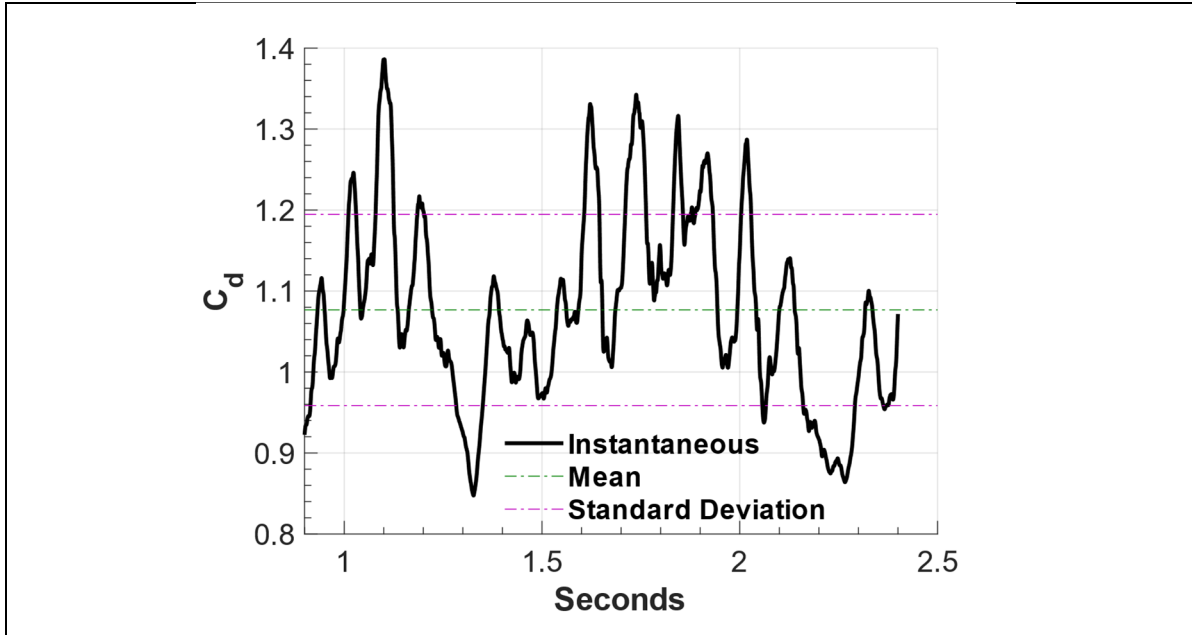
Figure 3-38 C_d Instantaneous and Mean values over a NACA 0012 in deep stall

Table 7 Lift and drag coefficients of NACA 0012 airfoil in deep stall

| | Reference | | | SU2 | |
	Experiment	URANS	DES	DDES	DDES	Standard deviation
C_d	1.11	1.42	1.07	1.08	1.08	0.12
C_l	1.17	1.43	1.09	1.09	1.06	0.13
Error % (C_d)	28.10	3.09	2.93	2.89		
Error % (C_l)	22.60	7.04	6.96	8.90		

3.3   Summary

The roughness implementation performed in SU2 code was verified and validated using RANS (smooth and rough surfaces) and DDES (smooth surfaces with massive flow separation) simulations in this chapter. For the RANS, we began our simulations with one of the simplest and most investigated study cases used in CFD simulations, a flat plate. In this way, friction coefficients along two flat plates, a smooth and rough one, were estimated using *SU2-RANSsmooth* and *SU2-RANSrough*. Next, flows over smooth and rough NACA 0012 airfoils were

evaluated using *SU2-RANS$_{smooth}$* and *SU2-RANS$_{rough}$.* Finally, an iced airfoil (model 5-6) was chosen so that the flow could be evaluated over smooth and rough ice using *SU2-RANS$_{smooth}$* and *SU2-RANS$_{rough}$*.

Errors of our estimations, as compared to experimental results, were assessed through confrontations with errors of numerical estimations found in the literature. *SU2-RANS* estimations of friction (flat plates) and lift (NACA 0012) coefficients were equivalent or superior to results obtained from the literature. The estimations of nondimensional velocities were improved in the first region the airfoil. However, the thickening of the boundary layer caused by roughness resulted in a slight underestimation of values after $x/c = 0.10$. For the iced model 5-6, *SU2-RANS* estimations of lift coefficient were superior to the numerical reference, and no significant difference was seeing between *SU2-RANS$_{smooth}$* and *SU2-RANS$_{rough}$* results. Despite the improved results of *SU2-RANS,* when larger regions of detached flow were reached after 6 degrees, *SU2-RANS* underestimated C_l, as compared to experiments. This behaviour was expected due to the inefficiency of RANS models to capture the physics of massive flow separation. When estimating C_d, although *SU2-RANS$_{smooth}$* estimations agreed with the numerical reference, a maximum error of 60% was achieved as compared to experimental results. However, the roughness implementation successfully reduced this error to 6.7%.

Two additional investigations were performed with the roughness implementation in RANS, a study on the Reynolds number sensitivity, and the influence of equivalent sand-grain roughness heights on the aircraft performance degradation based on the deterioration of the $C_{l(\max)}$. Results showed that, for Re greater than 3×10^6, a plateau was reached, and the reduction of maximum lift coefficient became stationary, which allow high-Re flows to be simulated at reduced Reynolds numbers. The equivalent k_s heights investigation, showed that sufficiently small heights have the same influence on $C_{l(\max)}$ as the smooth surface. Moreover, although great reductions of $C_{l(\max)}$ was seen for significant sizes of k_s, the continuous increase of k_s did not result in a linear performance degradation, and the $C_{l(\max)}$ becomes almost constant

when roughness is continuously increased, a saturation point seems to be approached, in which the variation of the maximum lift coefficient degradation is reduced. On the other hand, in-between values of k_s produce the maximum variation of the $C_{l(\max)}$ during the increments.

Once *SU2-RANS* estimations were verified and validated, we began the evaluations using the *SU2-DDES* model. As DDES is an unsteady model aimed at capturing the physics of massive-separated-flow turbulence, a minimum length in the spanwise direction was required to capture this three-dimensional phenomenon. Therefore, we performed a study using backward facing steps with three different aspect ratios, $z/h = 2$, $z/h = 4$ and $z/h = 6$, which directed us towards the width of $z/h = 4$. Following, evaluations were performed using two study cases with massive flow separation, a smooth surface channel with a backward facing step and a smooth NACA 0012 airfoil in deep stall. For the first, C_p, C_f and velocity profiles were estimated, while for the latter, C_p, C_l and C_d were obtained. For the BFS, *SU2-DDESsmooth* estimations of C_p and C_f presented reduced errors, especially in the recirculation region. Nondimensional velocity profiles were also well estimated. The maximum error found reached 25.6%, against 49.7% of the reference. Similarly, for the NACA 0012 in deep stall, *SU2-DDESsmooth* estimations presented small errors, as compared to experimental results.

In the next chapter, we present our study of massive-separated flows over rough surfaces using two study cases, a rough channel with a backward facing step, and a rough iced 5-6 model wing. The DDES model with roughness implemented is used for the simulations.

CHAPTER 4

RESULTS AND DISCUSSION

The DDES model with roughness implementation has been successfully verified and validated using smooth surfaces with massive flow separation. The objective of this chapter is to evaluate how roughness affects DDES estimations of aerodynamic parameters of massive-separated flows over rough surfaces. The evaluation is performed using two three-dimensional study cases, a rough backward facing step and a rough-iced model 5-6 airfoil.

4.1 Rough DDES

4.1.1 Rough backward facing step

In this study case, we use the same parameters utilized in the smooth surface backward facing step (3.2.2). The only additional parameter is the roughness on the bottom wall along the whole channel (Figure 4-1), which is imposed by an equivalent sand grain roughness of 50 mm. k_s is chosen so as to have the flow in the fully rough regime, $\mathrm{Re}_k \geq 70.0$. Thus, for $k_s = 50\,\mathrm{mm}$, a roughness Reynolds number of $\mathrm{Re}_k = 100$ is obtained just before the step at $x/h = -4$. Moreover, the boundary layer thickness at $x/h = -4$ is $2h$, against $1.5h$ in the smooth case at the same location.
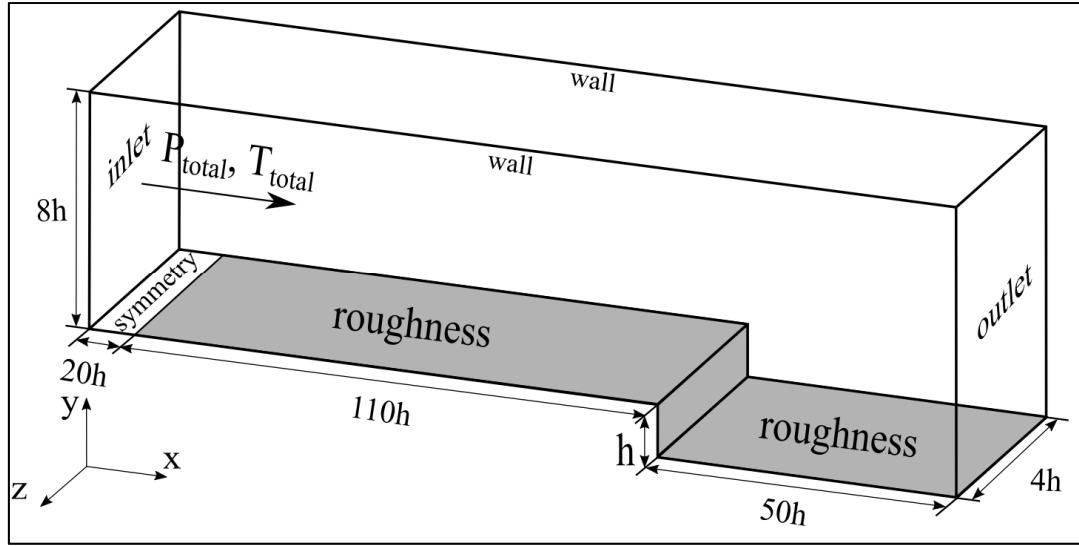
Figure 4-1 Backward facing step geometry, out of scale to show the main dimension

Flow separation and reattachment are common phenomena in engineering, which have been investigated, experimentally and numerically, for several years. The smooth-surface backward facing step study case has become well-known for the investigation of the effects of these phenomena, with many results published (Eaton & Johnston, 1981). Concerned about the role played by roughness on the effects already revealed, some authors began to investigate (Essel & Tachie, 2015; Kim & Chung, 1995; Wu et al., 2013). They discovered that, in general, roughness reduces the maximum reverse flow velocity in the recirculation region, which results in an increased reattachment length.

Figure 4-2 and Figure 4-3 present the instantaneous iso-surfaces of Q-criterion ($Q=25$ s^{-2}) colored by the streamwise velocity over the channel with smooth and rough surfaces, respectively. Although the three-dimensional structures are very similar in both cases, higher velocities can be seen represented by the increased reddish eddies of the flow over the smooth surface. Roughness effects thicken the boundary layer of the flow over the rough surface, which results in lower velocities at the same height (distance from the wall), as compared to the smooth surface. This difference in velocity can also be seen by the contour plot of the time-averaged nondimensional streamwise velocity, v/v_∞, presented in Figure 4-5 and Figure 4-6.
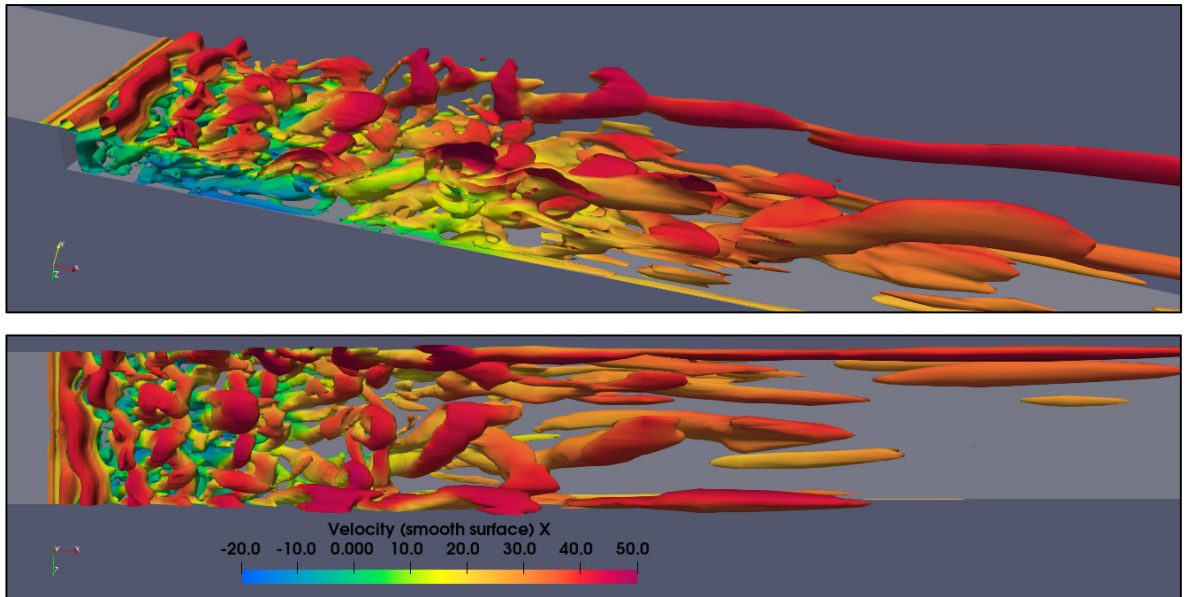
Figure 4-2 Instantaneous iso-surfaces of Q-criterion ($Q=25$ s^{-2}) colored by the streamwise velocity over a smooth surface

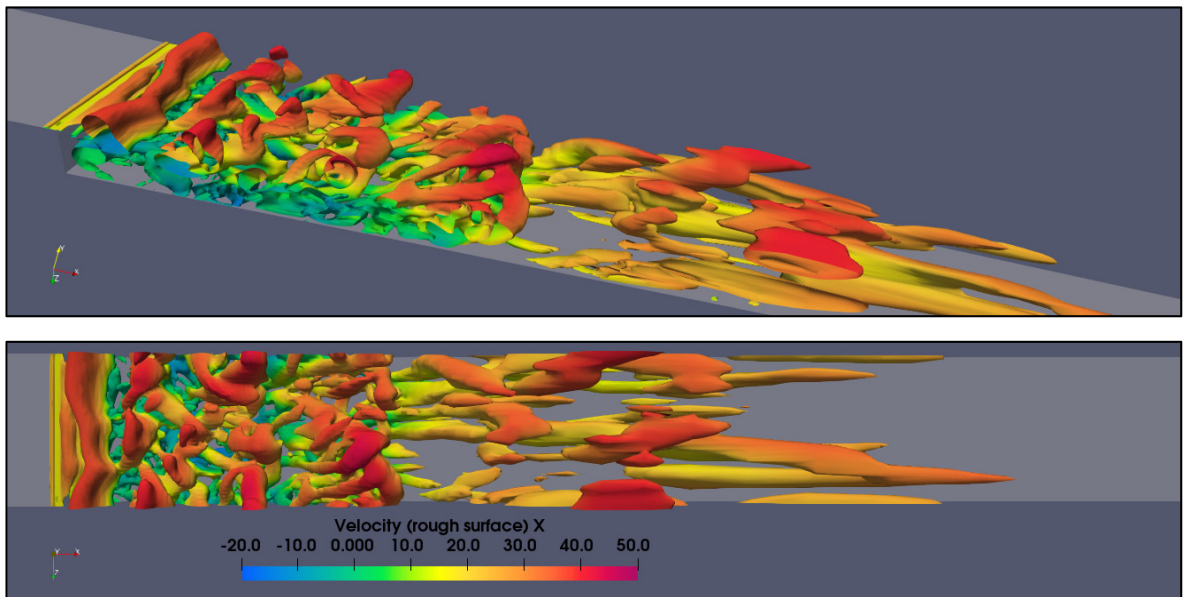
Figure 4-3 Instantaneous iso-surfaces of Q-criterion ($Q=25$ s^{-2}) colored by the streamwise velocity over a rough surface

Figure 4-4 illustrates the roughness Reynolds number ($\mathrm{Re}_k = \dfrac{\upsilon_\tau k_s}{\nu}$, where υ_τ is the friction velocity) along the bottom wall of the channel. *SU2-DDESrough* is used, and values are taken from the middle of the channel (plane xy at $z / h = 2$). In the region after the step, Re_k reaches zero at $x / h = 2.15$, and it begins to increase again at $x / h = 6.2$ (reattachment point), which continues exponentially up to $x / h = 11$, where a $\mathrm{Re}_k = 55.07$ is reached. From this point on, Re_k increases gently, achieving a value of 65.5 at $x / h = 50$.
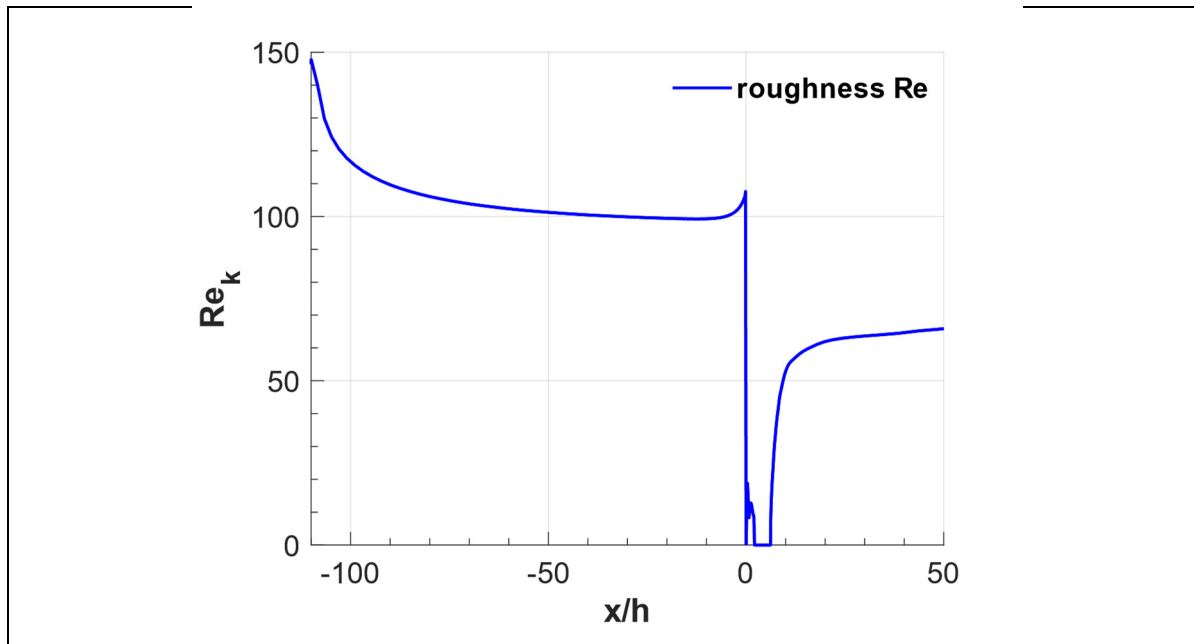
Figure 4-4 Roughness Reynolds number along bottom wall

Figure 4-5 and Figure 4-6 present the contour plot of the time-averaged (last 938 CTU) nondimensional streamwise velocity, $\upsilon / \upsilon_\infty$, of the flows over smooth and rough backward facing steps estimated with *SU2-DDES*. Curves were created with results taken from a cut of the middle of the channel (plane xy at $z / h = 2$). As done by (Wu et al., 2013) and (Essel & Tachie, 2015), the reattachment length was evaluated based on the contour line drawn from the step edge to the first grid point at the wall, where the averaged velocity is zero. Thus, Figure

4-5 and Figure 4-6 illustrate the reattachment lengths of the flows over smooth and rough backward facing steps, which occur at $x/h = 5.49$ and $x/h = 6.22$, respectively.

As seen in Figure 4-5 and Figure 4-6, the maximum reverse flow velocity reaches 20% of the free-stream velocity in both cases, against 19% and 18%, for smooth and rough in (Essel & Tachie, 2015); and 10% for both cases in (Wu et al., 2013). Note that the former author used an aspect ratio of 21, whereas the latter used 96. The resistance caused by roughness also results in the formation of the maximum reverse flow region farther downstream at $x/h = 3.28$, instead of $x/h = 2.30$ as occurs in the smooth case (distance measured from the step to the beginning of the contour lines of the maximum reverse flow). The same phenomenon can be seen in Figure 4-8 and Figure 4-9. Moreover, a secondary counterclockwise recirculation region is also seen in the corner of the step in both channels. In the smooth case, this region is formed between $x/h = 0$ and $x/h = 1.7$. Whereas, in the rough one, this region is slightly longer (between $x/h = 0$ and $x/h = 2.1$) and thicker.
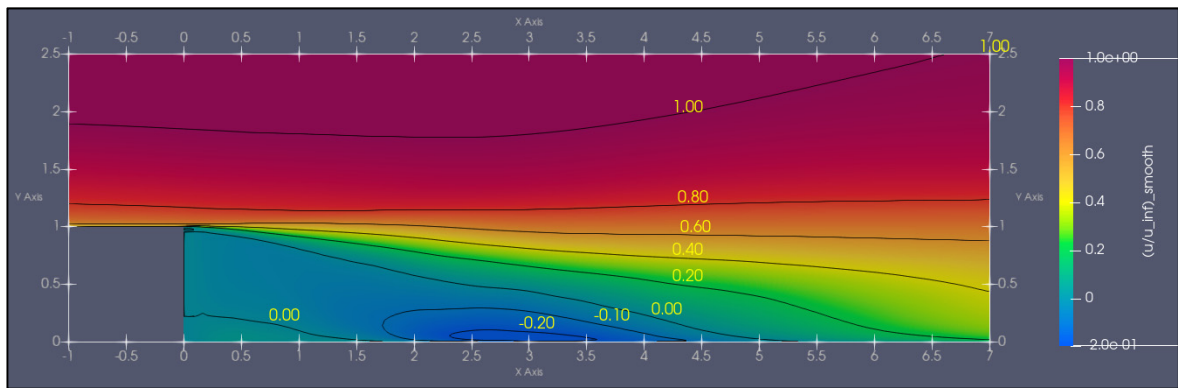

Figure 4-5 Contour plot of the time-averaged nondimensional streamwise velocity, υ/υ_∞ (Smooth BFS)
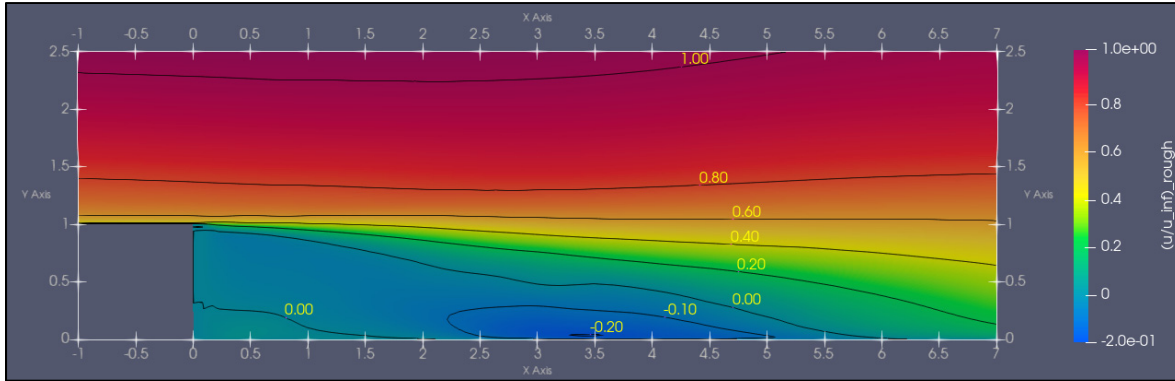
Figure 4-6 Contour plot of the time-averaged nondimensional streamwise velocity, v/v_∞ (Rough BFS)

With the purpose of evaluating whether taking values from a cut in the middle of the channel accurately reflects the characteristics of the flow, the reattachment points of all cuts along the spanwise direction are plotted in Figure 4-7. The red curve (left side) represents the smooth case, whereas the black one (right side) represents the rough case. As seen, the reattachment points are very similar along z in the smooth case. The space averaging of all points results in a reattachment point at $x/h = 5.48$, against $x/h = 5.49$ taken from the cut in the middle of the channel. In the rough case, points present a somewhat higher dispersion achieving a standard deviation of 0.0972, against 0.0365 in the smooth case. The space averaging of all points, in the rough case, results in $x/h = 6.13$, while the value taken from the middle of the channel is $x/h = 6.22$, which results in a discrepancy of 1.5%. The causes of this somewhat higher dispersion are not understood yet, and further investigations must be performed.

The aforementioned dispersion is also seen in Figure 4-8 and Figure 4-9, in which the streamwise skin friction coefficient is presented on the bottom wall of the channel. The black curves represent the regions where the C_f is null, which corresponds to the regions of zero nondimensional velocities presented in Figure 4-7, and consequently the reattachment point. The region of reverse flow, represented by the negative skin friction coefficient, is formed farther downstream, confirming what was shown in Figure 4-5 and Figure 4-6, which was represented by the nondimensional velocities. The values of positive friction coefficient represent the secondary counterclockwise recirculation regions.

As shown, the difference between results caused by the dispersion of points can be neglected in the smooth case. However, as this difference is slightly higher in the rough case, the space-averaged values will be used in our study. (Essel & Tachie, 2015) found experimental values of $x/h = 6.1$ and $x/h = 6.2$ using sandpaper SP-24 and SP-36, respectively. Note that geometric parameters such as expansion rate and aspect ratio used by (Essel & Tachie, 2015) are different than ours.
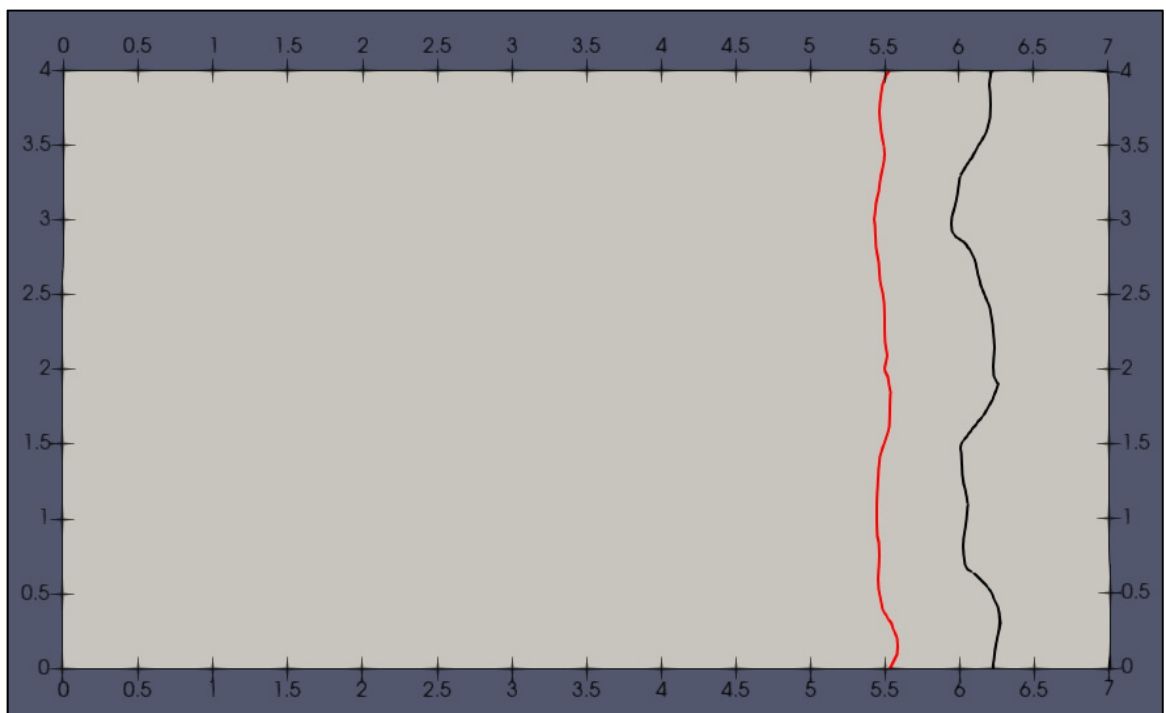

Figure 4-7 Reattachment point of all planes in the spanwise direction for smooth (left) and rough (right) cases
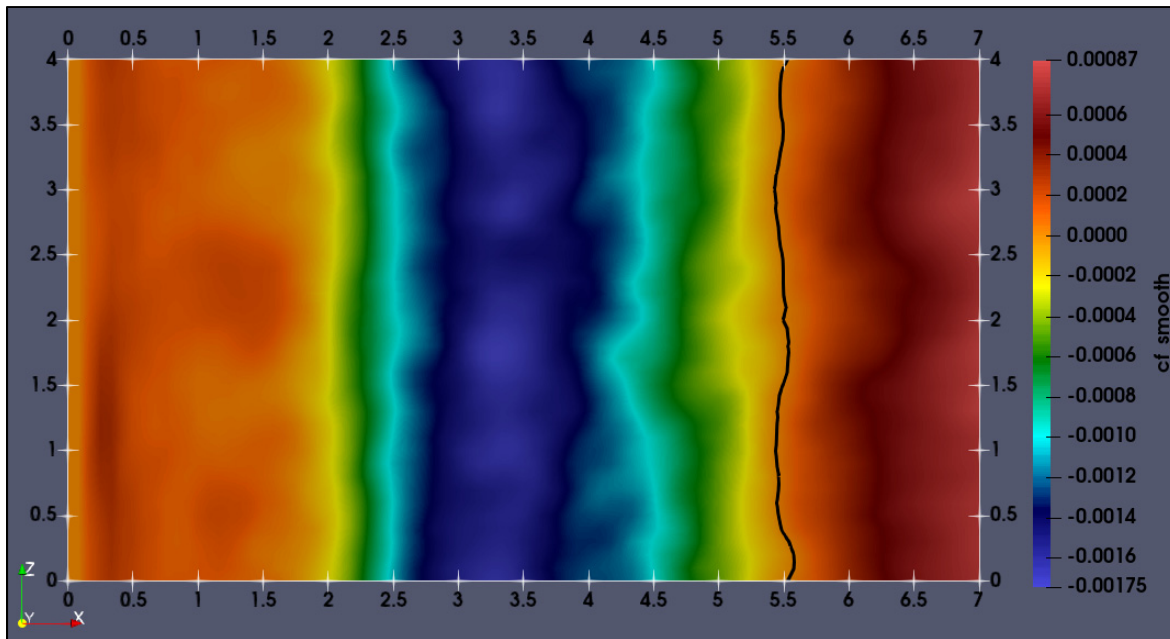
Figure 4-8 Skin friction coefficient over the bottom smooth surface
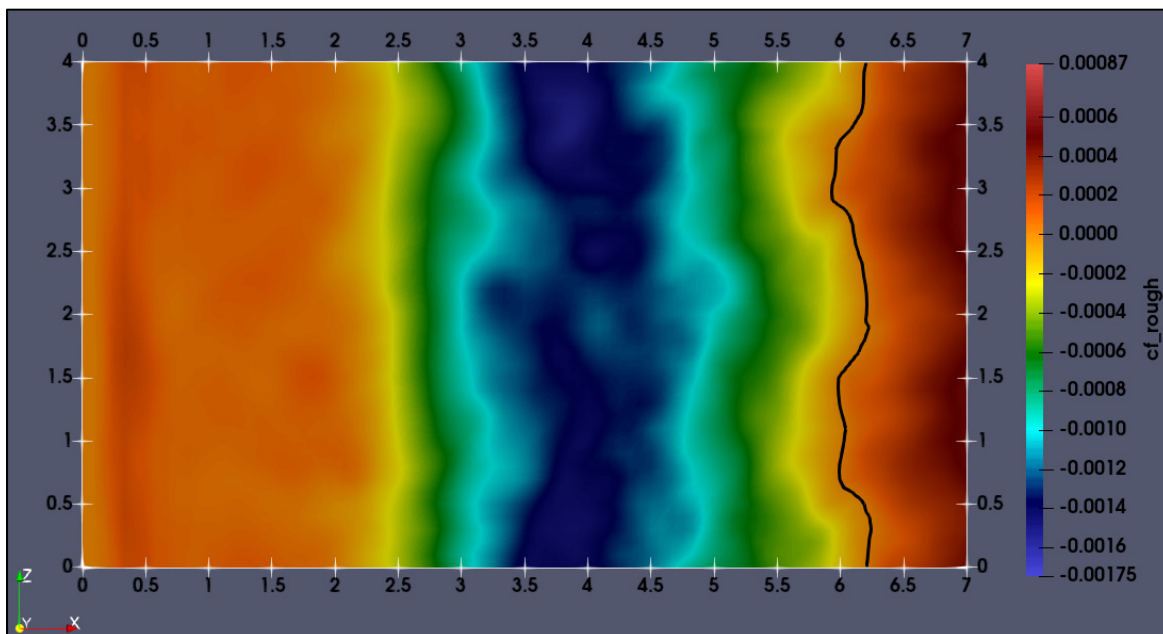

Figure 4-9 Skin friction coefficient over the bottom rough surface

Figure 4-10 presents the estimation of mean streamwise velocity profiles over smooth and rough surfaces. As shown, the rough velocity profiles are most often behind (lower velocity) the smooth ones due to roughness effects. Different phenomena occur in the recirculation region. At $x/h = 1$, the bottom wall roughness effects seem weaker than the adverse pressure gradient caused by the sudden expansion. Therefore, curves match from the bottom wall up to $y/h = 0.65$. At $x/h = 2$, roughness influence increases, and the backflow closer to the wall (from $y/h = 0$ to $y/h = 0.45$) is smaller than that of the smooth surface. The greatest difference is reached very close to the wall at $y/h = 0.085$, in which the nondimensional velocity over the rough surface is 61% inferior than the smooth one. These effects could also be seen in Figure 4-5 and Figure 4-6, where it was shown that the maximum reverse flow was formed farther downstream of the step in the rough case. After $x/h = 6$, the flow is reattached, and smooth profiles are ahead of the rough ones due to roughness effects. These effects fade farther of the wall, and curves match from $y/h = 2.8$ on.
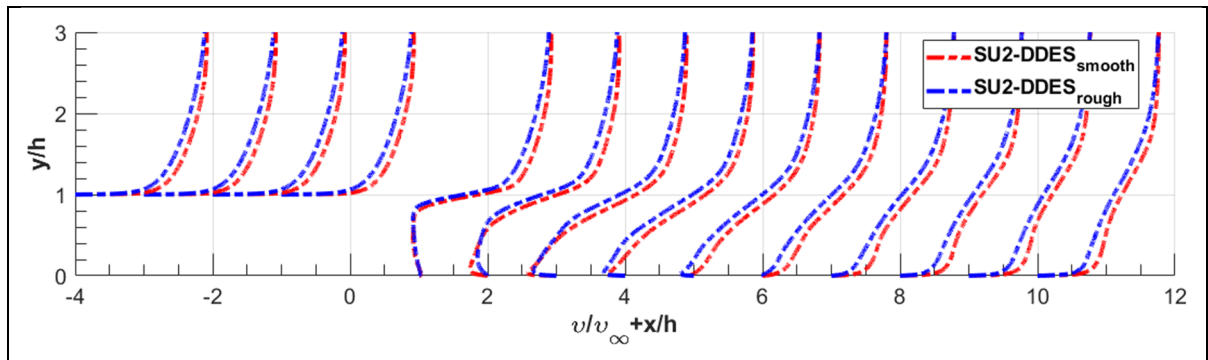
Figure 4-10 Mean streamwise velocity profiles over smooth and rough surfaces

Estimations of C_p and C_f using *SU2-RANS_rough* and *SU2-DDES_rough* are plotted in Figure 4-11 and Figure 4-12. As a matter of comparison, smooth results obtained with *SU2-DDES_smooth* are also added to the graphs. To calculate the difference between estimations of the different models, we use the same approach presented for the smooth case. Here, $\Delta C_p = 0.226$ and $\Delta C_f = 0.003$ are obtained from the difference between the peak and valley of the curve

estimated with *SU2-DDESrough*. The ROE scheme (Toro, 2013) is used for RANS, while, HR-SLAU2 (Kitamura, 2016; Kitamura & Hashimoto, 2016; Molina et al., 2020) is used for DDES. Similarly to the smooth case, C_p and C_f were calculated based on references values near the position $x/h = -4$, and pressure coefficient data was uniformly shift so that $C_p = 0$ near $x/h = 40$. Values are calculated from the time-averaged solutions, which are subsequently space averaged along the spanwise direction, as presented in Figure 4-7.

As shown in Figure 4-11, *SU2-RANSrough* and *SU2-DDESrough* estimate the same mean wall pressure coefficient in the region before the step. Roughness causes an increase of 8.24% in C_p estimations at $x/h = -0.5$, as compared to the smooth case. For the C_f calculated in the same region, *SU2-RANSrough* and *SU2-DDESrough* estimations match, achieving a value 25.8% higher than the smooth case (*SU2-DDESsmooth* estimation), as shown in Figure 4-12. After the step, the flow detaches, and a recirculation region is formed. Like in the smooth case, *SU2-RANSrough* estimations predict steeper and earlier drop in pressure and friction coefficients as compared to *SU2-DDESrough*. The added roughness results in a C_p 15.5% higher than that of the smooth case at the deepest valley (around $x/h = 2.5$).

The flows reattach at $x/h = 6.24$, $x/h = 6.13$, and $x/h = 5.48$ for *SU2-RANSrough*, *SU2-DDESrough*, and *SU2-DDESsmooth*, respectively. As the parameters are the same ones used in the smooth case, the difference in the reattachment point is clearly caused by roughness effects. Using a $\mathrm{Re}_k = 100$ at a point $4h$ before the step, *SU2-DDESrough* estimations show that the reattachment occurs 12% farther downstream as compared to the smooth case. As friction coefficients are not provided by (Essel & Tachie, 2015) and (Wu et al., 2013), the Re_k used by the authors were calculated based on the estimated c_f at a point $4h$ before the step, which was obtained using the Prandtl-Schlichting approximation ($c_f = 0.455[\log_{10}(\mathrm{Re}_x)]^{-2.58}$) taken from (Lazauskas, 2005). According to our approximations, $\mathrm{Re}_k \approx 62$ is used in the experimental results of (Essel & Tachie, 2015), and the reattachment occurs 7% farther downstream than the smooth case. In (Wu et al., 2013), a value of 3.5% is found, with a $\mathrm{Re}_k \approx 73$.
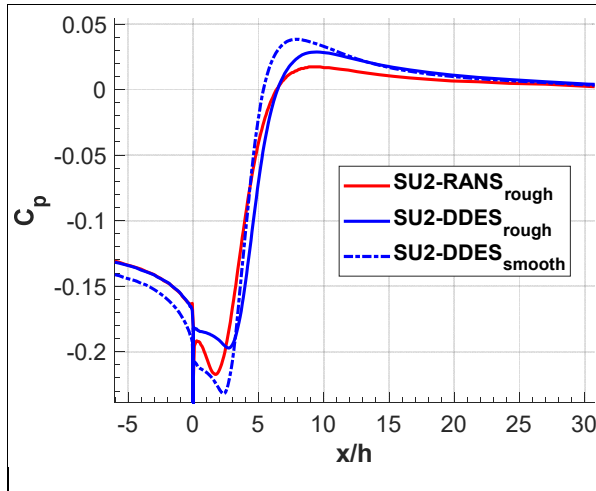
Figure 4-11 Mean pressure coefficient along the lower wall
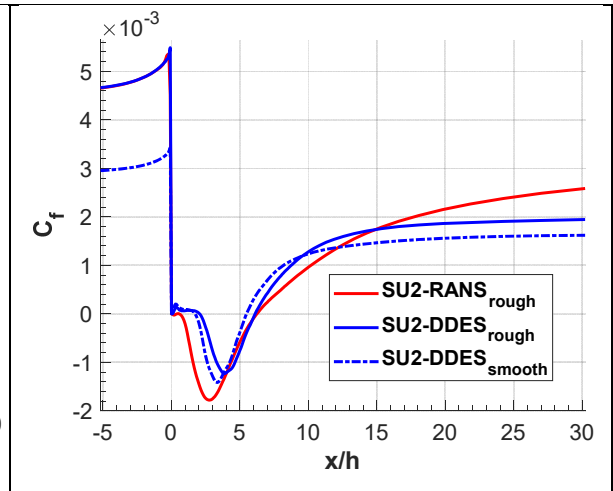
Figure 4-12 Mean skin friction coefficient along the lower wall

In the smooth case, an error of 12% was observed in the *SU2-DDESsmooth* estimation of the reattachment length as compared to experimental results obtained by Driver and Seegmiller (Driver & Seegmiller, 1985), in which the same parameters are utilized. Nevertheless, the reattachment length is within the range from $x/h = 4.9$ to $x/h = 8.2$ gathered (Eaton & Johnston, 1981) from several experiments. (Dietiker & Hoffmann, 2009) obtained a very similar error (11.5%) using DES with Menter's turbulence model (the error was calculated after digitizing the friction coefficient graph of the authors' paper). In the rough case, it was shown that the estimations of the roughness effects on the reattachment length as well as the maximum reverse flow are in accordance with findings and patterns reported in references (Essel & Tachie, 2015; Kim & Chung, 1995; Wu et al., 2013). Therefore, *SU2-DDESrough* results appear to confirm the experimental evidence of an increase of the reattachment length with roughness.

4.1.2   Rough-iced model 5-6 airfoil

The same model 5-6 airfoil used in the verification and validation section (3.1.3) is used herein. However, the effects of the aerodynamic parameters, previously estimated with *SU2-RANS*, are now evaluated using the *SU2-DDES.* The scheme of the study case (Figure 3-12), the airfoil

model characteristics, the aerodynamic parameters, the computational domain, and the equivalent sand-grain roughness height have been presented in section 3.1.3. The HR-SLAU2 scheme is used for the space integration of the flow inviscid terms, with the Roe NTS low-dissipation function. The Venkatakrishnan slope-limiting method, with constant equal to 0.03, is used with the MUSCL scheme for second order integration in space. The gradient is computed with the weighted least-square method. For the unsteady simulations, a second order dual time stepping approach is used, with 20 inner iterations. The time step is set to $\Delta t = 4 \times 10^{-5}$ (non-dimensional time is $\Delta t^* = \Delta t \dfrac{\upsilon_\infty}{c} = 2.72 \times 10^{-3}$), which is slightly smaller than the one used by (Lorenzo et al., 2011) for the same airfoil. Simulations are run for a total of 48 CTU, and the averaging is calculated using the last 26 CTU.

Table 8 compares the spanwise mesh spacing, $\Delta y / c$, the time length used to average the solution, Υ, and the dimensionless time-steps, Δt^*, of the present study to previous studies done for straight wings or iced wings at high Reynolds number around 10^6 and low Mach number using DES, DDES, ZDES and IDDES. The time length used to average the solution, Υ, is defined with $\text{CTU} = c / \upsilon_\infty$. As can be seen, the time step and span wise grid spacing vary greatly from one study to another. The spanwise mesh spacing in the present study is 0.005 (80 elements), and the time step is among the smallest used in previous studies.

Table 8 Spanwise mesh size and time step comparison between DDES studies

Model	Authors	$\Delta y / c$	Υ(CTU)	Δt^*
DES	(Pan & Loth, 2005)	1.0×10^{-2}	60	1.0×10^{-3}
DDES	(Lorenzo et al., 2011)	2.0×10^{-3}		4.3×10^{-3}
ZDES	(Le Pape et al., 2013)	4.0×10^{-3}	29	8.3×10^{-5}
DDES	(Alam et al., 2015)		6.3	2.3×10^{-4}
IDDES	(Probst et al., 2016)	8.0×10^{-4}	2.4	2.0×10^{-4}
ZDES	(Zhang et al., 2015)		21	1.0×10^{-3}
IDDES	(Butler et al., 2016)	1.3×10^{-5}	1.3	1.3×10^{-1}
DDES	(Xiao et al., 2017b)	2.0×10^{-3}		1.3×10^{-3}
DDES	(Oztekin & Riley, 2018)	3.0×10^{-3}	10	5.0×10^{-4}
IDDES	(Wang et al., 2018)		30	2.5×10^{-2}
DDES/AC	(Liu & Xiao, 2020)	2.5×10^{-3}	65	2.5×10^{-3}
DDES	Present study	5.0×10^{-3}	26	2.72×10^{-3}

Figure 4-13 and Figure 4-14 present the instantaneous iso-surfaces of the Q-criterion ($Q = 5000 \ s^{-2}$) colored by the streamwise velocity for smooth and rough iced model 5-6 airfoil. As it can be seen, these figures depict the complex three-dimensional nature of the flows with massive separation. It can be also noticed that there is no significant visual difference between the structures formed on smooth and rough iced airfoils. In both cases, a short laminar separation bubble is seen at the very beginning of the airfoil. Then, the formation of the Kelvin-Helmholtz instabilities initiates as the shear layer begin to gradually roll up, and finally break up into 3D structures.
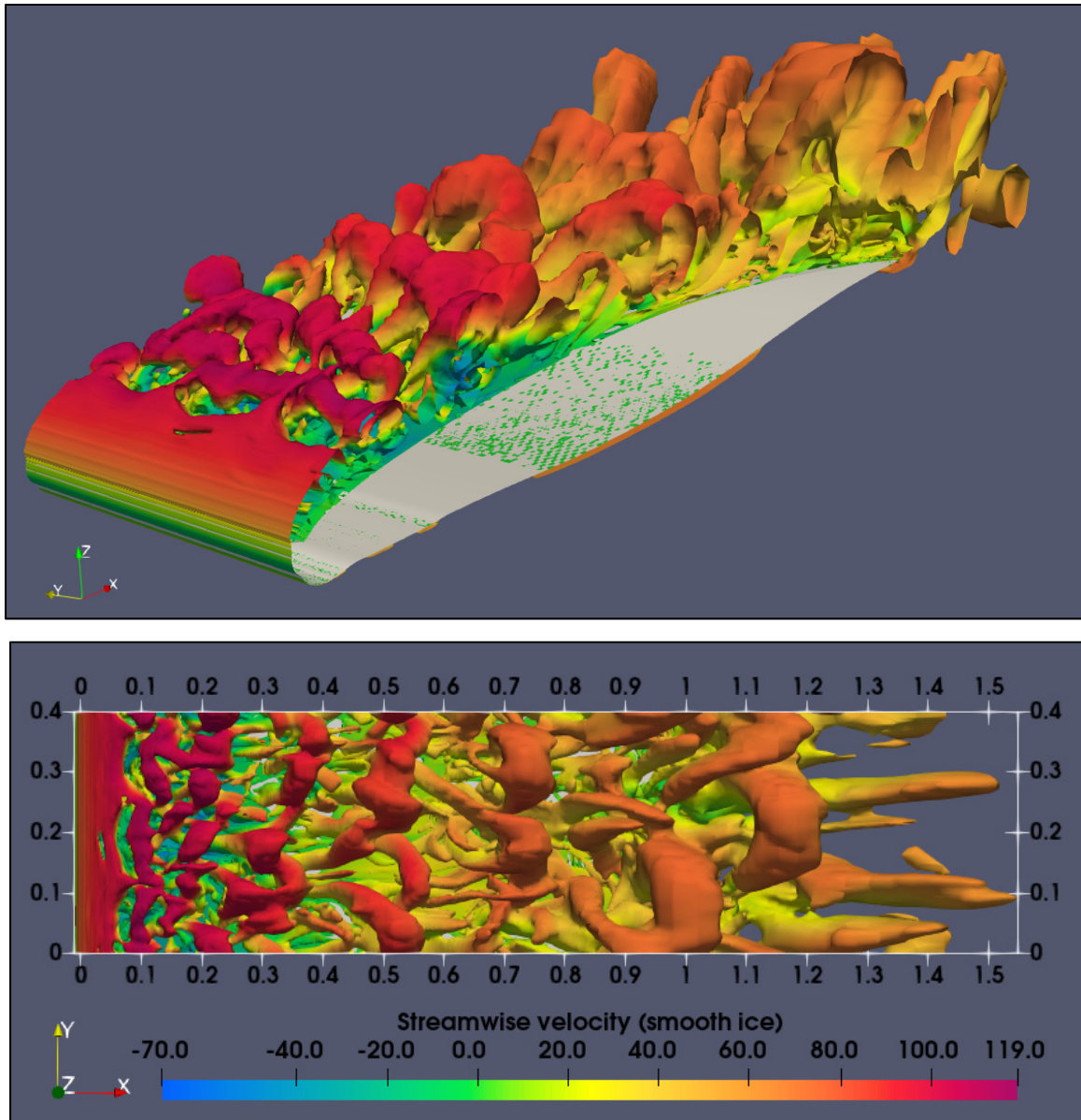
Figure 4-13 Instantaneous iso-surfaces of Q-criterion ($Q = 5000$ s^{-2}) colored by the streamwise velocity for the smooth iced model 5-6 airfoil
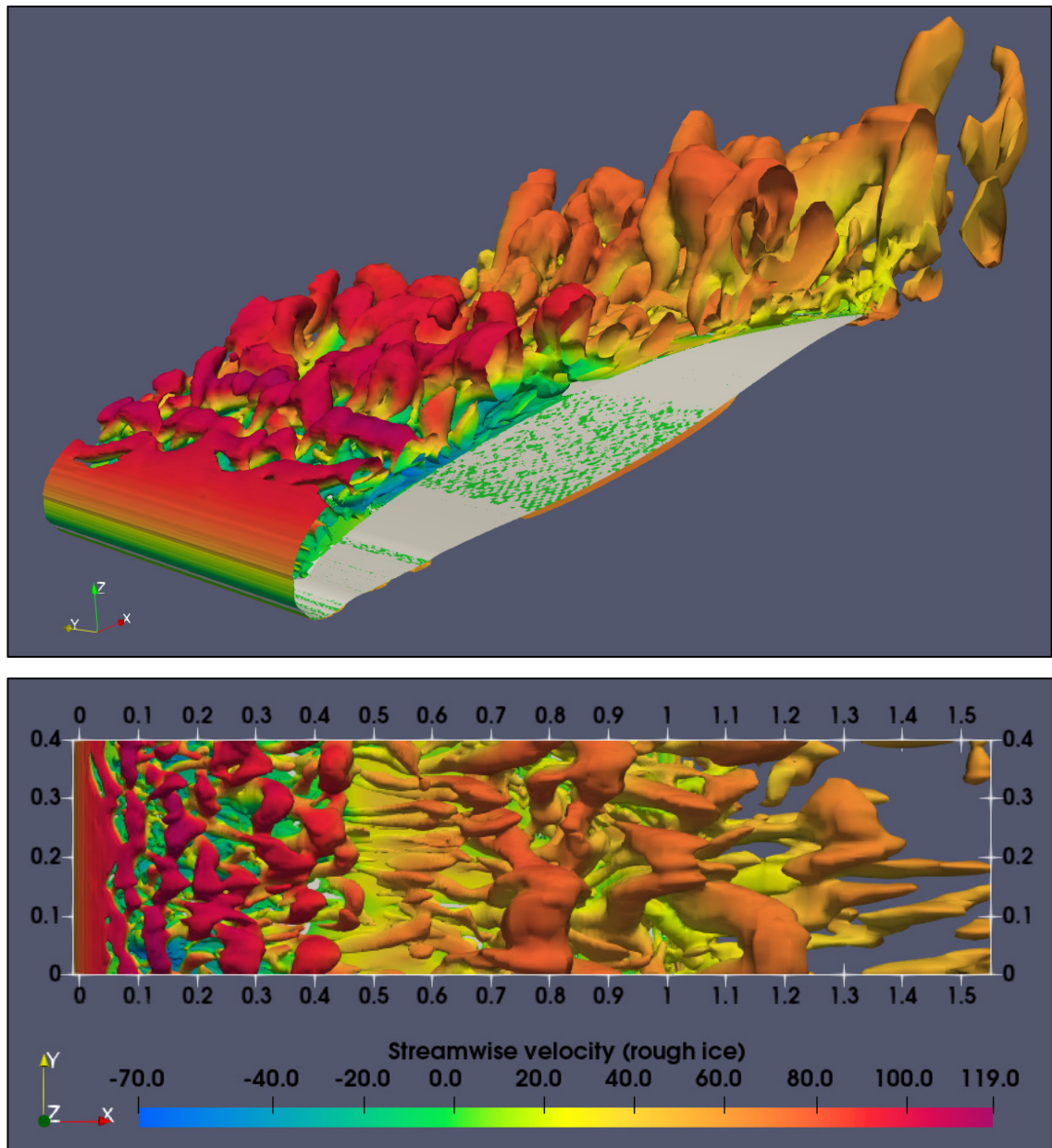
Figure 4-14 Instantaneous iso-surfaces of Q-criterion ($Q = 5000\ s^{-2}$) colored by the streamwise velocity for the rough iced model 5-6 airfoil

The flow field characteristics of the separation is marked by velocity fluctuations with respect to time, which is caused by turbulent eddies of the flow. In a DDES simulation, the RANS model is active near the wall within the boundary layer. In the separated region and in the wake, LES is active, meaning that turbulent viscosity must be reduced in order to liberate the

Kelvin-Helmholtz (KH) instability and accelerate transition to 2D and, then, 3D structures (Shur et al., 2015). Figure 4-15 and Figure 4-16 present the turbulent viscosity normalized by the dynamic viscosity, μ_{tur}/μ_{dyn}, estimated with *SU2-RANS_smooth* and *SU2-DDES_smooth*. In the case of the *SU2-DDES* solution, the time-averaged turbulent viscosity is used. The contours range from 0 to 1000 in both figures. As can be seen, the larger extend of the dark red area clearly indicates that, for *SU2-RANS_smooth* simulation, the turbulent viscosity is higher in the wake. For *SU2-DDES_smooth*, the turbulent viscosity is reduced, which confirms that LES is active in the detached region.
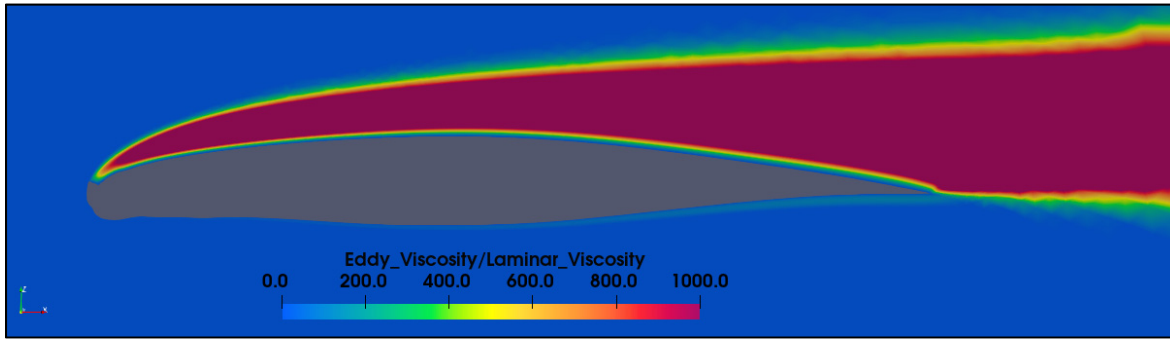
Figure 4-15 Turbulent viscosity normalized by laminar viscosity (RANS)
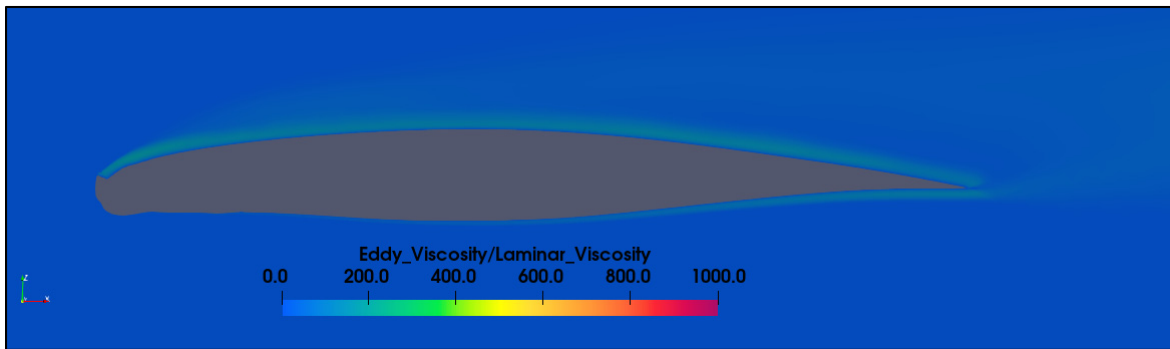
Figure 4-16 Turbulent viscosity normalized by laminar viscosity (DDES)

Figure 4-17 and Figure 4-18 present the time-averaged velocity streamlines over smooth and rough iced model 5-6 airfoils estimated with *SU2-DDES_smooth* and *SU2-DDES_rough*, respectively. The velocity streamlines are colored by the streamwise velocity (velocity in x).

The color legend is the same in both airfoils, with a maximum streamwise velocity of 106 m/s and maximum reverse velocity of -41 m/s. Similarly to *SU2-RANS* estimations (3.1.3), no significant difference is seen on the flows over smooth and rough iced airfoils. Maximum and minimum streamwise velocities are 105.8 m/s and 40.5 m/s, respectively. A noticeable difference of *SU2-DDES* estimations, as compared to *SU2-RANS*, is seen on the recirculation regions. As shown in Figure 4-17 and Figure 4-18, *SU2-DDES* estimations present a larger recirculation region just after the horn ice than *SU2-RANS*. Moreover, the trailing edge separation shown in *SU2-RANS* results (Figure 3-14 and Figure 3-15) is not present in *SU2-DDES* results.
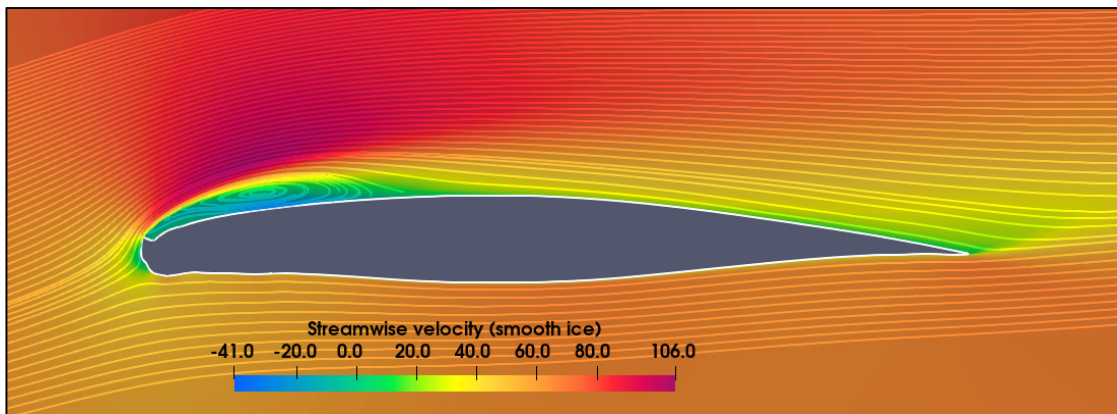
Figure 4-17 DDES estimations of time-averaged velocity streamlines of the flow over a smooth iced model 5-6 airfoil at AoA=8 degrees
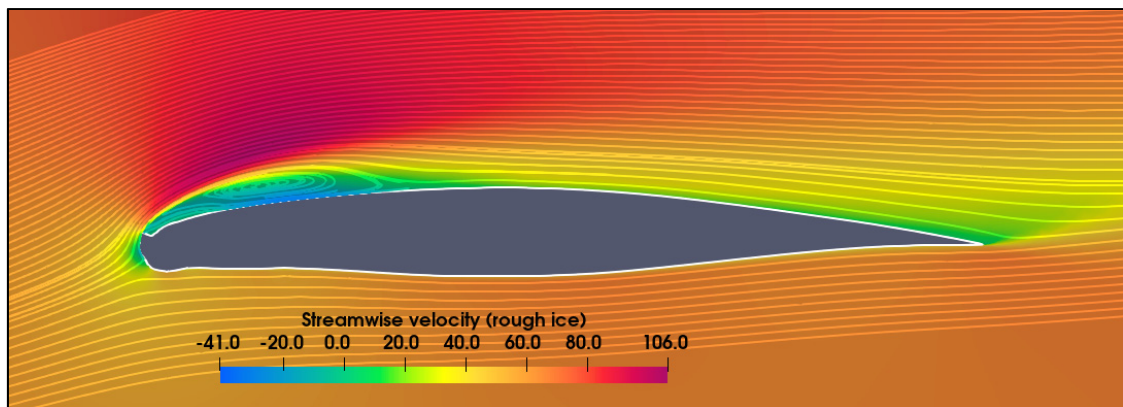
Figure 4-18 DDES estimations of time-averaged velocity streamlines of the flow over a rough iced model 5-6 airfoil at AoA=8 degrees

Figure 4-19 and Figure 4-20 present the contour plot of the time-averaged nondimensional streamwise velocity, v/v_∞, of the flows over smooth and rough iced airfoils at an AoA of 8 degrees. Curves were created using *SU2-DDES* time-averaged results taken from a cut of the middle of the airfoil (plane xz at $y=-0.2$). Similarly to what was done for the BFS, the reattachment point was evaluated based on the contour line in which the average velocity is zero. The zero-contour line is highlighted in black so that it can be easily visualized. As shown in Figure 4-19 and Figure 4-20 the flow detaches from the airfoil just after the horn tip, forming a large separation bubble downstream, and reattaching at $x/c = 0.33$ and $x/c = 0.36$, in smooth and rough cases, respectively. This is in accordance with observations of (Bragg et al., 2005), in which he highlights that the dominant flow feature of an airfoil with a horn-ice shape is the separation bubble that forms downstream of the horn. Again, no significate difference is noted between smooth and rough iced airfoils.
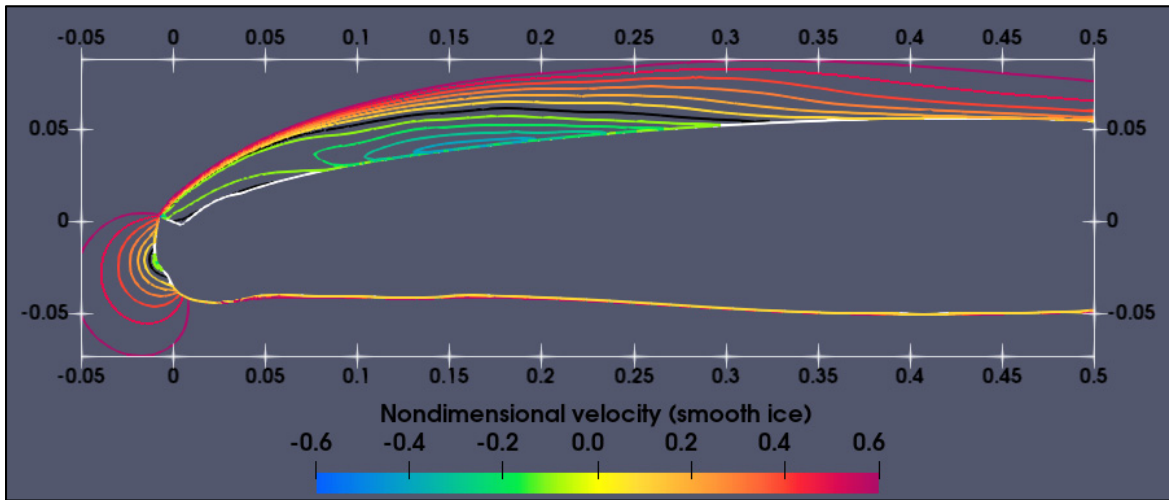
Figure 4-19 Contour plot of the time-averaged nondimensional streamwise velocity, v/v_{inf} (Smooth ice)
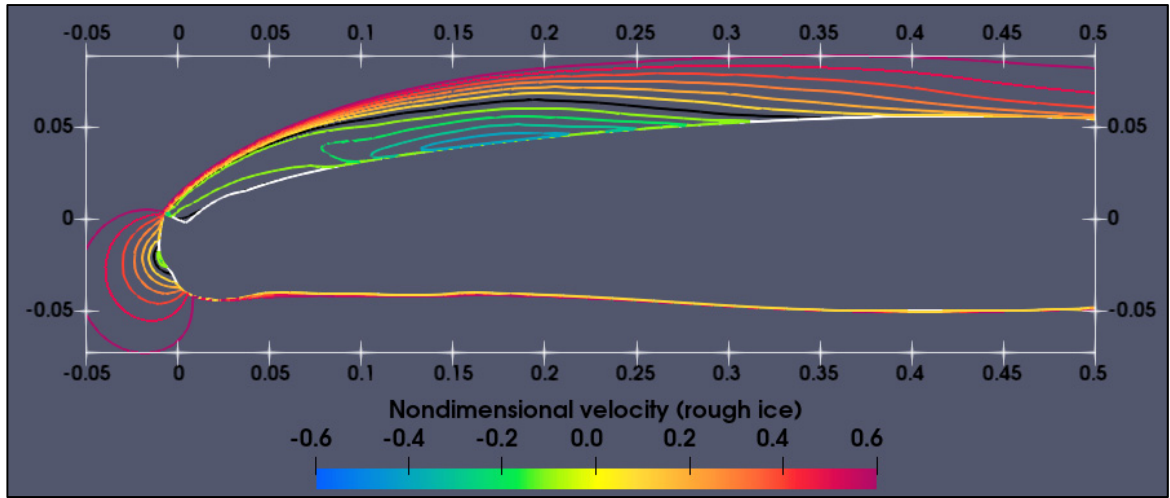
Figure 4-20 Contour plot of the time-averaged nondimensional streamwise velocity, $\upsilon/\upsilon_{\text{inf}}$ (Rough ice)

Next, we evaluate the reattachment of the shear layer considering the three-dimensional domain. For that, we present, in Figure 4-21 and Figure 4-22, the time-averaged skin friction coefficient over the whole span of smooth and rough iced airfoils. In the figures, the top view of the airfoils is presented, and the black lines illustrate the reattachment points ($c_f = 0$). No significant difference is seen in the figures. On the other hand, a small dispersion of the points is noticed. As the reattachment length, presented in Figure 4-19 and Figure 4-20, was measured from a cut in the middle of the span of the airfoil, slightly different values are obtained. Therefore, results taken from the middle of the span were compared to the time and space (spanwise) averaged values.
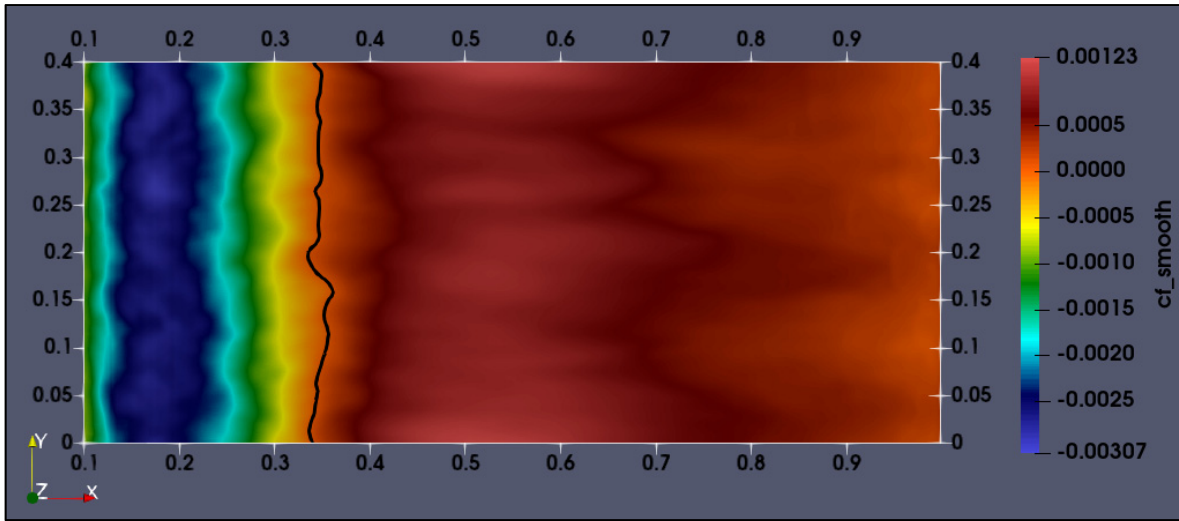
Figure 4-21 Time-averaged skin friction coefficient over smooth iced 5-6 airfoil
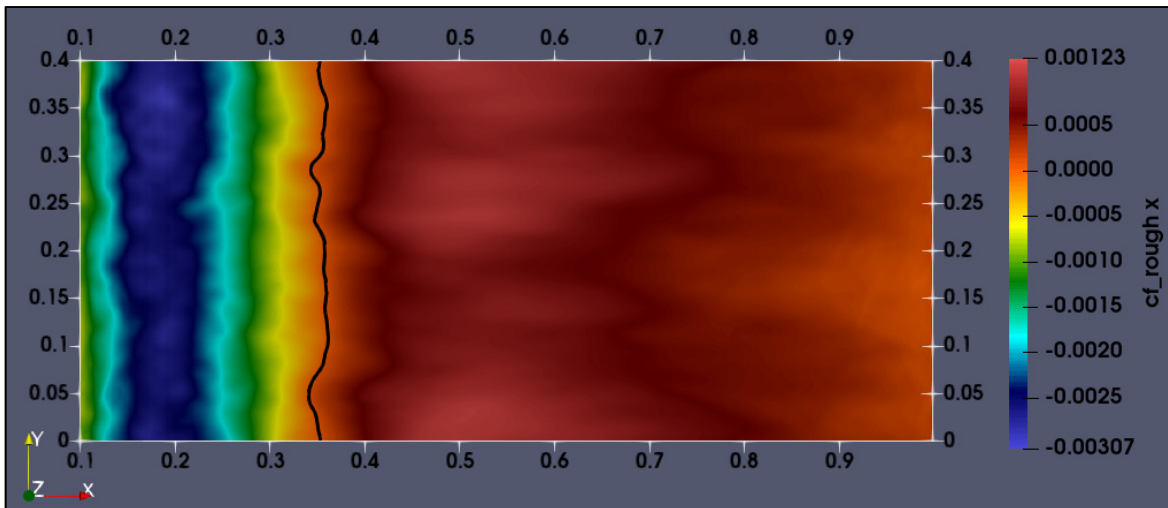
Figure 4-22 Time-averaged skin friction coefficient over rough iced 5-6 airfoil

Figure 4-23 presents the reattachment points along the span of the airfoil of smooth and rough iced airfoils overlapped. The black line represents the smooth case, whereas the red line represents the rough case. The space averages (spanwise) of both lines match with a value of $x/c = 0.35$, and standard deviations of 0.0060 and 0.0056, for smooth and rough cases, respectively. Values taken from the middle of the channel resulted in $x/c = 0.33$ and

$x/c = 0.36$. Although the difference is not significative, values taken from the middle of the wing wrongly suggest that a small difference in the reattachment is found.
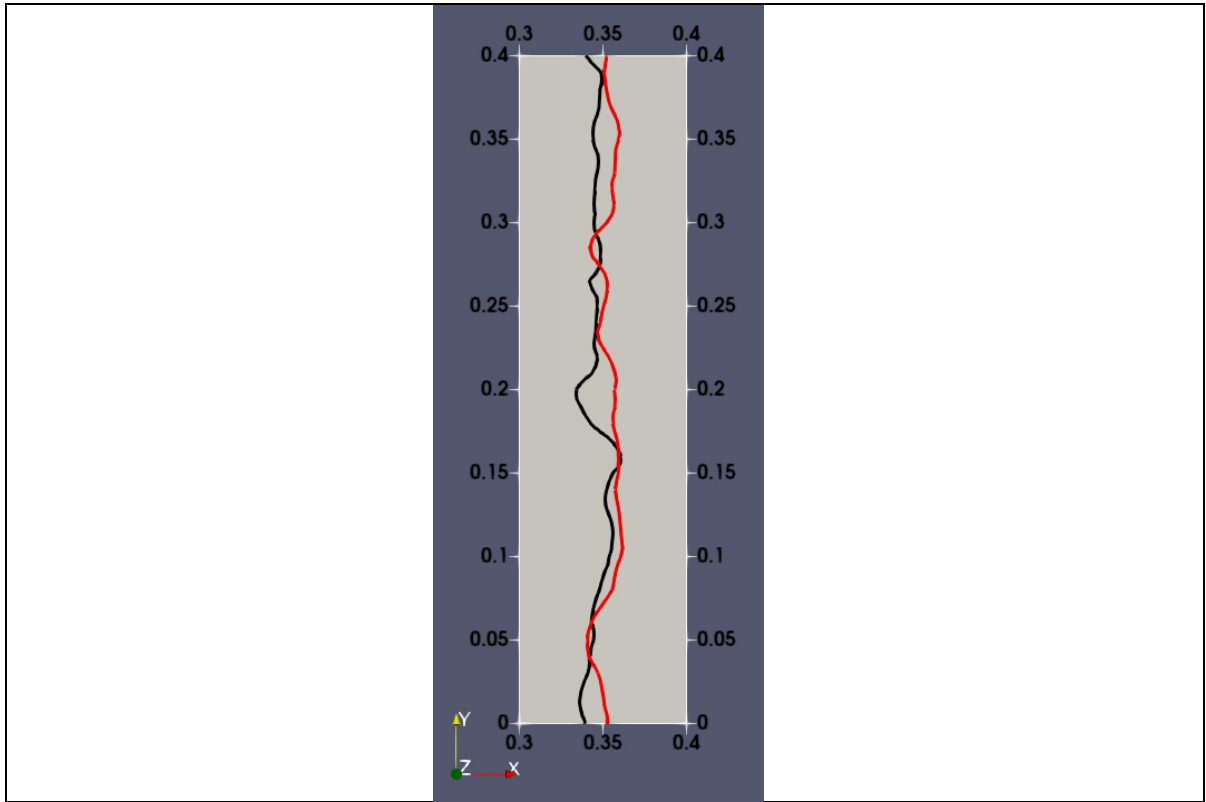
Figure 4-23 C_f estimated over smooth (black line) and rough (red line) iced airfoil

As for *SU2-DDES* estimations of pressure coefficient, reduced dispersion of points is found, which results in more uniform values along the span of the airfoils. The top views of the time-averaged pressure coefficient over smooth and rough iced airfoils are presented in Figure 4-24 and Figure 4-25. As a matter of comparison, values of $C_p = -1.2$ are highlighted on both wings, as shown by the black lines in Figure 4-24 and Figure 4-25. The dispersion of points along the spanwise direction reaches standard deviations of 0.0017 and 0.0012 for smooth and rough iced airfoils, respectively. In this case, values taken from the middle of the channel and the spanwise averaged ones match, being $x/c = 0.25$.
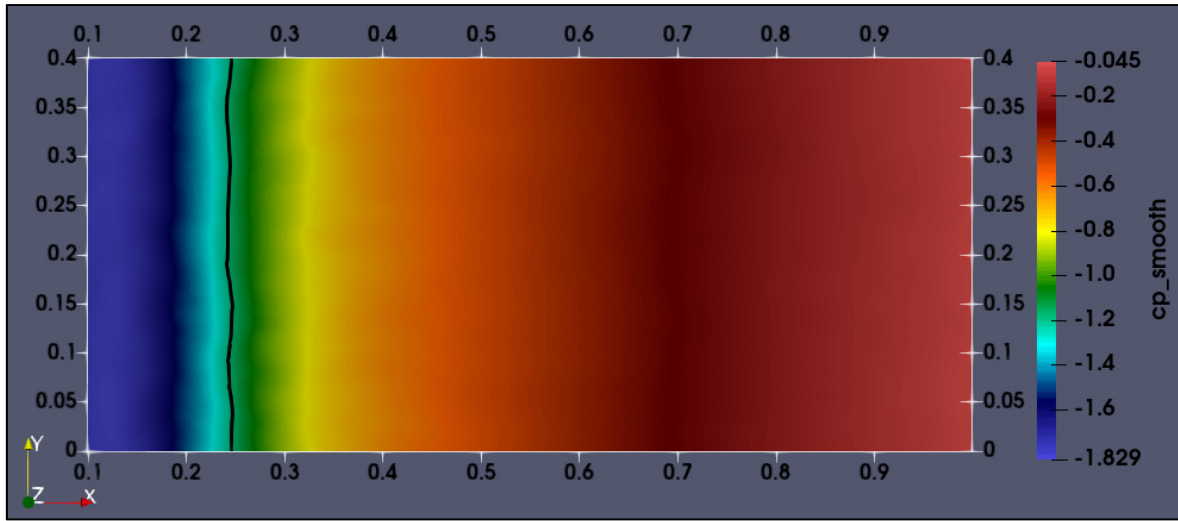
Figure 4-24 Time-averaged pressure coefficient over smooth iced model 5-6 airfoil
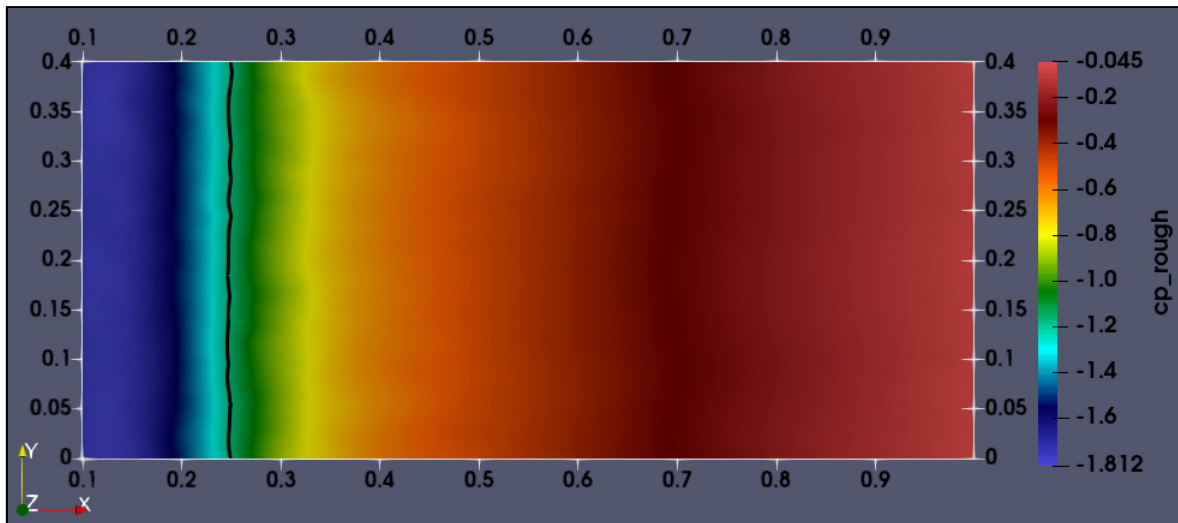
Figure 4-25 Time-averaged pressure coefficient over rough iced model 5-6 airfoil

In this way, *SU2-DDES* time-averaged estimations of the pressure coefficient around the airfoil (taken from the middle of the span at $y/c=0.2$) are plotted in Figure 4-26. Values obtained with the *SU2-RANS* model are also plotted for comparison. In addition, experimental and numerical results from the literature are plotted as reference. *SU2-DDES* results suggest that the effects of the horn ice are much greater than roughness, which results in no significant difference between the flows over smooth and rough ice. Estimations show that the boundary

layer separates at the tip of the horn due to the abrupt pressure gradient following the sketch of the laminar separation bubble done by (Bragg et al., 2005; Bragg et al., 1992) based on experimental results. According to their sketch, one can identify the "separation" and "transition" in the plateau region where pressure distribution is relatively constant. In our results, this region begins at the leading edge (separation) extending up to $x/c = 0.15$ (transition), as shown in Figure 4-26. At the transition point, the pressure recovery begins. As shown in Figure 4-26, *SU2-DDES* presents a faster pressure recovery than Lorenzo's elsA (DDES) code, and the largest discrepancy between the codes reaches 12.5% at $x/c = 0.3$. This difference between the codes might be caused by the rapid transition from RANS to LES obtained with the implementation of the SLA-SGS (Shur et al., 2015), which was not available by the time of Lorenzo's publication. As expected, *SU2-RANS* fails in regions of massive flow separation. On the other hand, all codes present very similar results on the pressure side.

Figure 4-27 presents the magnitude of the time-averaged friction coefficient distribution along the airfoil estimated with *SU2-RANS* and *SU2-DDES*. The x-axis represents the curvilinear coordinates normalized by the chord, with the negative values on the pressure side. As expected, *SU2-RANS* and *SU2-DDES* estimations are very close on the lower surface (no massive separation) of the airfoils. The increase of friction coefficient caused by roughness is clearly seen on both sides of the airfoils. On the suction region, the peak estimated by both codes occurs at $s/c = 0.015$, where the horn tip is localized. *SU2-DDES* estimations show friction coefficients close to zero past $s/c = 0.035$ over smooth and rough iced airfoils, whereas *SU2-RANS* present greater values for both airfoils. Moreover, the *SU2-RANS*$_{rough}$ predicts higher values of friction coefficient than *SU2-RANS*$_{smooth}$ in most of the region between $s/c = 0.04$ and $s/c = 0.065$.

For the reattachment point, *SU2-RANS*$_{smooth}$ and *SU2-DDES* predicted the same lengths of $x/c = 0.35$. Very close results of RANS and DDES simulations were also found by Choo et al. (2004) using an extruded GLC305/944-ice shape wing. In their simulation, "the time-averaged flow is separated for more than 40% of chord in the DES simulation and slightly less

than 40% in the RANS simulations". On the other hand, when roughness was active in our simulations, *SU2-RANS*rough estimated a longer reattachment length of $x/c = 0.4$.
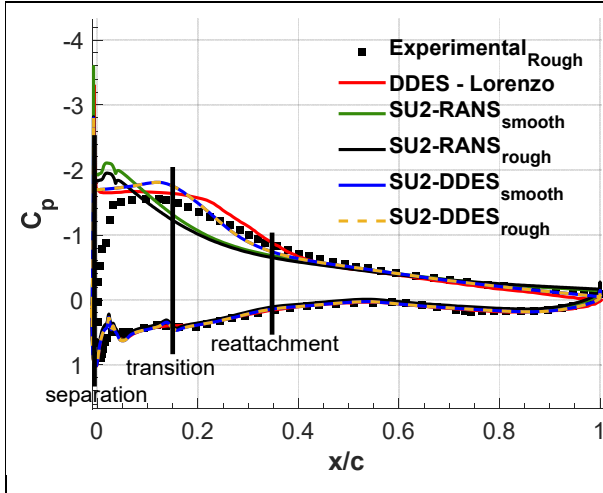
Figure 4-26 Mean pressure coefficient   Figure 4-27 Mean skin friction coefficient
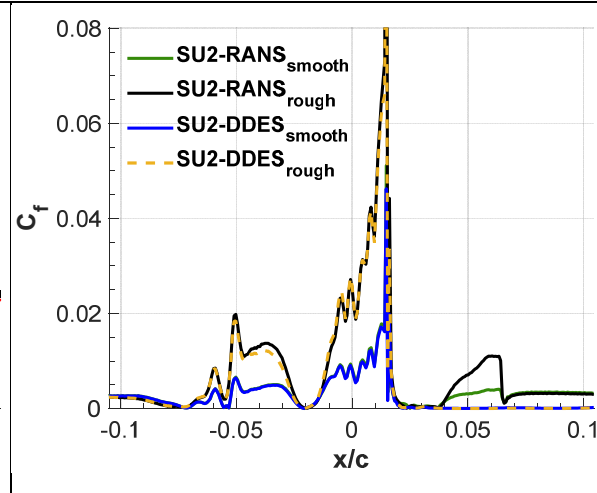
Figure 4-28 presents lift and drag curves obtained from experimental data as well as estimations using RANS and DDES models over smooth and rough ice. At higher AoA (over 5 degrees), larger separations are present, and *SU2-RANS* fails when estimating C_l. A similar behavior is seen in a comparison between RANS and DDES simulations done by Molina et al. (2020), in which a GLC-305 airfoil with a leading-edge horn-shape glaze ice is used. In their work, RANS and DDES presented good accuracy at zero degrees. However, RANS predicted a complete stalled flow field at 6 degrees (pre-stall angle), while DDES was in good agreement with experiments. Similarly, in our study, *SU2-DDES* simulations presented improved results as compared to *SU2-RANS*. When estimating C_l at 8 degrees, *SU2-RANS* presented an error of 6.8% for the smooth and rough cases, as compared to experiments. *SU2-DDES* achieved an error of 2.75%, with and without roughness. For C_d , results were also improved. *SU2-DDESsmooth* presented a drag coefficient 3.84% higher than experimental results, whereas *SU2-RANSsmooth* estimation was 7.64% inferior. Similarly, *SU2-DDESrough*'s estimation presented an error of 2.64%, against 4.9% of *SU2-RANSrough*'s.
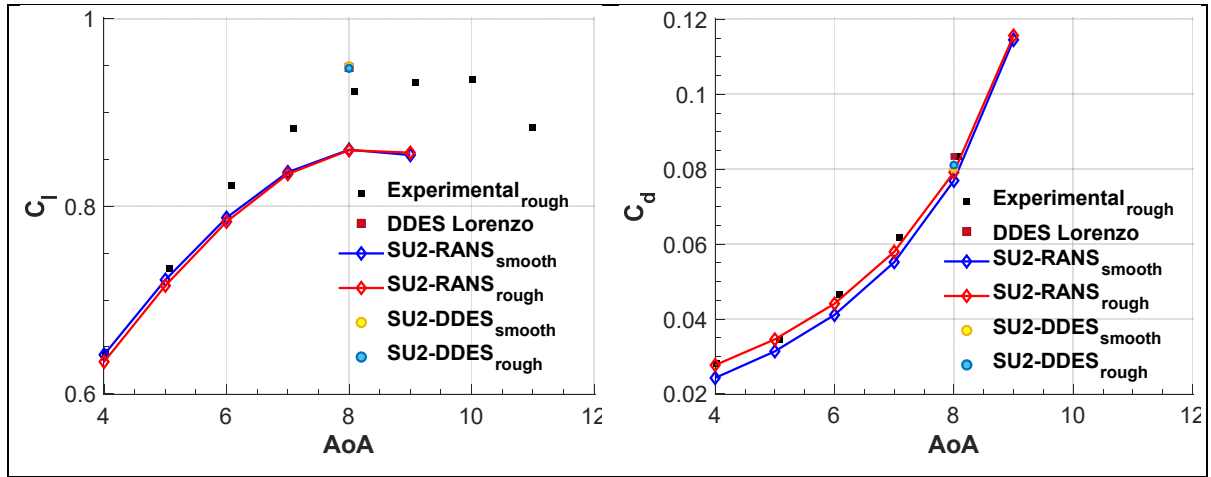
Figure 4-28 Lift and drag curves for smooth and rough ice using RANS and DDES

As shown by our results, although the DDES model improved estimations as compared to RANS, no significant roughness effects are produced on the flow over a model 5-6 airfoils with a horn-type ice accretion. This lack of roughness effects was caused by greater effects created by the horn ice on the leading edge of the airfoil.

4.2 Summary

The hybrid RANS/LES model known as Delayed Detached Eddy Simulation (DDES) coupled with the Spalart-Allmaras extension implemented to consider roughness effects, herein treated as SU2$_{rough}$, was used to estimate C_p, C_f, C_l, C_d, v/v_{inf} as well as the reattachment length of shear layers over rough and smooth surfaces. Estimations were performed using two study cases, a rough backward facing step and a rough-iced model 5-6 airfoil. For the rough backward facing step, C_p, C_f, v/v_{inf} and reattachment length were estimated. As expected, higher values of C_p and C_f were obtained because of roughness effects. In the same way, the resistance caused by roughness reduced the region of maximum reverse flow in the recirculation region, which was formed 42% farther downstream. Consequently, the reattachment of the shear layer occurred 12% farther downstream. It was shown that SU2$_{rough}$ estimations of roughness effects were in accordance with findings and patterns reported in the literature. For the rough-iced model 5-6 airfoil, C_p, C_f, C_l, C_d and the reattachment length

of the shear layer were estimated. Although the DDES presented improved estimations as compared to RANS, no significant roughness effects were noticed on the flow over a model 5-6 airfoils with a horn-type ice accretion. In conclusion, the rough BFS and the rough iced model 5-6 airfoil study cases presented regions in which a sudden low pressure is produced followed by massive flow separation. Therefore, improved estimations were obtained using the *SU2-DDES$_{rough}$* as compared to the *SU2-RANS$_{rough}$*. On the other hand, results show different effects between the two study cases. In the rough BFS, roughness produced significant effects due to the large extent of the rough wall (along all the bottom walls). Whereas, in the rough iced model 5-6 airfoil, no significant effects were seen when roughness was added only to the ice horn. This lack of roughness effects was caused by greater effects created by the horn ice on the leading edge of the airfoil.

CONCLUSION

In this research, we introduced the problem of aircraft icing, and how the aircraft performance is affected by this phenomenon. Among the methods to evaluate the performance degradation caused by icing, we pointed out the use of numerical simulations. Our literature review drew attention to the current tendency of moving from RANS to hybrid models such as DES and DDES, in industry and academia. Some improvements proposed to augment fidelity of estimations of these models were also presented. On the other hand, it was noticed that an important characteristic of iced airfoils has never been considered in these models, roughness. Therefore, we proposed to numerically estimate the aerodynamic performance degradation of a three-dimensional post-stall-angle rough iced wing using a hybrid model (RANS/LES) called DDES including RANS with roughness implemented. In order to accelerate the transition from RANS to LES, we combined the Shear-Layer Adapted (SLA) Sub-Grid length Scale (SGS) (to unlock the Kelvin-Helmholtz instability) with the low-dissipation scheme HR-SLAU2.

The process of verification and validation of the roughness implementation into SU2 was performed using RANS (smooth and rough surfaces) and DDES (smooth surfaces with massive flow separation) simulations. For RANS, three study cases were used, a flat plate, a NACA 0012 airfoil, and an iced model 5-6 airfoil. Each study case was duplicated so that we could evaluate flows over smooth and rough surfaces. Our estimations of friction (flat plates) and lift (NACA 0012) coefficients were equivalent or superior to results obtained from the literature. The estimations of nondimensional velocities were improved in the first region the NACA 0012 airfoil. On the other hand, the thickening of the boundary layer caused by roughness resulted in a slight underestimation of values (with errors under 11%) after $x/c = 0.10$. For the iced model 5-6, no significant difference is seen between smooth and rough estimations of lift coefficient. However, when larger regions of detached flow were reached after 6 degrees, C_l is underestimated as compared to experiments. This behaviour was expected due to the inefficiency of RANS models to capture the physics of massive flow separation. When estimating C_d, a maximum error of 60% was achieved as compared to

experimental results when roughness was not considered. However, the roughness implementation successfully reduced this error to 6.7%.

In addition, we performed two investigations with the roughness implementation in RANS, a study on the Reynolds number sensitivity, and the influence of equivalent sand-grain roughness heights on the aircraft performance degradation based on the deterioration of the $C_{l(\max)}$. Our results demonstrated that, when increasing the Reynolds number, a plateau was reached around $\mathrm{Re} = 3 \times 10^6$ resulting in a stationary reduction of maximum lift coefficient. Similarly, it was seen in the equivalent k_s heights investigation that the continuous increase of k_s did not result in a linear performance degradation. On the contrary, the variation of the reduction of maximum lift coefficient became drastically reduced after equivalent sand-grain roughness heights of around $k_s / c = 9 \times 10^{-4}$.

For DDES verification and validation, we utilized two study cases with massive flow separation, a smooth-surface channel with a Backward Facing Step, (BFS), and a smooth-surface NACA 0012 airfoil in deep stall. As DDES is an unsteady model aimed at capturing the physics of massive-separated-flow turbulence, a minimum length in the spanwise direction was required to capture this three-dimensional phenomenon. In this way, we performed a study using backward facing steps with three different aspect ratios, $z/h = 2, 3$ and 4, which directed us towards choosing the width of $z/h = 4$ for our simulations. Thus, in the verification and validation using the BFS, C_p, C_f and velocity profiles were estimated achieving reduced errors as compared to the references. Likewise, for the NACA 0012 in deep stall, our estimations presented errors of 2.89% for C_d, and 8.9 for C_l as compared to experiments, which was similar to previous DDES results. The errors of C_p estimations were slightly higher (maximum error of 12.3%) as compared to experiments, which is also similar to previous DDES results.

Finally, in our third research objective, the DDES model with roughness implementation was used to evaluate how roughness affects DDES estimations of aerodynamic parameters of

massive-separated flows over rough surfaces. The evaluation was performed using two three-dimensional study cases, a rough backward facing step and a rough-iced model 5-6 airfoil. Both study cases presented regions in which a sudden low pressure is produced followed by massive flow separation. Several aerodynamic parameters such as C_p, C_f, C_l, C_d, $\upsilon/\upsilon_{\text{inf}}$ as well as the reattachment length of shear layers were estimated. For the rough BFS, roughness was distributed along the entire length of the bottom walls, and for the rough iced airfoil, roughness was distributed only along the ice surface. As expected, higher values of C_p and C_f were obtained in the BFS study case due to roughness effects. In the same way, the resistance caused by roughness reduced the region of maximum reverse flow in the recirculation region, which was formed 42% farther downstream, and delayed the reattachment of the shear layer that occurred 12% farther downstream. It was shown that the roughness effects estimations were in accordance with findings and patterns reported in the literature. On the other hand, different results were seen for the rough iced model 5-6 airfoil. Although the DDES presented improved estimations as compared to RANS, no significant roughness effects were noticed on the aerodynamic parameters of the flow over the rough-horn-type iced airfoil. The difference seen between the iced airfoil and the BFS results, was caused by two reasons. First, the small length of the roughness distribution, which is only along the ice surface. Second, roughness effects were weaker than the great adverse pressure gradient created just after the tip of the horn ice, which "overshadowed" any roughness effects.

Another important conclusion risen from this research is the risk of evaluating aerodynamic parameters using conventional methods commonly applied in the post-processing of RANS simulations such as taking values from a cut in the middle of the domain (e.g., a cut in the middle of the span of a wing) to plot the friction or pressure coefficient. As shown in sections 4.1.1 and 4.1.2, results taken from sections at different distances along the spanwise direction might vary considerably, which results in misleading information. Therefore, we recommend the evaluation of dispersion of points along the spanwise direction before any parameter is analyzed in the post-processing step. Then, if a high dispersion is found, a space average procedure must be performed along the span to reduce possible errors.

Future studies could use different lengths of rough ice accretion to evaluate whether roughness effects become noticeable for a specific length. Moreover, pressure gradient assessment could reveal what range of gradients undergoes the "overshadowing" effect.

Furthermore, our model could be used to evaluate the effects of the onset of icing formation (roughness ice) using airfoils in pre-stall conditions. As no abrupt pressure is expected in this case, roughness effects would be favored, which could result in improved results.

Lastly, studies could explore the effects of wall roughness using other AoA as well as different iced airfoils to confirm whether the similarity on the reattachment length of rough and smooth iced airfoil, found in our study, is always the same.

BIBLIOGRAPHY

Abbott, I. H., Von Doenhoff, A. E., & Stivers Jr, L. (1945). *Summary of airfoil data* (NACA-TR-824). Retrieved from Office of Aeronautical Intelligence, Washington, DC, United States: https://ntrs.nasa.gov/citations/19930090976

Alam, M., Thompson, D. S., & Walters, D. K. (2015). Hybrid Reynolds-Averaged Navier–Stokes/Large-Eddy simulation models for flow around an iced wing. *Journal of aircraft, 52*(1), 244-256. doi:https://doi.org/10.2514/1.C032678

Anderson, J. D. (2001). *Fundamentals of aerodynamics* (N. Y. McGraw-Hill, NY Ed. Third ed.): McGraw-Hill.

Appiah-Kubi, P. (2011). *US Inflight Icing Accidents and Incidents, 2006 to 2010.* (Masters). University of Tennessee, Knoxville, Retrieved from https://trace.tennessee.edu/utk_gradthes/1055

Aupoix, B. (2015a). Improved heat transfer predictions on rough surfaces. *International Journal of Heat and Fluid Flow, 56*, 160-171. doi:https://doi.org/10.1016/j.ijheatfluidflow.2015.07.007

Aupoix, B. (2015b). Roughness Corrections for the k–ω Shear Stress Transport Model: Status and Proposals. *Journal of Fluids Engineering, 137*(2). doi:https://doi.org/10.1115/1.4028122

Aupoix, B., & Spalart, P. (2003). Extensions of the Spalart–Allmaras turbulence model to account for wall roughness. *International Journal of Heat and Fluid Flow, 24*(4), 454-462. doi:https://doi.org/10.1016/S0142-727X(03)00043-2

Bates, P. D., Lane, S. N., & Ferguson, R. I. (2005). *Computational fluid dynamics: applications in environmental hydraulics*: John Wiley & Sons.

Beaugendre, H., Morency, F., Habashi, W. G., & Benquet, P. (2003). Roughness implementation in FENSAP-ICE: Model calibration and influence on ice shapes. *Journal of aircraft, 40*(6), 1212-1215. doi:https://doi.org/10.2514/2.7214

Beierle, M. T. (1999). *Investigation of Effects of Surface Roughness on Symmetric Airfoil Lift and Lift-to-Drag Ratio.* (Doctoral thesis). University of Maryland - College Park, Defense Technical Information Center. Retrieved from http://www.dtic.mil/dtic/tr/fulltext/u2/a360065.pdf

Blanchard, A. (1977). *Analyse expérimentale et théorique de la structure de la turbulence d'une couche limite sur paroi rugueuse.* (Doctoral thesis PhD). Université de Poitiers Retrieved from http://www.sudoc.fr/095999868

Blazek, J. (2015). *Computational fluid dynamics: principles and applications* (Third ed.): Elsevier Ltd.

Bragg, M. B. (1982). *Rime ice accretion and its effect on airfoil performance.* (PhD). The Ohio State University, NTRS - NASA Technical Reports Server. Retrieved from https://ntrs.nasa.gov/citations/19820016290 (19820016290)

Bragg, M. B., Broeren, A. P., & Blumenthal, L. A. (2005). Iced-airfoil aerodynamics. *Progress in Aerospace Sciences, 41*(5), 323-362. doi:https://doi.org/10.1016/j.paerosci.2005.07.001

Bragg, M. B., & Gregorek, G. (1989). *Environmentally Induced Surface Roughness Effects on Laminar Flow Airfoils: Implications for Flight Safetyy.* Paper presented at the AIAA/AHS/ASEE Aircraft Design, Systems and Operations Conference. doi:https://doi.org/10.2514/6.1989-2049

Bragg, M. B., Khodadoust, A., & Spring, S. (1992). Measurements in a leading-edge separation bubble due to a simulated airfoil ice accretion. *AIAA Journal, 30*(6), 1462-1467. doi:https://doi.org/10.2514/3.11087

Brumby, R. E. (1979). Wing Surface Roughness: Cause and Effect. *DC Flight Approach, 32*, 2-7.

Butler, C., Qin, C., & Loth, E. (2016). *Improved Delayed Detached-Eddy Simulation on a Swept Hybrid Model in IRT.* Paper presented at the 8th AIAA Atmospheric and Space Environments Conference. doi:https://doi.org/10.2514/6.2016-3736

Cao, Y., Wu, Z., Su, Y., & Xu, Z. (2015). Aircraft flight characteristics in icing conditions. *Progress in Aerospace Sciences, 74*, 62-80. doi:https://doi.org/10.1016/j.paerosci.2014.12.001

Caruelle, B. (2000). *Simulations d'écoulements instationnaires turbulents en aérodynamique: application à la prédiction du phénomène de tremblement.* (PhD). Toulouse, INPT, Retrieved from http://www.sudoc.abes.fr/cbs/xslt/DB=2.1//SRCH?IKT=12&TRM=058494812 (2000INPT017H)

Cebeci, T. (1987). *Effects of environmentally imposed roughness on airfoil performance.* (NASA-CR-179639). NTRS - NASA Technical Reports Server Retrieved from https://ntrs.nasa.gov/citations/19890002354

Choo, Y. K., Thompson, D., & Mogili, P. (2004). *Detached-eddy simulations of separated flow around wings with ice accretions: year one report.* (NASA/CR-2004-213379). NTRS - NASA Technical Reports Server Retrieved from https://ntrs.nasa.gov/citations/20050019522

Critzos, C. C., Heyson, H. H., & Boswinkle Jr, R. W. (1955). *Aerodynamic characteristics of NACA 0012 airfoil section at angles of attack from 0 deg to 180 deg.* (NACA-TN-3361). NTRS - NASA Technical Reports Server: National Aeronautics and Space Administration Retrieved from https://ntrs.nasa.gov/citations/19930084501

Deck, S. (2002). *Simulation numérique des charges latérales instationnaires sur des configurations de lanceur.* (PhD). Orléans, Retrieved from http://www.sudoc.fr/07046524X

Deck, S. (2005). Zonal-Detached-Eddy Simulation of the Flow Around a High-Lift Configuration. *AIAA Journal, 43*(11), 2372-2384. doi:https://doi.org/10.2514/1.16810

Deck, S. (2012). Recent improvements in the zonal detached eddy simulation (ZDES) formulation. *Theoretical and Computational Fluid Dynamics, 26*(6), 523-550. doi:https://doi.org/10.1007/s00162-011-0240-z

deVelder, N. B. (2020). *Rough Airfoil Simulation for Wind Turbine Applications.* (PhD). University of Massachusetts Amherst, Retrieved from https://scholarworks.umass.edu/dissertations_2/1820/

Dezitter, F., Montreuil, E., Guffond, D., Caminade, F., Catris, S., Arnal, D., . . . Houdeville, R. (2009). *Enhancement of Prediction Capability in Icing Accretion and Related Performance Penalties Part II: CFD Prediction of the Performance Degradation due*

to Ice. Paper presented at the 1st AIAA Atmospheric and Space Environments Conference, 22-25 June 2009, Reston, VA, USA. Retrieved from http://citeseerx.ist.psu.edu/viewdoc/summary?doi=10.1.1.711.8833

Dietiker, J.-F., & Hoffmann, K. A. (2009). Predicting Wall Pressure Fluctuation over a Backward-Facing Step Using Detached Eddy Simulation. *Journal of aircraft, 46*(6), 2115-2120. doi:https://doi.org/10.2514/1.43912

Dirling, J., R. (1973, July 16, 1973). *A method for computing roughwall heat transfer rates on reentry nosetips.* Paper presented at the 8th Thermophysics Conference, Fluid Dynamics and Co-located Conferences, Palm Springs,CA,U.S.A. doi:https://doi.org/10.2514/6.1973-763

Driver, D. M., & Seegmiller, H. L. (1985). Features of a reattaching turbulent shear layer in divergent channelflow. *AIAA Journal, 23*(2), 163-171. doi:https://doi.org/10.2514/3.8890

Eaton, J., & Johnston, J. (1981). A Review of Research on Subsonic Turbulent Flow Reattachment. *AIAA Journal, 19*(9), 1093-1100. doi:https://doi.org/10.2514/3.60048

Edwards, J. R., & Chandra, S. (1996). Comparison of eddy viscosity-transport turbulence models for three-dimensional, shock-separated flowfields. *AIAA Journal, 34*(4), 756-763. doi:https://doi.org/10.2514/3.13137

Eick, D. (Producer). (2015, August 09, 2020). Aircraft Icing Accidents. [Presentation] Retrieved from https://www.ral.ucar.edu/sites/default/files/public/events/2016/friends-and-partners-in-aviation-weather/docs/01eick.pptx

Essel, E. E., & Tachie, M. F. (2015). Roughness Effects on Turbulent Flow Downstream of a Backward Facing Step. *Flow, turbulence and combustion, 94*(1), 125-153. doi:https://doi.org/10.1007/s10494-014-9549-1

Flack, K. A., & Schultz, M. P. (2010). Review of Hydraulic Roughness Scales in the Fully Rough Regime. *Journal of Fluids Engineering, 132*(4). doi:https://doi.org/10.1115/1.4001492

GARTEUR. (2003). *Prediction of performance degradation due to icing for 2D configurations*. Retrieved from

Gray, V. H. (1958). *Correlations Among Ice Measurements, Impingement Rates Icing Conditions, and Drag Coefficients for Unswept NACA 65A004 Airfoil*. (NACA-TN-4151). NTRS - NASA Technical Reports Server Retrieved from https://ntrs.nasa.gov/citations/19810068588

Gray, V. H. (1964). *Prediction of Aerodynamic Penalties Caused by Ice Formations on Various Airfoils*. (NASA TN D-2166). NASA Lewis Research Center Retrieved from https://books.google.ca/books/about/Prediction_of_Aerodynamic_Penalties_Caus.html?id=t0rByZmBO_8C&redir_esc=y

Green, S. (2006). *A Study of U.S. Inflight Icing Accidents and Incidents, 1978 to 2002.* Paper presented at the 44th AIAA Aerospace Sciences Meeting and Exhibit. doi:https://doi.org/10.2514/6.2006-82

Gregory, N., & O'Reilly, C. L. (1970). *Low-Speed Aerodynamic Characteristics of NACA0012 Aerofoil Section, including the Effects of Uppe-Surface Roughness Simulating Hoar Frost*. (3726). CiteSeerX Retrieved from http://citeseerx.ist.psu.edu/viewdoc/download?doi=10.1.1.227.696&rep=rep1&type=pdf

Gulick, B. G. (1938). *Effects of a Simulated Ice Formation on the Aerodynamic Characteristics of an Airfoil*. (NACA-WR-L-292). NTRS - NASA Technical Reports Server Retrieved from https://ntrs.nasa.gov/citations/19930093051

Guseva, E. K., Garbaruk, A. V., & Strelets, M. K. (2017). Assessment of delayed DES and improved delayed DES combined with a shear-layer-adapted subgrid length-scale in separated flows. *Flow, turbulence and combustion, 98*(2), 481-502. doi:https://doi.org/10.1007/s10494-016-9769-7

Hellsten, A., & Laine, S. (1998). Extension of k-W Shear-Stress Transport Turbulence Model for Rough-Wall Flows. *AIAA Journal, 36*(9), 1728-1729. doi:http://dx.doi.org/10.2514/2.7543

Hoerner, S. F. (1965). *Fluid Dynamic Drag*.

Holmén, V. (2012). *Methods for vortex identification.* (Masters). Lund University, Retrieved from http://lup.lub.lu.se/student-papers/record/3241710 (LUTFMA-3239-2012)

Im, H.-S., & Zha, G.-C. (2014a). Delayed Detached Eddy Simulation of Airfoil Stall Flows Using High-Order Schemes. *Journal of Fluids Engineering, 136*(11), 111104. doi:https://doi.org/10.1115/1.4027813

Im, H.-S., & Zha, G.-C. (2014b). Delayed Detached Eddy Simulation of Airfoil Stall Flows Using High-Order Schemes. *Journal of Fluids Engineering, 136*. doi:10.1115/1.4027813

Jackson, D. G. (1999). *Effect of simulated ice and residual ice roughness on the performance of a natural laminar flow airfoil.* (Masters). University of Illinois at Urbana-Champaign, Retrieved from http://icing.ae.illinois.edu/papers/00/darren%20jackson%20dissertation.html

Jefferson-Loveday, R. J. (2020). Enhanced Delayed Detached Eddy Simulation for Cavities and Labyrinth Seals. *Journal of Engineering for Gas Turbines and Power, 142*(1). doi:https://doi.org/10.1115/1.4045484

Jespersen, D. C., Pulliam, T. H., & Childs, M. L. (2016). *Overflow turbulence modeling resource validation results*. (20190000252). NTRS - NASA Technical Reports Server: NASA Retrieved from https://ntrs.nasa.gov/citations/20190000252

Kays, W., & Crawford, M. (1993). *Convective Heat and Mass Transfer, McGraw-Hill*.

Kerho, M. F., & Bragg, M. B. (1997). Airfoil Boundary-Layer Development and Transition with Large Leading-Edge Roughness. *AIAA Journal, 35*(1), 75-84. doi:https://doi.org/10.2514/2.65

Kim, B. N., & Chung, M. K. (1995). Experimental study of roughness effects on the separated flow over a backward-facing step. *AIAA Journal, 33*(1), 159-161. doi:https://doi.org/10.2514/3.12348

Kim, H., & Bragg, M. B. (1999). *Effects of leading-edge ice accretion geometry on airfoil performance.* Paper presented at the 17th Applied Aerodynamics Conference. doi:https://doi.org/10.2514/6.1999-3150

Kitamura, K. (2016). Assessment of SLAU2 and other flux functions with slope limiters in hypersonic shock-interaction heating. *Computers & Fluids, 129*, 134-145. doi:https://doi.org/10.1016/j.compfluid.2016.02.006

Kitamura, K., & Hashimoto, A. (2016). Reduced dissipation AUSM-family fluxes: HR-SLAU2 and HR-AUSM+-up for high resolution unsteady flow simulations. *Computers & Fluids, 126*, 41-57. doi:https://doi.org/10.1016/j.compfluid.2015.11.014

Knopp, T., Eisfeld, B., & Calvo, J. B. (2009). A new extension for k–ω turbulence models to account for wall roughness. *International Journal of Heat and Fluid Flow, 30*(1), 54-65. doi:https://doi.org/10.1016/j.ijheatfluidflow.2008.09.009

Kundu, P. K., Cohen, I. M., & Dowling, D. R. (2012). *Fluid Mechanics* Academic Press.

Ladson, C. L. (1988). *Effects of independent variation of Mach and Reynolds numbers on the low-speed aerodynamic characteristics of the NACA 0012 airfoil section.* (NASA-TM-4074). NTRS - NASA Technical Reports Server Retrieved from https://ntrs.nasa.gov/citations/19880019495

Langel, C. M., Chow, R., Van Dam, C., & Maniaci, D. C. (2017). *RANS Based Methodology for Predicting the Influence of Leading Edge Erosion on Airfoil Performance.* Sandia National Lab.(SNL-NM), Albuquerque, NM (United States) Retrieved from https://www.osti.gov/biblio/1404827-rans-based-methodology-predicting-influence-leading-edge-erosion-airfoil-performance

Larsson, J., Kawai, S., Bodart, J., & Bermejo-Moreno, I. (2016). Large eddy simulation with modeled wall-stress: recent progress and future directions. *Mechanical Engineering Reviews, 3*(1), 15-00418-00415-00418. doi:https://doi.org/10.1299/mer.15-00418

LaViolette, M. (2017). On the history, science, and technology included in the Moody diagram. *Journal of Fluids Engineering, 139*(3). doi:https://doi.org/10.1115/1.4035116

Lazauskas, L. V. (2005). *Hydrodynamics of advanced high-speed sealift vessels.* (Masters). The University of Adelaide, Retrieved from http://hdl.handle.net/2440/37729

Le Pape, A., Richez, F., & Deck, S. (2013). Zonal detached-eddy simulation of an airfoil in poststall condition. *AIAA Journal, 51*(8), 1919-1931. doi:https://doi.org/10.2514/1.J052235

Lee, C.-H. (2018). Rough boundary treatment method for the shear-stress transport k-ω model. *Engineering Applications of Computational Fluid Mechanics, 12*(1), 261-269. doi:https://doi.org/10.1080/19942060.2017.1410497

Liu, J., & Xiao, Z. (2020). Low-Frequency Oscillation over NACA0015 Airfoil Near Stall at High Reynolds Number. *AIAA Journal, 58*(1), 53-60. doi:https://doi.org/10.2514/1.J058598

Liu, S. (2014). *Simulation of Transition and Roughness Effects on Micro Air Vehicle Aerodynamics.* (PhD). University of Sheffield, Retrieved from http://etheses.whiterose.ac.uk/id/eprint/7757

Lorenzo, A., Valero, E., & De-Pablo, V. (2011). *DES/DDES post-stall study with iced airfoil.* Paper presented at the 49th AIAA Aerospace Sciences Meeting Including the New Horizons Forum and Aerospace Exposition. doi:https://doi.org/10.2514/6.2011-1103

Lynch, F. T., & Khodadoust, A. (2001). Effects of ice accretions on aircraft aerodynamics. *Progress in Aerospace Sciences, 37*(8), 669-767.

Mendez, B., Muñoz, A., & Munduate, X. (2015, 5-9 January 2015). *Study of distributed roughness effect over wind turbine airfoils performance using CFD.* Paper presented at the 33rd Wind Energy Symposium, Kissimmee, Florida. doi:https://doi.org/10.2514/6.2015-0994

Menter, F., & Kuntz, M. (2004). Adaptation of eddy-viscosity turbulence models to unsteady separated flow behind vehicles. In *The aerodynamics of heavy vehicles: trucks, buses, and trains* (pp. 339-352): Springer, Berlin, Heidelberg. doi:https://doi.org/10.1007/978-3-540-44419-0_30

Mockett, C. (2009). *A Comprehensive Study of Detached Eddy Simulation*: Univerlagtuberlin.

Mockett, C., Haase, W., & Schwamborn, D. (2018). *Go4Hybrid: Grey Area Mitigation for Hybrid RANS-LES Methods* (Vol. 134): Springer.

Molina, E., Spode, C., Annes da Silva, R. G., Manosalvas-Kjono, D. E., Nimmagadda, S., Economon, T. D., . . . Righi, M. (2017). *Hybrid rans/les calculations in su2.* Paper presented at the 23rd AIAA Computational Fluid Dynamics Conference. doi:https://doi.org/10.2514/6.2017-4284

Molina, E. S., Silva, D. M., Broeren, A. P., Righi, M., & Alonso, J. J. (2020). Application of DDES to Iced Airfoil in Stanford University Unstructured (SU2). In *Progress in Hybrid RANS-LES Modelling* (pp. 283-293): Springer. doi:https://doi.org/10.1007/978-3-030-27607-2_23

Moody, L. F. (1944). Friction factors for pipe flow. *Trans. Asme, 66*, 671-684. Retrieved from http://www.ipt.ntnu.no/~asheim/TPG4135/Moody.pdf

Nikuradse, J. (1933). *Laws of flow in rough pipes*: National Advisory Committee for Aeronautics Washington.

Orszag, S. A., & Patterson, G. (1972). Numerical simulation of turbulence. In *Statistical models and Turbulence* (pp. 127-147): Springer. doi:https://doi.org/10.1007/3-540-05716-1_8

Oztekin, E. S., & Riley, J. T. (2018). *Ice accretion on a NACA 23012 airfoil.* Paper presented at the 2018 Atmospheric and Space Environments Conference. doi:https://doi.org/10.2514/6.2018-2860

Palacios, F., Colonno, M. R., Aranake, A. C., Campos, A., Copeland, S. R., Economon, T. D., . . . Alonso, J. J. (2013). *Stanford University Unstructured (SU2): An open-source integrated computational environment for multi-physics simulation and design.* Paper presented at the 51st AIAA Aerospace Sciences Meeting including the New Horizons Forum and Aerospace Exposition 2013, January 7, 2013 - January 10, 2013, Grapevine, TX, United states. doi:https://doi.org/10.2514/6.2013-287

Pan, J., & Loth, E. (2005). Detached eddy simulations for iced airfoils. *Journal of aircraft, 42*(6), 1452-1461. doi:https://doi.org/10.2514/1.11860

Papadakis, M., Alansatan, S., & Seltmann, M. (1999). *Experimental study of simulated ice shapes on a NACA 0011 airfoil.* Paper presented at the 37th Aerospace Sciences Meeting and Exhibit. doi:https://doi.org/10.2514/6.1999-96

Papadakis, M., Alansatan, S., & Wong, S.-C. (2000). *Aerodynamic characteristics of a symmetric NACA section with simulated ice shapes.* Paper presented at the 38th Aerospace Sciences Meeting and Exhibit. doi:https://doi.org/10.2514/6.2000-98

Papadakis, M., Alansatan, S., & Yeong, H. (2000). *Aerodynamic performance of a T-tail with simulated ice accretions.* Paper presented at the 38th Aerospace Sciences Meeting and Exhibit. doi:https://doi.org/10.2514/6.2000-363

Papadakis, M., & Gile Laflin, B. (2001). *Aerodynamic performance of a tail section with simulated ice shapes and roughness.* Paper presented at the 39th aerospace sciences meeting and exhibit. doi:https://doi.org/10.2514/6.2001-539

Papadakis, M., Gile Laflin, B., Youssef, G., & Ratvasky, T. (2001). *Aerodynamic scaling experiments with simulated ice accretions*. Paper presented at the 39th Aerospace Sciences Meeting and Exhibit. doi:https://doi.org/10.2514/6.2001-833

Papadakis, M., Yeong, H., Chandrasekharan, R., Hinson, M., Ratvasky, T., & Giriunas, J. (2001). *Experimental investigation of simulated ice accretions on a full-scale T-tail.* Paper presented at the 39th Aerospace Sciences Meeting and Exhibit. doi:https://doi.org/10.2514/6.2001-90

Patel, V. (1998). Perspective: flow at high Reynolds number and over rough surfaces— Achilles heel of CFD. doi:https://doi.org/10.1115/1.2820682

Philippe, R. (2001). *Young-Person''s Guide to Detached-Eddy Simulation Grids*. NTRS - NASA Technical Reports Server Retrieved from https://ntrs.nasa.gov/citations/20010080473

Probst, A., Löwe, J., Reuß, S., Knopp, T., & Kessler, R. (2016). Scale-resolving simulations with a low-dissipation low-dispersion second-order scheme for unstructured flow solvers. *AIAA Journal, 54*(10), 2972-2987. doi:https://doi.org/10.2514/1.J054957

Ratvasky, T. P., Barnhart, B. P., & Lee, S. (2010). Current Methods Modeling and Simulating Icing Effects on Aircraft Performance, Stability, Control. *Journal of aircraft, 47*(1), 201-211. doi:https://doi.org/10.2514/1.44650

Rumsey, C., Smith, B., & Huang, G. (2018). Turbulence Modeling Resource website [online]. Retrieved from http://turbmodels.larc.nasa.gov

Schlichting, H. (1937). *Experimental Investigation of the Problem of Surface Roughness*. (NACA-TM-823). Retrieved from https://ntrs.nasa.gov/citations/19930094593

Sheldahl, R. E., & Klimas, P. C. (1981). *Aerodynamic Characteristics of Seven Symmetrical Airfoil Sections Through 180-Degree Angle of Attack for Use in Aerodynamic Analysis of Vertical Axis Wind Turbines*. Retrieved from https://www.semanticscholar.org/paper/Aerodynamic-Characteristics-of-Seven-Symmetrical-of-Sheldahl-Klimas/e70e0520d1418d29cc868ecc00174c2273b9eefc

Shur, M., Spalart, P., Strelets, M., & Travin, A. (1999). Detached-eddy simulation of an airfoil at high angle of attack. In *Engineering Turbulence Modelling and Experiments 4* (pp. 669-678): Elsevier. doi:https://doi.org/10.1016/B978-008043328-8/50064-3

Shur, M. L., Spalart, P. R., Strelets, M. K., & Travin, A. K. (2008). A hybrid RANS-LES approach with delayed-DES and wall-modelled LES capabilities. *International Journal of Heat and Fluid Flow, 29*(6), 1638-1649. doi:https://doi.org/10.1016/j.ijheatfluidflow.2008.07.001

Shur, M. L., Spalart, P. R., Strelets, M. K., & Travin, A. K. (2015). An Enhanced Version of DES with Rapid Transition from RANS to LES in Separated Flows. *Flow, turbulence and combustion, 95*(4), 709-737. doi:https://doi.org/10.1007/s10494-015-9618-0

Spalart, P., & Allmaras, S. (1992). *A one-equation turbulence model for aerodynamic flows* (AIAA Paper 1992-439). Retrieved from https://doi.org/10.2514/6.1992-439

Spalart, P., & Allmaras, S. (1992). *A one-equation turbulence model for aerodynamic flows.* Paper presented at the 30th aerospace sciences meeting and exhibit. doi:https://doi.org/10.2514/6.1992-439

Spalart, P., & Allmaras, S. (1994). A One-Equation Turbulence Model for Aerodynamic Flows. *Recherche Aérospatiale, 1*, 5-21.

Spalart, P., Deck, S., Shur, M., Squires, K., Strelets, M., & Travin, A. (2005). A New Version of Detached-Eddy Simulation, Resistant to Ambiguous Grid Densities. *Theoretical and Computational Fluid Dynamics*. doi:https://doi.org/10.1007/s00162-006-0015-0

Spalart, P., Jou, W., Strelets, M., & Allmaras, S. (1997). *Comments on the feasibility of LES for wings, and on a hybrid RANS/LES approach.* Paper presented at the Advances in DNS/LES First AFOSR International Conference on DNS/LES, Lousinia. https://www.semanticscholar.org/paper/Comments-on-the-feasibility-of-LES-for-wings%2C-and-a-Spalart/b2a4f279d5d9f417085b0372e1173497baef73c8

Spalart, P., & Venkatakrishnan, V. (2016). On the role and challenges of CFD in the aerospace industry. *The Aeronautical Journal, 120*(1223), 209. doi:https://doi.org/10.1017/AER.2015.10

Spalart, P. R. (2009). Detached-eddy simulation. *Annual review of fluid mechanics, 41*, 181-202. doi:https://doi.org/10.1146/annurev.fluid.010908.165130

Squires, K. D., Krishnan, V., & Forsythe, J. R. (2008). Prediction of the flow over a circular cylinder at high Reynolds number using detached-eddy simulation. *Journal of Wind Engineering and Industrial Aerodynamics, 96*(10-11), 1528-1536. doi:https://doi.org/10.1016/j.jweia.2008.02.053

Stebbins, S. J. (2018). *Review and Study of Aerodynamic Simulations of Lifting Bodies with Ice Accretion.* (Masters). Retrieved from https://libraetd.lib.virginia.edu/public_view/st74cr01f

Stebbins, S. J., Loth, E., Broeren, A. P., & Potapczuk, M. (2019). Review of computational methods for aerodynamic analysis of iced lifting surfaces. *Progress in Aerospace Sciences, 111*, 100583. doi:https://doi.org/10.1016/j.paerosci.2019.100583

Tabatabaian, M. (2015). *CFD module*: Stylus Publishing, LLC.

Tagawa, G. B. S., Morency, F., & Beaugendre, H. (2018). *CFD study of airfoil lift reduction caused by ice roughness.* Paper presented at the 2018 Applied Aerodynamics Conference. doi:https://doi.org/10.2514/6.2018-3010

Toro, E. F. (2013). *Riemann solvers and numerical methods for fluid dynamics: a practical introduction* (Third ed.): Springer-Verlag Berlin Heidelberg.

Travin, A., Shur, M., Strelets, M., & Spalart, P. (2000). Detached-Eddy Simulations Past a Circular Cylinder. *Flow, turbulence and combustion, 63*(1-4), 293-313. doi:https://doi.org/10.1023/A:1009901401183

Valarezo, W. O., Lynch, F. T., & McGhee, R. J. (1993). Aerodynamic performance effects due to small leading-edge ice (roughness) on wings and tails. *Journal of aircraft, 30*(6), 807-812. doi:https://doi.org/10.2514/3.46420

Versteeg, H. K., & Malalasekera, W. (2007). *An introduction to computational fluid dynamics - The finite volume method* (2nd ed.). Toronto: Pearson Education.

Wang, L., Hu, R., Li, L., & Fu, S. (2018). Detached-Eddy Simulations for Active Flow Control. *AIAA Journal, 56*(4), 1447-1462. doi:https://doi.org/10.2514/1.J055891

White, F. M., & Corfield, I. (2006). *Viscous fluid flow* (Vol. 3): McGraw-Hill New York.

Wilcox, D. C. (1988). Reassessment of the scale-determining equation for advanced turbulence models. *AIAA Journal, 26*(11), 1299-1310. doi:https://doi.org/10.2514/3.10041

Winkler, C., Dorgan, A., & Mani, M. (2012). *A reduced dissipation approach for unsteady flows on unstructured grids.* Paper presented at the 50th AIAA Aerospace Sciences Meeting Including the New Horizons Forum and Aerospace Exposition.

Wu, Y., Ren, H., & Tang, H. (2013). Turbulent flow over a rough backward-facing step. *International Journal of Heat and Fluid Flow, 44*, 155-169. doi:https://doi.org/10.1016/j.ijheatfluidflow.2013.05.014

Xiao, M., Zhang, Y., & Chen, H. (2017a). *Numerical Study of an Iced Airfoil Based on Delayed Detached-Eddy Simulation with Low Dissipation Scheme.* Paper presented at the 9th AIAA Atmospheric and Space Environments Conference. doi:https://doi.org/10.2514/6.2017-3761

Xiao, M., Zhang, Y., & Chen, H. (2017b). *Numerical Study of an Iced Airfoil Using Window-Embedded RANS/LES Hybrid Method.* Paper presented at the 9th AIAA Atmospheric and Space Environments Conference. doi:https://doi.org/10.2514/6.2017-3761

Younes, K., Grenke, A., Hickey, J.-P., Gagnon, M., & Elzein, B. (2020). *Enhanced Delayed Detached Eddy Simulations of Shock-Vector Control.* Paper presented at the 23rd AIAA International Space Planes and Hypersonic Systems and Technologies Conference. doi:https://doi.org/10.2514/6.2020-2411

Zhang, Y., Habashi, W. G., & Khurram, R. A. (2015). Zonal Detached-Eddy Simulation of Turbulent Unsteady Flow over Iced Airfoils. *Journal of Aircraft, 53*(1), 168-181. doi:10.2514/1.C033253

Zhiyin, Y. (2015). Large-eddy simulation: Past, present and the future. *Chinese journal of Aeronautics, 28*(1), 11-24. doi:https://doi.org/10.1016/j.cja.2014.12.007